MESOSCALE MOTIONS INDUCED BY CUMULUS CONVECTION: A NUMERICAL STUDY

by

JOHN MAURICE BROWN

B.A., University of California at Los Angeles, 1964

M.A., University of California at Los Angeles, 1966

SUBMITTED IN PARTIAL FULFILLMENT OF THE

REQUIREMENTS FOR THE DEGREE OF DOCTOR OF PHILOSOPHY

at the

MASSACHUSETTS INSTITUTE OF TECHNOLOGY

October 1974

ic February 1975

Signature of Author .....
Department of Meteorology, 28 October 1974

Certified by .....
Thesis Supervisor

Accepted by .....
Chairman, Departmental Committee on Graduate Students

Lindgren

WITHDRAWN

JAN 23 1975

FROM

MIT LIBRARIES

MESOSCALE MOTIONS INDUCED BY CUMULUS CONVECTION:

A NUMERICAL STUDY

by

John Maurice Brown

Submitted to the Department of Meteorology on 28 October 1974
in partial fulfillment of the requirements for the degree of
Doctor of Philosophy.

ABSTRACT

There is evidence from observations that evaporation of precipitation falling from widespread thick masses of middle- and high-cloud cumulonimbus debris is of vital importance to the dynamics of some tropical disturbances.

A numerical model suitable for testing this idea has been designed and run. Dynamics of the large-scale flow are governed by the hydrostatic unfiltered equations specialized to two dimensions and solved by standard finite difference procedures. There are 19 vertical layers, horizontal grid distance is 25 km, and domain length is 10^3 km. The value of f is for 10°N.

Cumulus convection is parameterized through a one-dimensional plume model which allows for vertical transport of water substance in vapor and liquid form. These plumes, all of uniform size, are assumed to cover only a small fraction of a gridcolumn's cross-sectional area. Within each grid-column the total mass flux upward through convective cloud base is assumed proportional to the large-scale upward mass flux through 90 cb. The proportionality factor, β, is an assigned constant for each computation. Convective-scale precipitation is parameterized by placing an upper limit, r_{lim}, on the liquid-water mixing ratio within convective clouds; any excess condensate is assumed to fall out without evaporation. The water budget for the large-scale includes vapor and both cloud and precipitation and allows for transformations between these categories.

The initial state for all computations resembles a simple tropical wave in a moist but unsaturated environment. The wavelength is 10^3 km. During all model runs a large-scale cloud forms due to detrainment at convective-cloud top. Amplifying internal gravity waves of small scale obscure the meteorologically significant motions after eight to twelve hours of model integration; no attempt is made to control these.

Computations are sensitive to the choices of r_{lim} and β. For β = 1.0, the initial wave disturbance weakens. Rapid deepening of the

initial disturbance in runs with β = 1.35 and 1.50 is a result of low-level warming by "compensating subsidence" between clouds. Larger τ_{ecm} causes convective-cloud tops to be lower and the large-scale cloud to be more dense.

That evaporative cooling can induce a mesoscale downdraft of 10 cm sec^{-1} is demonstrated by a pair of runs having β = 1.35, τ_{ecm} = .006, and vertical shear of the zonal wind. One run includes evaporation of large-scale precipitation, the other does not. In the former, there develops a low-level mesosystem similar to that observed by Zipser in the Line Islands. Furthermore, evaporation is sufficient to terminate deepening of the initial wave disturbance. Close to half of this evaporation is the end result of ascent initiated by cumulus-convection heating within the large-scale cloud. It is tentatively concluded that under ideal conditions, precipitation evaporation on a scale larger than the convective scale is crucial to the dynamics of tropical disturbances.

Thesis Supervisors: Frederick Sanders and Norman A. Phillips

Title: Professors of Meteorology

To Mom and Dad

ACKNOWLEDGMENTS

The author extends his sincere appreciation to his thesis advisors, Professors Norman A. Phillips and Frederick Sanders, for their advice, guidance and patience throughout the long course of this research. Many stimulating discussions with others at MIT added to this research. Financial support for the author during his stay at MIT came in part from a NASA Traineeship and from research assistantships supported by NSF grants GA 28724X and GA 27908X, and by NOAA grant E-22-37-71(G). Computing was done at the MIT Information Processing Center with funds provided by the Department of Meteorology.

The opportunity to observe tropical weather first hand and to exchange ideas with other enthusiasts was provided to the author during several summers with NOAA's National Hurricane Research Laboratory. He is particularly glad to have had the opportunity to participate in a variety of research missions flown by the NOAA Research Flight Facility.

The author is grateful to Dr. Edward Zipser of the National Center for Atmospheric Research (sponsored by the National Science Foundation) for inviting him to visit NCAR briefly in 1971 for a valuable exchange of ideas.

The final draft was ably typed by Mrs. Carla Jacobson. Typing by Mrs. Dorthea Runge, Mrs. Ina Couture, and Mrs. Diana Bristol is also acknowledged. Mr. Rob Lauden, aided by Mr. Ken Field, drafted the figures.

The author acknowledges the forebearance of his colleagues at Iowa State University during the final stages of this research.

The author is deeply appreciative of the love and patience of his wife, Judy, during the past four years, and to his parents for providing financial support at critical moments.

Finally, he acknowledges God's grace in granting him this opportunity to study and explore one element of His creation and the perseverence to complete this work.

TABLE OF CONTENTS

ABSTRACT 2
DEDICATION 4
ACKNOWLEDGMENTS 5
TABLE OF CONTENTS 7
LIST OF FIGURES 9
LIST OF TABLES 12
LIST OF IMPORTANT SYMBOLS 13

1. INTRODUCTION 17

2. NUMERICAL MODEL DESIGN 25
   2.1 Solution procedure 27
   2.2 Non-convective subgrid-scale processes 31
   2.3 Parameterization of cumulus convection 33
      2.3.1 Ensemble of convection clouds 33
      2.3.2 Ensemble influence upon the large scale 41
   2.4 Water budget 44

3. ADVENTURES IN INITIALIZATION 51
   3.1 Temperature, relative humidity, and geostrophic wind 51
   3.2 Calculation of divergent horizontal flow 54
      3.2.1 Incorporation of surface friction 55
      3.2.2 Incorporation of cumulus-convection heating and computation of final u 63

4. NUMERICAL MODEL RESULTS: CASES WITHOUT VERTICAL SHEAR OF THE ZONAL GEOSTROPHIC WIND 65
   4.1 N1 and N2: The basic no-shear experiments 68
      4.1.1 Narrowing and weakening of the large-scale disturbance 78
      4.1.2 Parameterized convection and comparison with observation 90
      4.1.3 Internal gravity waves below 50 cb 108
      4.1.4 Large-scale cloud and precipitation 110
   4.2 Experiment N3: β = 1.5 117
   4.3 Conclusions from no-shear computations 125

5. NUMERICAL MODEL RESULTS: CASES WITH VERTICAL SHEAR OF THE ZONAL GEOSTROPHIC WIND 130
   5.1 Free parameters and initial conditions 130
   5.2 Runs with and without large-scale precipitation evaporation: β = 1.35 136
      5.2.1 Time history of experiments S1 and S2 136
      5.2.2 The experiment S1 mesohigh 149
      5.2.3 Anvil circulation, experiments S1 and S2 152
      5.2.4 Comparison with observation 155
   5.3 Experimental results: β = 1.0 163
      5.3.1 Experiments S3 and S4: analogs to S1 and S2 163
      5.3.2 Experiments S5 and S6: k_{ecm} and a 170

6. CONCLUSIONS AND SUGGESTIONS FOR FUTURE RESEARCH 177
6.1 Summary and conclusions 177
6.2 Suggestions for future research 183

APPENDICES

Appendix A. Energy and the constraints on the domain average of u and v 187
Appendix B. Computation of C_θ, C_r and C_v 190
Appendix C. Consequences of assuming fractional cloud area is negligable 192
Appendix D. Fallout of precipitation: numerical procedures 195
Appendix E. A_c and E_p computation procedure and truncation error 199

REFERENCES 202

BIOGRAPHICAL NOTE 207

LIST OF FIGURES

Figure		Page
1-1	Typical schematic Θ_E-profiles.	18
1-2	Schematic cross sections through the Line Islands disturbance.	21
2-1	Domain, boundary conditions, vertical grid spacing and layers of influence of subgrid-scale eddy momentum ("friction") and water-vapor transports.	30
2-2	The "growing" and "mature" cloud components and their sum.	40
3-1a	Initial temperature sounding used in production runs.	52
3-1b	Initial humidity sounding used in production runs.	53
3-2	Major results of dry-run tests.	59
4-1	ν at 0 hours for all no-shear runs.	67
4-2	ω at 0 hours, run N1.	67
4-3	The partitioning of the initial ω, experiment N1.	70
4-4	ω at three-hour intervals, experiment N1.	71
4-5	Domain water budget for run N1, by three-hour periods.	73
4-6	ν, experiment N1.	79
4-7	Upward mass flux through 90 cb within the large-scale disturbance as a function of time, runs N1 and N2.	81
4-8	Comparison of the last four terms in (4.1), experiment N1.	83
4-9	As figure 4-8, experiment N2.	86
4-10	$\overline{\phi} - \hat{\overline{\phi}}$, experiment N1.	89
4-11	Experiment N1 heat budget in gridcolumn centered at 462.5 km, for the first three hours.	93
4-12	Experiment N1 water vapor budget in gridcolumn centered at 462.5 km, for the first three hours.	97

Figure		Page
4-13	Normalized in-cloud mass flux, , derived from the observational studies of table 6.	104
4-14	Comparison of the heating produced by convection as determined from various studies.	105
4-15	Comparison of the rates of change in large-scale water vapor produced by convection, as determined from various studies.	106
4-16	Step-by-step plots of θ , ω , r_L , and r_p at χ = 462.5 km.	111
4-17	Large-scale cloud, ageostrophic streamfunction, and isotherms of cooling by evaporation of large-scale precipitation during the preceding three hours, for run N1.	114
4-18	ω during experiment N3.	118
4-19	As figure 4-8, experiment N3.	120
4-20	As figure 4-11, experiment N3.	123
5-1	Zonal geostrophic wind, shear experiments.	133
5-2	Initial frictional plus baroclinic at various levels, shear computations.	134
5-3	Initial ageostrophic streamfunction, runs S1 and S2.	137
5-4	Ageostrophic streamfunction, large-scale cloud, and isotherms of cooling by evaporation of large-scale precipitation during preceding 3 hours, for runs S1 and S2.	138
5-5	$\Phi - \hat{\Phi}$, experiments S1 and S2.	141
5-6	θ_E cross-sections, experiments S1 and S2.	144
5-7	Comparison of disturbance θ_E -profiles.	159
5-8	As figure 5-4, runs S3 and S4.	164
5-9	As figure 5-4, run S5.	171

Figure		Page
D-1	Plot of $\omega_p = 285\, \rho^{.625}\, \rho_0^{0.5}\, r_p^{.125}$ with pressure for a typical range of precipitation-water mixing ratio (r_p) in our experiments.	196
D-2	Exact and Marchuk finite-difference solutions to (2.8) with ω_p = 0.05 cb sec^{-1} and $A = 0 = E_p$.	197

LIST OF TABLES

Table		Page
1.	Computational outline and role of thermodynamic and cloud processes involved in advancing the basic variables to time step $n+1$.	28
2.	Parameters which are identical for all production runs.	50
3.	Summary of input constants and friction-initialization strategy used in "dry-run" initialization tests.	57
4.	Free parameter values in no-shear runs.	66
5.	Supporting and supplementary data for figures 4-4 and 4-17.	76
6.	Observational studies of cumulus ensembles.	98
7.	Comparison of various N1 results with observation.	100
8.	Free parameter values in shear runs.	135
9.	Supporting and supplementary data for figures 5-4, 5-5 and 5-6.	146
10.	Interpolated positions (km) of low-level mesosystem features, run S1.	151
11.	Liquid-water budget for large-scale cloud, experiment S1.	153
12.	Comparison of S1 with the disturbances reported by Zipser (1964) and Riehl (1965, 1969).	157
13.	Supporting and supplementary data for figure 5-8.	168
14.	Supporting and supplementary data for figure 5-9.	173

LIST OF IMPORTANT SYMBOLS

Symbol	Definition
A	Rate (per unit mass of dry air) of formation of large-scale precipitation by autoconversion plus collection.
a	Autoconversion coefficient.
A_c	"Collection" (per unit mass) of cloud liquid water by precipitation.
A_u	"Autoconversion" (per unit mass) of cloud liquid water to precipitation.
C_r	Rate of change of r contributed by convection.
C_w	Rate of change of r_w contributed by convection, excluding evaporation of detrained liquid water.
C_θ	Rate of change of θ contributed by convection, excluding evaporation of detrained liquid water.
D	Raindrop diameter.
E_c	Rate of evaporation of detrained convective-cloud liquid water.
E_ℓ	Rate of evaporation of large-scale cloud liquid water.
E_p	Rate of evaporation of large-scale precipitation.
$\mathcal{E}$	Empirical coefficient in formula for evaporation from a single raindrop.
F_w	Rate of increase of water-vapor mixing ratio as a result of water-vapor accession from the sea.
F_x	x -component of frictional force.
F_y	y -component of frictional force.
L	Latent heat of condensation, 2.501×10^6 K_j ton^{-1}.
M_c	Upward mass flux within convective clouds averaged over a horizontal "gridsquare." $M_c = \ell m$
$\bar{M}$	Total upward mass flux ("large-scale") averaged over a horizontal "gridsquare."

Symbol	Definition
q_m	Upward mass flux within convective clouds if all such clouds had top at p_t .
N_0	Parameter in Marshall-Palmer drop-size distribution.
P	p / p_{00}
R	Specific gas constant for dry air, 287.05 Kj ton^{-1} C^{-1}.
T	Temperature.
a	Cross-section area of convective cloud.
b	Radius of convective cloud. In chapter 3, only, it is ratio of "geostrophic scale height" to density scale height.
c_p	Specific heat of dry air at constant pressure, 1004.25 Kj ton^{-1} C^{-1}.
f	Coriolis parameter.
g	Acceleration of gravity, 9.8 m sec^{-2}.
k	Cloud-top distribution function.
k_m	Fraction of total cloud population which is "mature."
p	Pressure.
p_b	Cloud base pressure.
p_t	Pressure at maximum cloud top within a particular grid-column.
p_1	Level at which rising air in convective clouds first loses positive buoyancy.
p_∞	100 cb.
q	Dummy variable.
r	Large-scale water-substance mixing ratio. $r = r_v + r_l$.
r_l	Large-scale cloud-water mixing ratio.
r_{lc}	Liquid-water mixing ratio within convection clouds.

Symbol	Definition
r_{lcm}	Maximum allowable liquid-water mixing ratio within convective clouds.
r_p	Mixing ratio of large-scale precipitation.
r_s	Saturation mixing ratio.
r_v	Mixing ratio of large-scale water vapor.
t	Time.
u	x -component of velocity (zonal wind).
u_g	Zonal geostraophic wind.
v	y -component of velocity.
v_g	y -component of geostrophic velocity.
x	East-west coordinate, increasing east.
y	North-south coordinate, increasing north.
β	Ratio of upward mass flux through convective-cloud base to large-scale upward mass flux at 90 cb.
Δt	Computational timestep.
Δx	Horizontal grid increment.
η	Fractional gridsquare area covered by convective clouds.
θ	Potential temperature.
θ_E	Equivalent potential temperature.
χ	R/c_p
ν	Coefficient of vertical kinematic eddy viscosity
ρ	Air density.
ρ_s	Standard density.
ρ_0	Standard density at 100 cb.
τ_A	Microphysical time scale.
τ_s	Time it takes a parcel to traverse concentrated-detrainment region.

Symbol	Definition
Φ	Geopotential.
ω	Individual rate of change of pressure.
ω_p	Fall speed of large-scale precipitation.
$(\ )_c$	In-cloud value of ( ) [excepting M_c].
$(\ )_e$	Environment value of ( ).
$\bar{(\ )}$	The horizontal average of ( ) over a "gridsquare."
$\hat{(\ )}$	χ -average of ( ).
$(\ )'$	Individual change of ( ).

1. INTRODUCTION

Various case studies of certain tropical weather disturbances have suggested that appreciable downward mass flow from mid-troposphere to the lower troposphere must occur within the rain areas of these (for example, Riehl, 1965; Riehl and Pierce, 1968; Riehl, 1969; Zipser, 1969). This has been inferred indirectly by noting that low-tropospheric values of the quasi-conservative thermodynamic quantity, equivalent potential temperature, θ_E , of air which has passed through the rain areas of such disturbances is abnormally low (see figure 1-1). It is clear from observed lower tropospheric temperature and water vapor within these rain areas that much of this subsidence is in response to cooling of unsaturated air by evaporation of cloud or precipitation water substance.

It is commonly observed that downdrafts on a convective time and space scale (say, 15 minutes and 2000 meters) normally accompany rainfall from cumulus and cumulonimbus clouds. The coolness and dryness of these downdrafts attest to their mid-tropospheric source. Unquestionably there existed in the tropical disturbances in question heavy rain showers and squalls of cumulonimbus origin. Therefore, the observed θ_E-redistribution could have been accomplished by cumulonimbus downdrafts.

There is evidence, however, to suggest that a significant fraction of the water substance carried upward in cumulonimbus updrafts remains suspended in cloud droplet or ice crystal form in middle or upper troposphere for a sufficient length of time to form, usually in the presence of vertical shear of the horizontal wind between lower and upper troposphere, an

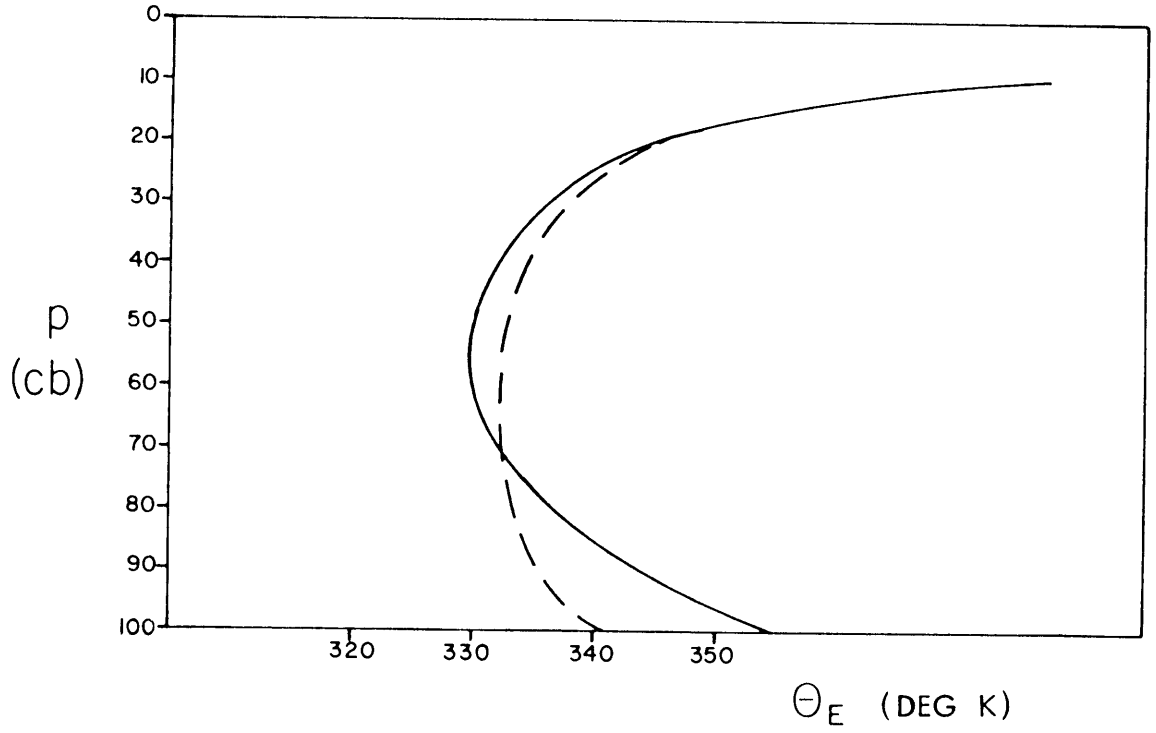


Figure 1-1. Typical schematic Θ_E-profiles: in the undisturbed tropical atmosphere (solid curve), and within air which has just passed through a disturbance (dashed). (After Riehl and Pierce, 1968)

extensive sheet or layer of precipitating middle cloud (specifically, altostratus[1] cumulonimbogenitus and nimbostratus cumulonimbogenitus). Precipitation falling from such a cloud mass will experience evaporation as it plunges toward Earth, the heat required for the evaporation coming from the air through which the precipitation passes. Clearly, if there is sufficient evaporation the motion field will respond.

Riehl (1965, 1969), concerning a westward-moving tropical wave in the Caribbean Sea, and Zipser (1969), with respect to a disturbance in the Line Islands, have been the strongest proponents of the importance of this process. Zipser had more data on which to base his analysis than did Riehl, and it was the author's good fortune to be able to speak with him and to view the ground-based time-lapse movie film taken at Palmyra Island.

The exact beginnings of the Line Islands event are obscure, but it is likely that convective-scale negatively buoyant downdraft air from an active cluster of cumulonimbi spread out laterally as it impinged on the sea surface to form a "mesohigh" with a "pseudo-cold front" along its leading (western) edge. This process happens frequently in mid-latitude squall lines (e.g., Fujita, 1963). The "cold front" was the scene of local strong low level convergence between the ambient undisturbed flow and the more rapidly westward moving downdraft air behind it, and therefore was likely a

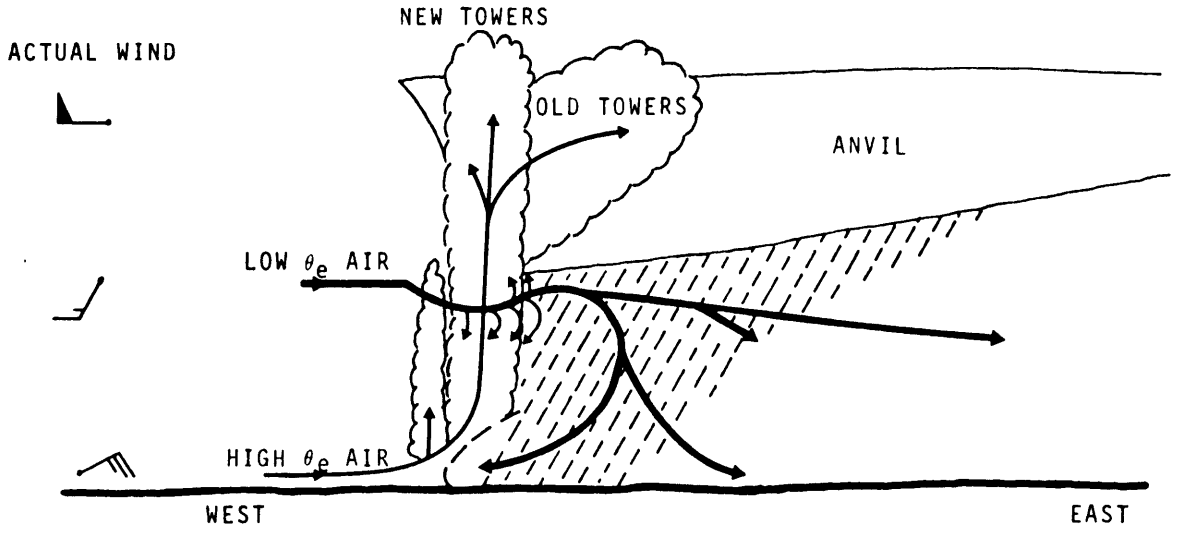
---

[1] A ground-based observer using the WMO Cloud Code should code the sky C_M 7, thick altostratus with some altocumulus present, or, if no altocumulus, then C_M 2, altostratus and/or nimbostratus. Altostratus or nimbostratus being the predominant genus present should not be construed as indicating that this "anvil" is free of substantial vertical motions. To the contrary, upward motion, on the convective-scale or some larger scale, is almost certainly present within it and prolongs its life as a precipitation producer.

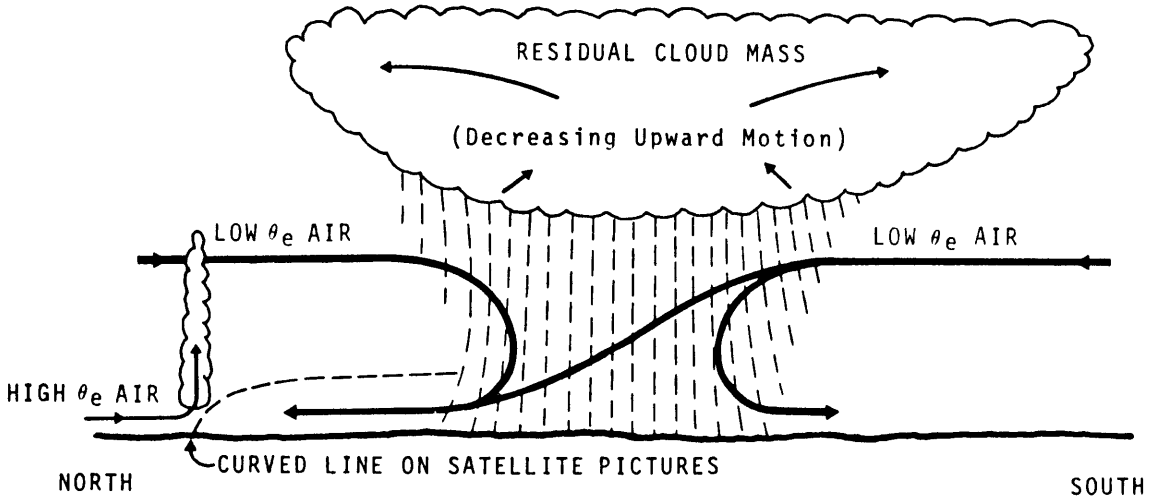
"trigger" for continued cumulonimbus convection. The persistent convection together with the appreciable vertical shear produced, within a few hours, a thick layer of precipitating altostratus. This stage in the life history of the Line Islands disturbance is depicted in figure 1-2a. The low θ_E-air behind the "cold front" was observed to be almost entirely devoid of cumulus convection.

Subsequently, the leading edge of the downdraft air continued to progress westward and northwestward but the convection along its leading edge gradually lost its vigor. Figure 1-2b is a schematic presentation of the structure of the disturbance six to eight hours after figure 1-2a. By this time cumulus convection was probably too weak to produce significant downdrafts. The cloud band marking the leading edge of the downdraft air could be seen on ATS-I satellite pictures as a thin arc extending for a length of over 500 km. The pictures suggest that as much as 2×10^5 km^2 of the ocean surface may have been covered by downdraft air.

It is mainly the occurrence of precipitation from the extensive altostratus deck and the distinctly <u>mesoscale</u> ($\sim$100 km) rather than convective-scale character of the low level motion field that led Zipser to the conclusion that significant subsidence occurred on the mesoscale underneath this cloud layer. There were neither liquid-water-content measurements within the altostratus layer nor sufficiently detailed surface precipitation data available to aid in estimating how much altostratus precipitation might have evaporated as it fell. In fact, the author knows of no meteorological dataset suitable for quantitatively measuring or estimating the mass transports by such mesoscale downdrafts, or for estimating the amount of precipitation evaporation under such an altostratus layer.



a. Formation of the altostratus cumulonimbogenitus anvil and evaporation induced downdraft.



b. Six to eight hours after part a. The east-west section at this time would appear similar except that all low θ_e-air flowing underneath the "residual cloud mass" would be coming from the west.

Figure 1-2. Schematic cross-sections through the Line Islands disturbance (after Zipser, 1969, figure 15). Streamlines are relative to the moving cloud system.

A very crude estimate of the order of temperature and pressure changes that might occur as the direct result of evaporation is as follows. Consider a cloud-free region extending from the base of the altostratus "anvil" to the sea surface, of depth Δp. Assume that an amount of precipitation, $2R$ (tons per square meter), falls out of the base of the anvil, and that one-half of this evaporates as it falls, the other half reaching the surface. If it is assumed that this evaporation is isobaric then for the layer as a whole, $(\Delta p/g) c_p \Delta T = -L R$, or, $\Delta T = -(L/c_p)(g/\Delta p) R$, where L = latent heat of condensation, taken throughout this study to be 2.501×10^6 kj ton^{-1}, and c_p = specific heat at constant pressure, 1.00425×10^3 kj ton^{-1} C^{-1}. A rainfall of 2.5 mm (0.10 inch) during a 1-2 hour period is in my experience not an unusual amount of rainfall from cumulonimbi debris after the parent clouds have dissipated. Taking $R = 2.5 \times 10^{-3}$ ton m^{-2} and $\Delta p = 35$ centibars (as per Riehl's, 1965, estimate of the base of the "anvil"), we have $\Delta T \approx -(2.5 \times 10^3) \times 2.5 \times 10^{-3} \times (10/35) \approx -1.80$ C as an <u>average</u> temperature drop for the whole layer. The corresponding virtual temperature change is -1.67 C which implies hydrostatically a 100 to 65 cb layer thickness decrease of about 22 meters, or a surface pressure rise of 2.5 mb if the level of the 65 cb pressure surface is unaffected. To this the atmosphere would surely respond in a detectable manner.

In view of these considerations the author was (and is) sufficiently impressed to explore the matter in more detail. To wit, a time-dependent numerical model has been designed to test the working hypothesis that evaporation of precipitation falling from widespread sheets of altostratus

cloud (which is a by-product of cumulonimbus convection) is sufficient to produce a mesoscale downdraft having sufficient strength and persistence to (a) alter the θ_E - profile so that it resembles observed disturbance profiles exemplified by figure 1-1, and to (b) alter the dynamics of the large scale to the extent that to ignore such evaporation is to make a qualitative error.

This is one of the few numerical studies of mesoscale convection phenomena other than tropical storms and hurricanes, and fronts. The early work of Sasaki (1962) and Ogura and Charney (1962) in essence explores the propagation of a gravity wave through a conditionally unstable air mass, and is inspired by the pressure jump theory of squall-line formation. Ogura and Charney's model does not allow precipitation of condensate to occur and the precipitation of Sasaki's does not evaporate. Schlesinger (1973 a,b), in applying the non-hydrostatic anelastic equations (Ogura and Phillips, 1962) to a two-dimensional domain with horizontal dimension 180 km, finds that a single convective cell growing in strong shear can produce a cumulonimbus anvil with horizontal dimension approaching 100 km. His parameterization of microphysical precipitation and evaporation processes is inadequate for testing of the hypothesis under scrutiny in this study.

Since the mesoscale (i.e. large-scale) downdrafts to be studied have a horizontal scale an order of magnitude larger than the vertical, we use the hydrostatic unfiltered (sometimes referred to as the "primitive" or "PE") equation set. It is thus necessary to parameterize the influence which the non-hydrostatic cumulus convection has upon the evolution of the explicitly

described "large-scale" flow. In addition, there is an explicit large-scale water budget, including cloud and precipitation and microphysical precipitation processes. These aspects of the model are presented in chapter 2.

Chapter 3 deals with the problem of establishing a satisfactory initial state for the model time integration. In chapter 4 the results of integrations in which there is no vertical shear of the basic zonal wind are presented, with emphasis on the workings of the parameterization of convective heating, and the microphysical parameterization in the water budget. Chapter 5 contains the results of the integrations in which shear of the zonal wind is present. We examine these in light of our working hypothesis. In chapter 6 the discussion centers around topics in which further research is needed if models such as the present one are to yield more definitive results.

2. NUMERICAL MODEL DESIGN

Our experimental domain is a flat plane rotating at an angular velocity $f/2$. In order to simplify the complete equations governing the flow in this domain into a set which is manageable yet capable of accurately describing the large-scale quasi-hydrostatic motion, we (a) replace the vertical momentum equation by the hydrostatic relation and express the remaining equations in the (x , y , p , t) coordinate system, and (b) restrict the horizontal variation of all dependent variables to be in the x-direction only, with the exception of θ , potential temperature, and Φ , geopotential. The resulting equation set is given below.

$$\frac{\partial u}{\partial t} = -\frac{\partial}{\partial x}(uu) - \frac{\partial}{\partial p}(\omega u) - \frac{\partial \Phi}{\partial x} + fv + F_x \tag{2.1}$$

$$\frac{\partial v}{\partial t} = -\frac{\partial}{\partial x}(uv) - \frac{\partial}{\partial p}(\omega v) - \frac{\partial \Phi}{\partial y} - fu + F_y \tag{2.2}$$

$$0 = -\frac{\partial \Phi}{\partial p} - c_p \theta \frac{d P^x}{d p} \tag{2.3}$$

$$0 = \frac{\partial u}{\partial x} + \frac{\partial \omega}{\partial p} \tag{2.4}$$

$$\frac{\partial \theta}{\partial t} = -\frac{\partial (u\theta)}{\partial x} - v\frac{\partial \theta}{\partial y} - \frac{\partial}{\partial p}(\omega \theta) - \frac{L}{c_p}\bar{P}^x\left[E_l + E_p + E_c\right] + C_\theta \tag{2.5}$$

$$\frac{\partial r}{\partial t} = -\frac{\partial}{\partial x}(ur) - \frac{\partial}{\partial p}(\omega r) + F_{rv} - A + E_p + C_r \qquad (2.6)$$

$$\frac{\partial r_v}{\partial t} = -\frac{\partial}{\partial x}(u r_v) - \frac{\partial}{\partial p}(\omega r_v) + F_{rv} + E_l + E_p + E_c + C_{rv} \qquad (2.7)$$

$$\frac{\partial}{\partial t} r_p = -\frac{\partial}{\partial p}(\omega_p r_p) + A - E_p \qquad (2.8)$$

We define P as p/p_{00}, p_{00} being 100 cb. All other symbols in the dynamical equations have their standard definitions. The thermodynamic equation (2.5) and the water budget equations (2.6) - (2.8) have appended to them source and sink terms arising from convective cloud influences and microphysical precipitation processes. r is the sum of the large-scale water vapor mixing ratio, r_v, and the cloud water mixing ratio, r_l. [Small approximations are made in (2.6) and (2.7) by using mixing ratio instead of specific humidity, $q \equiv r/(1+r)$, and in (2.3) by ignoring virtual temperature effects.] ω_p is rate of fall of precipitation with mixing ratio r_p, A is the autoconversion rate of large-scale cloud to precipitation and the collection of cloud by precipitation, E_p is the evaporation of precipitation that falls from large-scale cloud and E_l is the evaporation of large-scale cloud. ω_p, A and E_p are discussed in section 2.4. The quantities C_θ, C_r, C_{rv} and E_c represent large-scale changes due to convective cloud parameterization, and are discussed in section 2.3.

2.1 Solution procedure

The large-scale variables to be forecast are u, v, θ, r, t_v and t_p, as shown in the above equations. "Thermodynamic" processes involved in prediction of θ, r, t_v and t_p can be separated into (a) those associated with large-scale precipitation, t_p, i.e., (A, E_p), and (b) all others (large-scale lifting to saturation and the effects of cumulus convection), i.e., E_l, C_θ, C_r, C_v and E_c. Specific formulae for individual rates of change are used only for A and E_p. Mutual adjustment to saturation conditions of tentatively predicted supersaturated values of θ and t_v is accomplished by the isobaric "wet-bulb" process (MacDonald, 1963) as may be required by process (b) instead of using, for example, the rate formula $\dot{\theta} \propto \omega$ times the moist-adiabatic lapse rate. The variables E_c and E_l symbolize this adjustment process.

The time stepping procedure uses successive time steps $t = n\Delta t$, based for the most part on the leap-frog scheme $f_{n+1} = f_{n-1} + 2\Delta t \dot{f}_n$. Table 1 lists the sequence of steps by which the basic variables (u, v, θ, r, t_v and t_p) are advanced to $n+1$ using the values of $n-1$ and n. The only exceptions to the leap-frog procedure are in vertical diffusion, fallout of r_p (see section 2.4) and in the effect of convection (step 7). In step 7 the leap-frog time extrapolation from $n-1$ to $n+1$ resulted in separation of solutions at even and odd time steps if step 7 used only the results of step 1 at n. This sensitivity appeared to be associated with oscillations of convective cloud tops just above and just below one of the

.. Computational outline and role of thermodynamic and cloud processes involved in advancing th basic variables to time step $n+1$.

Step	Forecast variable and equation			
Description	θ (2.5)	r (2.6)	r_v (2.7)	r_p (2.8)
Compute cumulus properties for $t = n\Delta t$	--	--	--	--
Predict $(u, v)_{n+1}$	--	--	--	--
Predict $(r_p)_{n+1}$ as affected by fallout	--	--	--	ω_p
Correct $(r_p)_{n+1}$ for autoconversion, collection and evaporation	--	--	--	A, E_p
Predict $(\theta, r, r_v)_{n+1}$ as affected by large-scale advection, vertical diffusion and consequences of step 4	E_p	A, E_p	E_p	--
First saturation adjustment of $(\theta, r_v)_{n+1}$, for diagnostic purposes	E_l	--	E_l	--
lodify $(\theta, r, r_v)_{n+1}$ using result of tep 1 for n and for $n-1$	C_θ	C_r	C_v	--
inal saturation adjustment for $(\theta, r_v)_{n+1}$	E_c	--	E_c	--

pressure levels of the model. It was eliminated by averaging the results of step 1 for n and $n-1$ in going from $n-1$ to $n+1$.

In order to simplify matters further we consider only solutions such that, for q any dependent variable other than Φ, $q(x, p, t) = q(x + L_x, p, t)$, where L_x = 1000 km. Our domain is thus confined to a 1000 km long vertical cross-section through the atmosphere in which (2.1) - (2.8) is solved subject to the constraint that the mass-weighted average of v is always 0, and that the mass-weighted average of u is constant (not necessarily 0) in time (see figure 2-1). For our governing equations to conserve total energy in adiabatic reversible flow, it is necessary to take $\partial\theta/\partial y$ as constant in x and p; it is assumed constant with time as well. These constraints are similar to those imposed in a model designed by Williams (1967) for the study of two-dimensional frontogenesis.

At the bottom boundary, $p = p_{00}$, we take $\omega = 0$. The lower boundary condition on Φ in (2.3) is provided by the constraints on the domain averages of u and v.

We integrate the governing equations by finite difference procedures. The domain is partitioned into 40 x 19 = 760 grid rectangles defined by increments of 25 km in x and 5 cb in p (figure 2-1). All dependent variables except ω are carried at the mid-points of these, following Lorenz (1960). The finite difference analogues of the advection terms in (2.1), (2.2), (2.5), (2.6) and (2.7) are written in flux form (see, e.g., Bryan, 1966), but a special device is used in (2.8), see section 2.4. For additional details consult Appendix A.

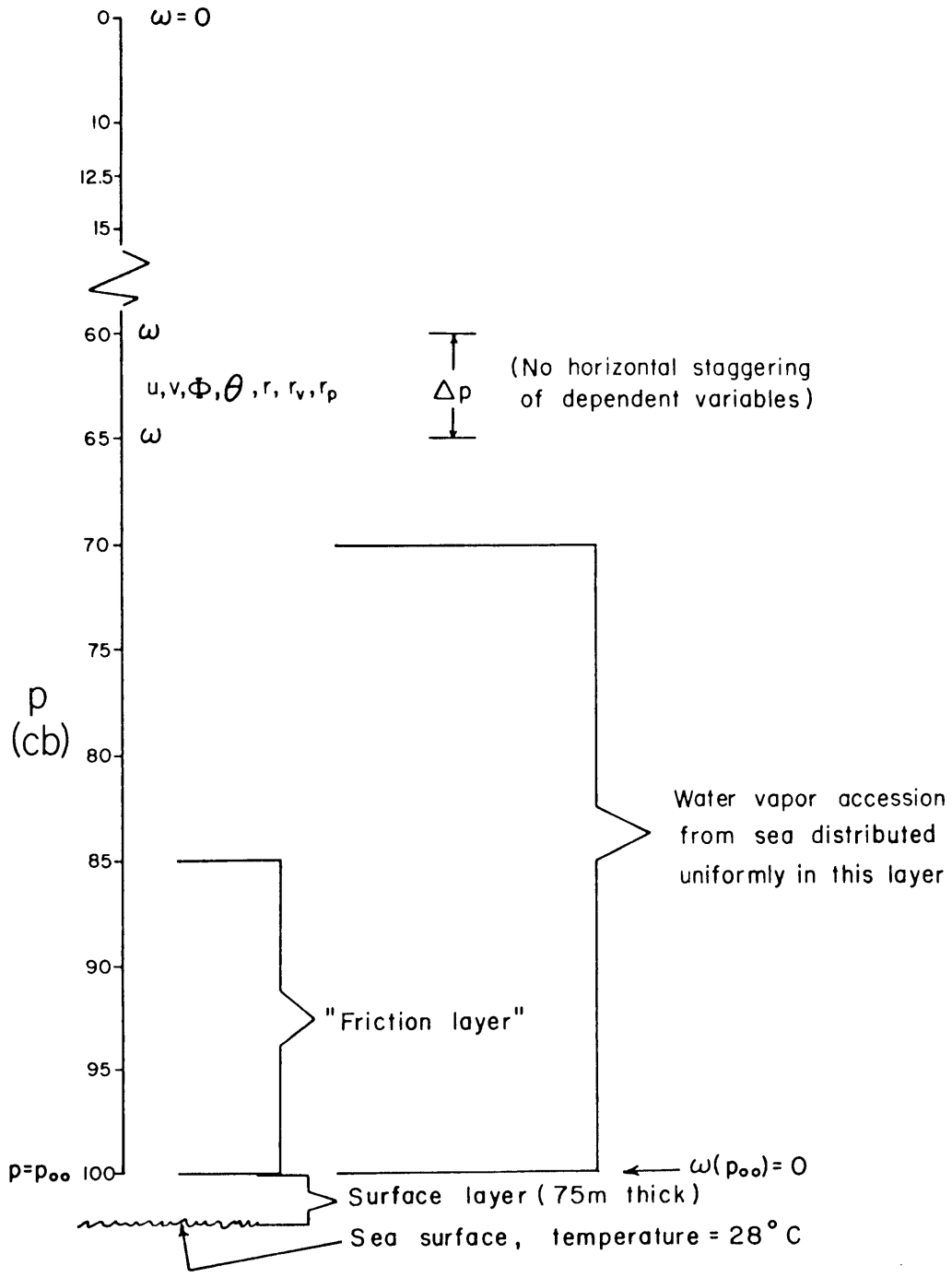


Figure 2-1. Domain, boundary conditions, vertical grid spacing and layers of influence of subgrid-scale eddy momentum ("friction") and water vapor transports.

2.2 Non-convective subgrid-scale processes

In the atmosphere the influence of momentum loss and heat and moisture accession by air adjacent to the sea is spread through the lowest several hundred meters by the action of small-scale "eddies." We parameterize the transport of momentum and water vapor by these eddies using standard procedures. Heat accession and transport are ignored since in the tropics the Bowen ratio is generally $<<$ 1.

The $p = p_\infty$ pressure surface is taken as the top of a neutrally buoyant constant stress and constant eddy-water-vapor-flux layer of depth 75 meters. To wit,

$$(\tau_{xz}, \tau_{yz}) = c_D \rho_0 |V| (u, v)$$

and

$$\mathcal{R} = c_D \rho_0 |V| (r_v(p_\infty) - r_{sea}) ,$$

where τ_{xz} and τ_{yz} are the x and y-components of the surface stress, and $\mathcal{R}$ is the surface flux (positive if downwards) of r_v and r. The velocity at 100 centibars, V, is linearly extrapolated from grid values at 92.5 and 97.5 centibars. The drag coefficient, c_D, assigned the magnitude 10^{-3}, may be thought of as appropriate to 75 meters. With a logarithmic wind profile and roughness length of 0.1 cm, this is

equivalent to a 10 meter drag coefficient of 1.5×10^{-3}, consistent with reported measurements by Pond et al. (1971), for example.

Above p_∞, the eddy stresses are written

$$(\tau_{xz}, \tau_{yz}) = -\rho_s^2 g \, \ell^2 \left(\frac{\partial u}{\partial p}, \frac{\partial v}{\partial p}\right),$$

with

$$(F_x, F_y) = -g \frac{\partial}{\partial p}(\tau_{xz}, \tau_{yz}) .$$

ℓ at 100 cb is assumed equal to the Von Karman constant times the depth of the (neutral) constant stress layer times the surface friction velocity. Above p_∞, ℓ decreases monotonically to 0 at 85 cb:

$$\ell = 0.4(75)\left(\frac{|\tau|_{100\,cb}}{\rho_0}\right)^{1/2} \left[\frac{1 - \frac{\ln p}{\ln 100}}{1 - \frac{\ln 85}{\ln 100}}\right], \quad 85\ cb \le p \le p_\infty,$$

= 0 otherwise. The choice of 85 cb as the top of the friction layer was made mainly on the basis of experimentation with various initialization procedures, reported in chapter 3.

The eddy water vapor flux is treated as suggested by Miller et al. (1972), i.e., by assuming a linear decrease of $|\tau|$ from the 100 cb

value defined above to 0 at 70 cb. F_ν is then given by $-g\,\partial \mathcal{R}/\partial p$.

Certainly these formulations of F_x, F_y and F_ν are vulnerable, e.g., static stability could have been accounted for in the formulation of ν. However, the above formulas are considered sufficiently accurate for our purpose, to qualitatively model the influence of surface friction and moisture accession.

2.3 Parameterization of cumulus convection

Many schemes have been proposed, but in my opinion only recently, with the work of Arakawa (1971), and Arakawa and Schubert (1974) has the parameterization problem been put on a sound physical basis. When this project was started (1970), none of the procedures then available (see Bates, 1972, for a concise review) seemed readily adoptable to the requirements of this study, in particular that of including an explicit computation of liquid water transport by the cumulus. Therefore, I designed a new one. It is similar to the more straightforward aspects of the Arakawa scheme (though arrived at independently).

2.3.1 Ensemble of convective clouds

In this section we indicate the attributes of our idealized cloud ensemble.

(a) The cumulus properties are computed using a conventional plume model. Such models do not include downdrafts.

(b) Let M_c and $\bar{M}$ be defined as the following upward mass fluxes per unit area, averaged horizontal over a "grid square," having area A_{grid} :

$$M_c = \frac{1}{A_{grid}} \int \rho w \, dA_{cloud}$$

$$\bar{M} = \frac{1}{A_{grid}} \int \rho w \, dA_{grid}$$

M_c is the average value of $\rho w \approx -\omega/g$ inside convective clouds multiplied by the percentage area covered by the clouds, whereas $\bar{M}$ is equal to $-\bar{\omega}/g$, $\bar{\omega}$ being the large-scale ω appearing in (2.4). From the above definitions we have

$$\frac{1}{A_{grid}} \int \rho w \, dA_{env} = \bar{M} - M_c . \qquad (2.9)$$

Defining p_b as cloud base pressure, we assume

$$M_c(p_b) = \beta \bar{M}(90\ cb) , \quad \bar{M}(90\ cb) > 0,$$

(2.10)

= 0 (i.e., no clouds), otherwise.

A value of one for β (typical of all earlier parameterizations) therefore implies no vertical motion at cloud base level in the cloud environment if

cloud base happens to also be at 90 cb. A larger value for β implies subsidence in the environment, a feature which is now thought to be important (chapter 4). A relation between β and convective cloud area can also be derived [equation (2.16)].

(c) Cloud base pressure, p_b, is the lifted-condensation-level (LCL) pressure of a large-scale air parcel at 97.5 cb. All clouds in a particular gridsquare are based at this pressure.

(d) At cloud base the air rising into the clouds is assumed to be neutrally buoyant with respect to the large scale. This assumption is used in estimating cloud buoyancy as a function of height and the resulting height of cloud top.

(e) The upward mass flux $m = \rho \pi r^2 w$ in an individual cloud is assumed to obey the simplified entrainment law

$$\frac{1}{m}\frac{dm}{dz} = \frac{2\alpha}{\text{radius}} = \frac{2\,(0.1)}{1\ \text{km}}, \quad p < p_b .$$

m times the number of clouds per unit area is equal to M_c:

$$M_c(p_b) = \frac{N(p)}{A_{grid}}\, m(p) . \tag{2.11}$$

(f) We ignore all influence clouds may have on the large-scale momentum budget. There is evidence (see, for example, Gray, 1967, and Simpson, 1972) that the vertical transport of momentum by cumulus clouds cannot be

ignored under all circumstances, but it seems unlikely to be of major importance for this study.

(g) Convective-cloud liquid-water mixing ratio, $r_{\ell c}$, is subject to the constraint that it cannot exceed an upper limit ($r_{\ell cm}$) which is assigned a fixed value in a given numerical integration. Any excess convective cloud condensate falls immediately to the surface without evaporation. This is the simplest possible assumption consistent with allowing convective-scale precipitation and detrainment of cloud liquid water into the environment.

(h) The plume model assumption (a) and mass continuity may be used to express the budget of the quantity q_c within an individual cloud as (ignoring pressure perturbations due to the cloud)

$$\frac{\partial}{\partial p}(m q_c) = q_e \frac{\partial m}{\partial p} - \frac{a}{g} \dot{q}_c \qquad (2.12)$$

The first term on the right hand side is the rate of entrainment of $q = q_e$ from the environment and the last term is the individual rate of change averaged over the cross-section area of the cloud, $a = \pi b^2$. In terms of the cloud potential temperature, water content, and momentum, the equations are

$$\frac{\partial}{\partial p}(m \theta_c) = \theta_e \frac{\partial m}{\partial p} - \frac{a}{g} \dot{\theta} , \quad \dot{\theta} = -\frac{L}{c_p} P^{-\kappa} \dot{r}_v \qquad (2.13)$$

$$\frac{\partial}{\partial p}(m r_c) = r_e \frac{\partial m}{\partial p} - \frac{a}{g} \dot{r} \qquad (2.14)$$

$$\frac{\partial}{\partial p}(m w) = -\frac{m}{w \rho_s}\left(\frac{\rho_e - \rho_c}{\rho_s}\right) . \qquad (2.15)$$

ρ_s is a convenient standard density and ρ_c is the cloud density including liquid water. (The condensation and precipitation processes in the first two of these are actually computed by a saturation adjustment procedure allowing for τ_{cm} .) The equations are solved with lower boundary conditions at p_b from (c) and (d) above and a w value of 1 m sec^{-1}. From (2.11), the relation $m = \rho \pi b^2 w$, $M_c = -\beta \bar{\omega}/g$, and the cloud base w of 1 m sec^{-1}, we find that the fractional area covered by convective clouds at $p = p_b$ is

$$\frac{\pi b^2 N(p_b)}{A_{grid}} \approx \frac{\beta \bar{\omega}(90\ cb)}{1\ m\ sec^{-1}} . \qquad (2.16)$$

A choice of β and a fixed value (1 m sec^{-1}) for w therefore implies a proportionality of cloud area to $\bar{\omega}$ at 90 cb.

(i) The highest cloud tops are at p_t , where w vanishes in (2.15).

(j) Convective clouds are ignored if plume buoyancy is negative at the top of the first complete 5-cb-thick computational layer above cloud base.

(k) For realism we should allow for some clouds not reaching p_t . Let $q_m(p)$ represent the value of M_c corresponding to $N(p) = N(p_b)$ in (2.11). In equations (2.12)-(2.15), q_m can then replace m , and we can define the ratio

$$k(p) = \frac{N(p)}{N(p_b)} = \frac{M_c(p)}{q_m(p)} . \qquad (2.17)$$

Let $p_1 > p_t$ be the level at which the plume first loses positive buoyancy, $h(p)$ is then assumed to be distributed as follows:

$$h = 0, \qquad p < p_t$$

$$h = (p - p_t)\left[\frac{h_m}{2(p_1 - p_t)} + \frac{1 - h_m}{p_b - p_t}\right], \qquad p_t \leq p \leq 2p_1 - p_t \tag{2.18}$$

$$h = h_m + (1 - h_m)\left(\frac{p - p_t}{p_b - p_t}\right), \qquad 2p_1 - p_t < p < p_b$$

$$h = 1 \qquad p \geq p_b$$

This specifies M_c given the solution of (2.12)-(2.15).

The choice of h_m is based upon the following physical view of the cumulus ensemble. We presume that each cloud in the ensemble has a lifetime, i.e., that at a particular instant each cloud is either growing, mature or decaying. Only growing and mature clouds contribute to M_c and are included in N. Decaying clouds are assumed to mix <u>in situ</u> with

their environment--they contain no organized updraft or downdraft motion--whereas growing and mature clouds are entraining plumes. Growing clouds detrain no mass to the environment; mature clouds detrain only at their tops which are within the layer $p_t \leq p \leq p_1 + (p_1 - p_t)$. Decaying clouds mix with the environment throughout their whole depth. Mass balance is satisfied separately for the mature and for the growing-decaying subsets of the ensemble.

The first two terms, $(p - p_t)\, k_m / [2(p_1 - p_t)]$ and k_m, contributing to k in (2.18) represent the mature clouds, and the second terms, proportional to $1 - k_m$, represent the growing clouds. At cloud base (p_t) we have the following ratio between growing and mature clouds:

$$\frac{N_{grow}}{N_{mature}} = \frac{1 - k_m}{k_m}$$

A value of 2 has been used for this ratio, giving $k_m = 1/3$. If we assume that all clouds have an identical life-history, and that the cloud population is in steady state, the choice of $k_m = 1/3$ is equivalent to assuming that all clouds spend one-half as much time in the mature stage as it takes them to grow to "maturity."

In figure 2-2 is a sample $k(p)$ distribution derived from the slightly modified (see chapter 3) Line Islands Experiment (LIE) mean of Palmyra Island's 0000Z temperature and 1200Z humidity soundings (Madden et al., 1971).

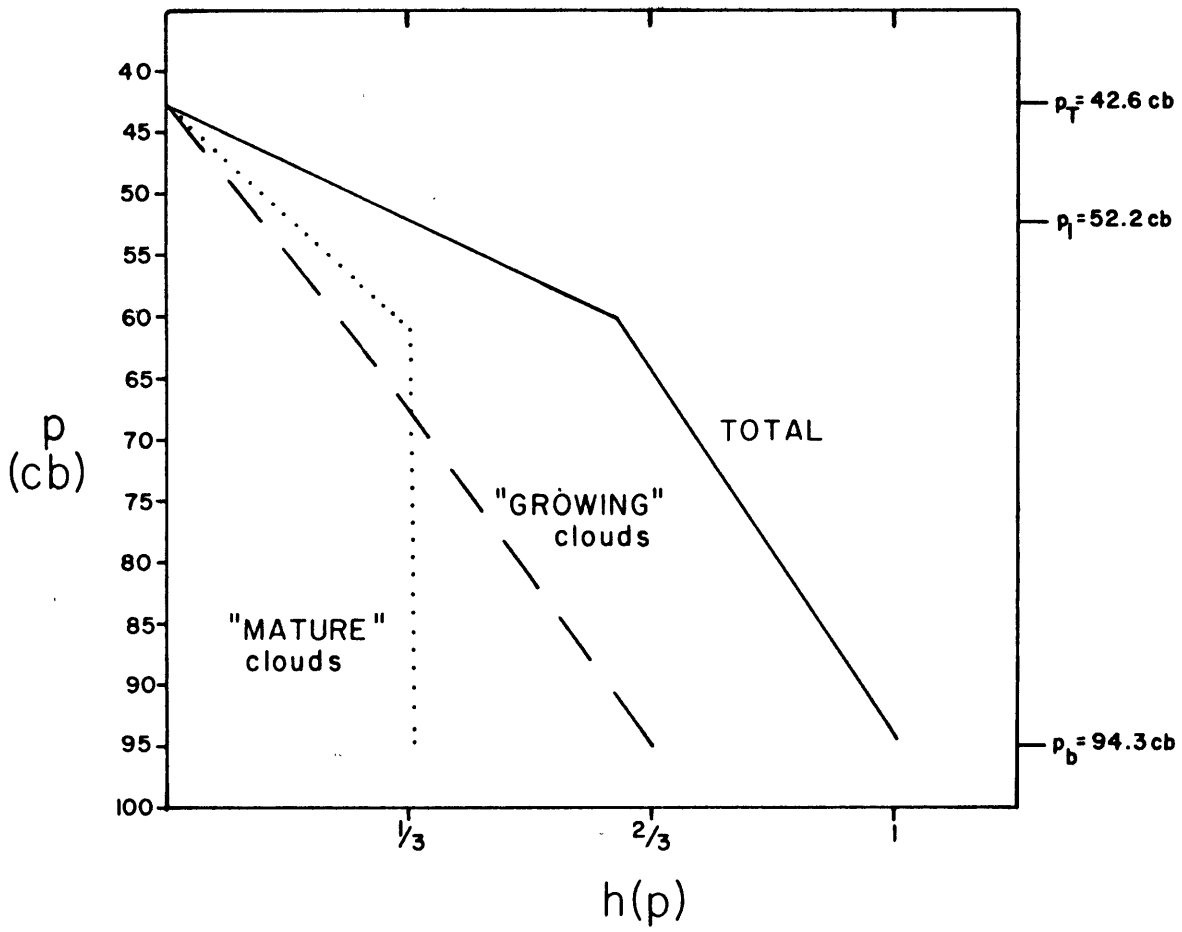


Figure 2-2. The "growing" and "mature" cloud components of $k(\eta)$, and their sum. This is based on the Palmyra 0000Z temperature and 1200Z humidity mean soundings for the Line Islands Experiment, depicted in figure 3-1, with the exception that Θ at 97.5 cb has been increased to that at 92.5 cb.

2.3.2 Ensemble influence upon the large scale

Our idealized ensemble of convection clouds affects the evolution of the large-scale flow as follows.

(a) Mass is taken from the environment at lower levels and transported to higher levels where it is put back into the environment; as mass rises in convective clouds, condensation increases its θ and decreases its r_v, and microphysical processes (g. in section 2.3.1) may decrease r as well. Outside convective clouds, mass continuity demands that there be updraft-compensating subsidence superimposed upon the large scale vertical motion, according to equation (2.9).

(b) Where detrainment occurs, liquid water is isobarically mixed into the environment, evaporating completely (and instantaneously) if the environment is not yet saturated.

Consider first the equation

$$\frac{\partial q}{\partial t} + \nabla\cdot(\mathbf{V}q) + \frac{\partial}{\partial p}(\omega q) = \dot{q}$$

where q represents θ, r or r_v. The large-scale (grid area) average of q and $\mathbf{V}$, written as $\bar{(\ )}$ contains both convective cloud, $(\ )_c$, and cloud environment, $(\ )_e$. The result of integrating the above relation over A_{grid} can be written at each pressure level as

$$\frac{\partial \bar{q}}{\partial t} + \nabla\cdot(\bar{V}\bar{q}) + \frac{\partial}{\partial p}(\bar{\omega}\bar{q}) = g\frac{\partial}{\partial p}\left[M_c(q_c - q_e) + \bar{\eta}(q_e - \bar{q})\right] + \frac{1}{A_{grid}}\left[\int \dot{q}\, dA_c + \int \dot{q}\, dA_e\right], \quad (2.19)$$

where the minor approximations are made that $\omega \approx -\rho g w$ and that $\overline{qV} = \bar{q}\,\bar{V}$. The cloud model equation (2.12) and the defintions $M_c = \rho_b \eta_b = \rho_b [N(p_b)/A_{grid}]\, m$ allow us to express the cloud integral of $\dot{q}$ as

$$\frac{1}{A_{grid}} \int \dot{q}\, dA_c = g\left[q_e \rho_b \frac{\partial \eta_b}{\partial p} - \frac{\partial}{\partial p}(M_c q_c) + q_c \eta_b \frac{\partial \rho_b}{\partial p}\right]. \quad (2.20)$$

(Recall that cloud thermodynamics is computed by isobaric adjustment rather than by using the explicit expressions for $\dot{q}$.) When substituted into (2.19) this results in

$$\frac{\partial \bar{q}}{\partial t} + \nabla \cdot (\bar{V} \bar{q}) + \frac{\partial}{\partial p}(\bar{\omega} \bar{q})$$

$$= g\left[-\frac{\partial}{\partial p}(q_e M_c) + q_e \lambda \frac{\partial \eta_u}{\partial p} + q_c \eta_u \frac{\partial \lambda}{\partial p}\right]$$

$$+ g \frac{\partial}{\partial p}\left[(q_e - \bar{q})\bar{M}\right] + \frac{1}{A_{grid}} \int \dot{q}\, dA_c . \qquad (2.21)$$

The first term on the right can be interpreted as the convergence of the compensating downward flux of q in the environment, and the second and third as effects of entrainment (q_e) and detrainment (q_c). The fourth term is the same as the $\partial(\bar{\omega}\bar{q})/\partial p$ term on the left side except that $\bar{q}$ is replaced by $\bar{q} - q_e$. The ratio $(\bar{q} - q_e)/\bar{q}$ is equal to $\eta/(1-\eta)(q_c/\bar{q} - 1)$, where η is the fractional cloud area. For small η and not too large values of $q_c/\bar{q}$, this ratio is small, and we therefore ignore the fourth term in (2.21). At the same time q_e is replaced by $\bar{q}$ in the remaining terms and in the plume equations described earlier. (These approximations are also made by Ooyama, 1971, and Arakawa and Schubert, 1974. For $q = r_w$ or r, they are not so readily justifiable in our case; see Appendix C.) The resulting three terms define the quantities C_θ, C_r and C_w for $q = \theta$, r and r_w. At levels between cloud base (p_b) and the bottom (p_{bb}) the cumulus effect is also determined by these three terms, but with $\lambda \equiv 1$, η_u decreasing linearly from its value at p_b to zero at p_{bb}, and by replacing $q_e (= \bar{q})$ in the second term by $q_c(p_b)$. This may be thought of as a crude modeling of a tendency

for the more buoyant (larger θ , larger r) elements in the sub-cloud layer to be those which enter cloud base.

Finally, the environment $\dot{q}$ term in (2.21), in terms of the symbols used in table 1, now consists of the following effects

$$q = \theta : \qquad -\left[E_p + E_\ell + E_c\right] \quad \text{times} \quad (L/c_p)\bar{P}^{\kappa}$$

$$q = r : \qquad -A + E_p$$

$$q = r_v : \qquad E_p + E_\ell + E_c$$

where, as mentioned earlier, E_ℓ and E_c are obtained implicitly by saturation adjustment.

2.4 Water budget

Equations (2.6), (2.7) and (2.8) constitute the large-scale water budget. Only vapor and liquid forms are considered; liquid may exist as cloud droplets ($\lesssim 100\ \mu$ diameter, mixing ratio $r_\ell = r - r_v$) which do not move relative to the air parcels in which they exist, and as precipitation-size particles (mixing ratio r_p) which fall straight down. When r_v and r are predicted by the use of (2.6) and (2.7) (step 5, table 1), there is no guarantee that $r_{v_{n+1}}$ will not turn out $> r_{n+1}$. The negative values of $r_{\ell_{n+1}}$ so implied are few in number and are generally small.

Microphysical processes are parameterized, following the often-used procedures developed by Kessler (1969), on the implicit assumption that they can be applied directly to the large-scale variables (ignoring effects

of inhomogeneities). We thus assume raindrops to be size-distributed with diameter D according to the empirical Marshall-Palmer (1948) formula

$$N_0 dD = N_0 e^{-\lambda D} dD = (10^7 \text{ m}^{-4}) e^{-\lambda D} dD .$$

With N_0 fixed, λ is determined by the precipitation mixing ratio.

In (2.8), ω_p , the precipitation fall speed in terms of pressure, is set equal to a constant, .05 cb sec^{-1}. This allows use of the semi-implicit Marchuk procedure (see Phillips, 1973) which avoids having to use a smaller time step in (2.8) than in the other equations. A discussion of the error made in taking ω_p = constant, and of the application of the Marchuk scheme, is to be found in Appendix D.

The term A in equations (2.6) and (2.8) represents the sum of "autoconversion" and "collection:" $A = A_u + A_c$. Autoconversion is the parameterization of the processes by which cloud droplets become rain drops. We follow Kessler in assuming

$$A_u = a r_l .$$

a is a disposable parameter. A value for a of about 10^{-3} sec^{-1} is thought to apply for clouds which are not entirely composed of ice (conversation with Professor Houghton, 1972; Mason, 1969), and this value seems to be favored by modelers of cumulus clouds (for example, Simpson and Wiggert, 1969). The apparent persistence of the anvil rainfall in Zipzer's (1969) case study might, however, argue in favor of a smaller a , unless there is sufficient upward motion within the anvil to replenish the r_l which

is converted to precipitation. Therefore, a is an important parameter for our problem and is the subject of limited experimentation, reported in Chapter 5.

As raindrops fall through air containing cloud drops, some of the cloud drops will collide and coalesce with the raindrops. This process, which we call "collection," reduces r_ℓ and increases r_p. It is described by the "continuous collection" equation, derived by Kessler (1969, p. 28). With all symbols in the meter-ton-second system, it can be written

$$A_c = 933.5\, E\, \rho_s^{.375}\, \rho_o^{.5}\, r_\ell\, r_p^{.875} \tag{2.22}$$

ρ_s and ρ_o are "standard" densities based on Jordan's (1958) mean West Indies hurricane season sounding; ρ_o is at p_a = 100 cb and ρ_s is at the pressure at which (2.22) is to be applied. The collision efficiency, E, in this formula will be assumed unity. For small r_p, A_c tends to be less important than A_u, but the converse is true in the presence of sufficiently large r_p.

Precipitation evaporation per unit mass of air is given by

$$E_p = 134.5\, \rho_s^{-.325}\, \mathcal{E}(p)\, r_p^{.675}\, (r_s - r_v). \tag{2.23}$$

This equation was constructed using Beard and Pruppacher's (1971) UCLA Cloud Tunnel measurements of evaporation from ventilated water drops.

Tables 1 and 2 of their paper were first used to obtain (by eye) the evaporation rate from a single drop of mass m :

$$\frac{dm}{dt} = \mathcal{E}(p)\, D^{1.7} (r_s - r_v) . \qquad (2.24)$$

This equation was then integrated over all drop sizes in the Marshall-Palmer distribution to give (2.23). $\mathcal{E}(p)$ is listed in Appendix E.

Since the aim of this study is to explore the effect of precipitation evaporation, it is necessary that the evaporation calculation be as accurate as possible. Sources of error are the following:

(a) The formula (2.24) fits Beard and Pruppacher's measurements only to $\pm$ 15% for $60 \leq p \leq 100$ cb.

(b) The fractional rate of evaporation is greater for small drops than for large. Thus, one suspects that raindrop samples taken in situations where evaporation is occurring might correspond to an N_o substantially below $10^7 m^{-4}$. The factor 134.5 is proportional to $N_o^{.125}$. A value for N_o of $10^6 m^{-4}$ would then replace 134.5 by 0.47 (134.5). The author knows of no quantitative evidence to substantiate taking N_o as low as $10^6 m^{-4}$, nevertheless the uncertainties concerning the drop-size distribution must be considered as a source of uncertainty in E_p .

(c) The fall speed of precipitation, ω_p , is an overestimate in the mid- and upper troposphere (see Appendix D). Thus, a systematic but small underestimate of evaporation is likely above 80 centibars or so. The error is probably less than 25%, based on the error in ω_p estimates.

(d) Time and space truncation error in calculation of E_p and r_p was not explored as fully as it might have been. However, tests described in Appendices D and E suggest that this is no more serious than (a) or (c) above. The downward diffusion of r_p, evident (see figure D-2) in the 180 second timestep test of the Marchuk scheme, may tend to compensate for the $\sim$ 25% slowness in the phase speed, for example.

Defining the operator $\langle\ \rangle$ by

$$\langle(\ )\rangle = \frac{1}{g}\int_0^{p_\infty} (\ )\, dp$$

, we may write the vertical integrals of (2.6)-(2.8) as

$$\frac{\partial\langle r\rangle}{\partial t} = -\frac{\partial}{\partial x}\langle ur\rangle - \mathcal{R}\Big|_{p_\infty} - \langle A\rangle + \langle E_p\rangle + \langle C_r\rangle \quad (2.25)$$

$$\frac{\partial\langle r_v\rangle}{\partial t} = -\frac{\partial}{\partial x}\langle ur_v\rangle - \mathcal{R}\Big|_{p_\infty} + \langle E_l\rangle + \langle E_p\rangle + \langle E_c\rangle + \langle C_v\rangle \quad (2.26)$$

$$\frac{\partial\langle r_p\rangle}{\partial t} = -\frac{\omega_p r_p}{g}\Big|_{p_\infty} + \langle A\rangle - \langle E_p\rangle \quad (2.27)$$

The terms $-\mathcal{R}\Big|_{p_\infty}$ and $-\frac{\omega_p r_p}{g}\Big|_{p_\infty}$ are the moisture accession from the sea and the large-scale precipitation. $\langle C_r\rangle$ in (2.25) is convective

cloud precipitation, as can be verified by integrating (2.20), with $q_c = c$, from p_t to p_b and dividing by g. It is important that the finite difference analogues to these equations have no spurious sources or sinks. That this is the case can easily be demonstrated providing that no large-scale precipitation is present above 15 cb. In no computations did $c_p > 0$ ever occur above the 15-20 cb layer.

A list of free parameters which are identical in <u>all</u> production runs with the complete model is given in table 2.

It is believed that this model is capable of describing the essence of the large-scale evaporation process discussed in chapter 1. Additional details concerning computational procedures are provided in the Appendices.

Table 2. Parameters which are identical for all production runs

---

Computational

Horizontal grid increment: 25 km, $0 \leq \chi \leq$ 1000 km

Vertical grid increment: 5 cb, $10 \leq p \leq$ 100 cb;
10 cb, $0 \leq p \leq$ 10 cb

Time step used in boundary layer initialization (section 3.2.1): 1000 sec

Large-scale flow

f (Coriolis parameter): $.24 \times 10^{-4}$ sec^{-1}

u_g (Zonal geostrophic wind) at 97.5 cb: -5 m sec^{-1}

Subgrid-scale, non-convective diffusion (section 2.2)

Depth of constant stress layer: 75 m

C_D (drag coefficient at 75 m): 10^{-3}

Top of planetary boundary layer ($\sigma \rightarrow 0$): 85 cb

Sea surface temperature (used to obtain r_{sea}): 28 C

Cumulus convection (section 2.3)

Entrainment rate: $.2 \times 10^{-3}$ m^{-1}

h_m [equation (2.18), ratio of number of mature clouds to growing clouds]: .33

Large-scale cloud microphysics (section 2.4)

ω_p (precipitation fall speed): .05 cb sec^{-1}

N_0 (parameter in Marshall-Palmer drop size distribution): 10^7 m^{-4}

E [collision efficiency, eq (2.22)]: 1.0

---

3. ADVENTURES IN INITIALIZATION

At the start of each integration it is assumed that there is present a large-scale disturbance having the structure of a simple tropical wave. In this chapter we will review the procedures used in the construction of this initial disturbance, with particular attention to problems encountered in the initialization of the divergent portion of the flow.

3.1 Temperature, relative humidity, and geostrophic wind

The temperature and relative humidity inputs are based on Palmyra Island's LIE (Line Islands Experiment) mean (see figure 3-1). All computations have the identical initial vertical temperature sounding (solid curve on figure 3-1a) and a geostrophic easterly current of -5 m sec^{-1} at 97.5 cb. No initial x-variation of temperature is present; we choose $\partial\theta/\partial y$ to be either negative (westerly geostrophic wind shear), or zero (no shear). Superimposed upon this is a meridional current of amplitude ± 5 m sec^{-1}, varying sinusoidally in x, but independent of height (except for frictional modification). The initial relative humidity varies only with pressure in the westerly shear cases, but a sinusoidal x-variation with the high humidity lying along the trough axis is superposed when the shear is zero (see figure 3-1b). The picture that emerges from this is a simple tropical wave, with a wave length of 1000 km, only slightly shorter than typical.

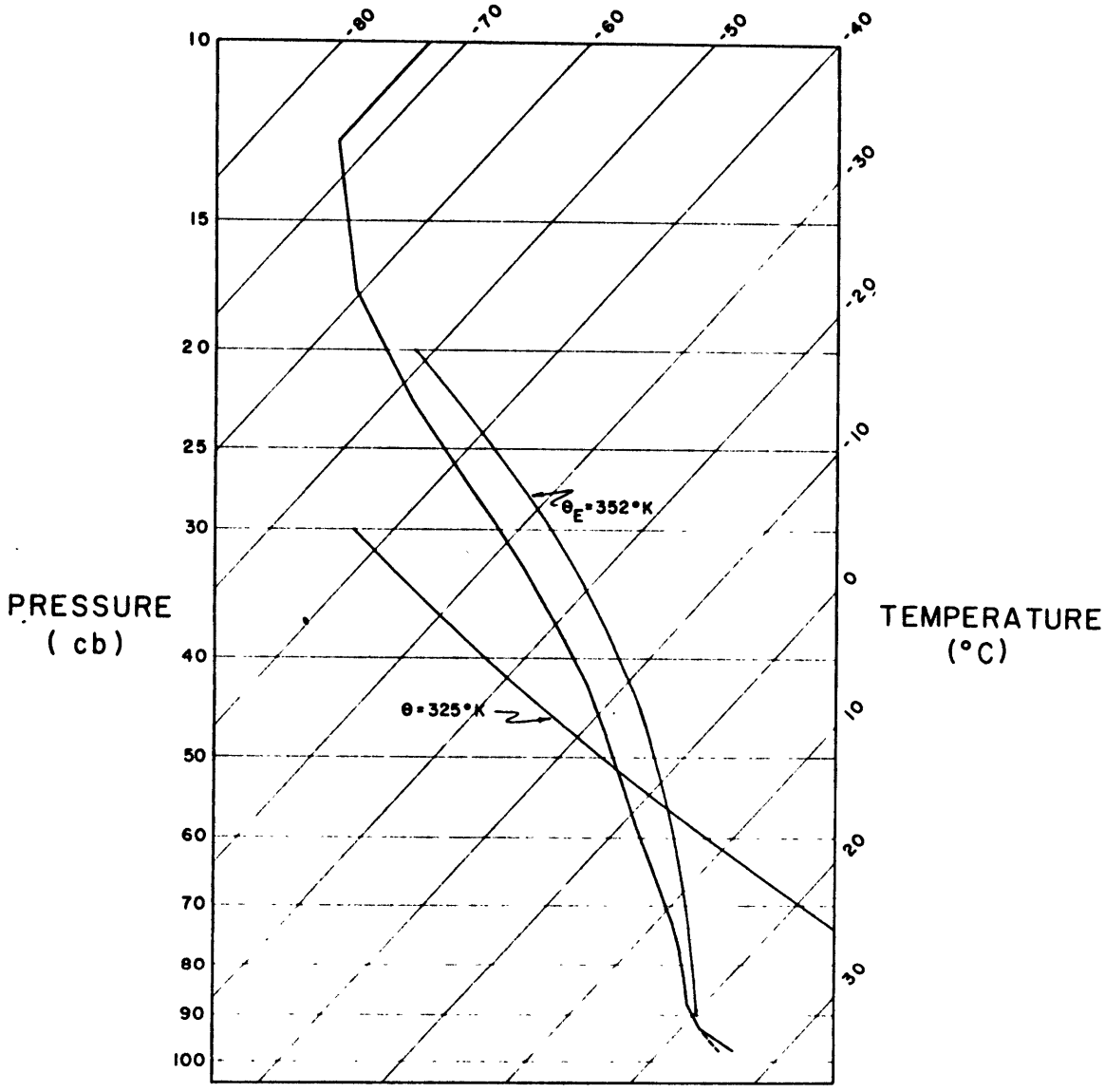


Figure 3-1a. Initial temperature sounding (plotted on a skew - T log p diagram) used in production runs. This coincides with the LIE Palmyra 0000Z mean, except below 92.5 cb, where the Palmyra means is dashed.

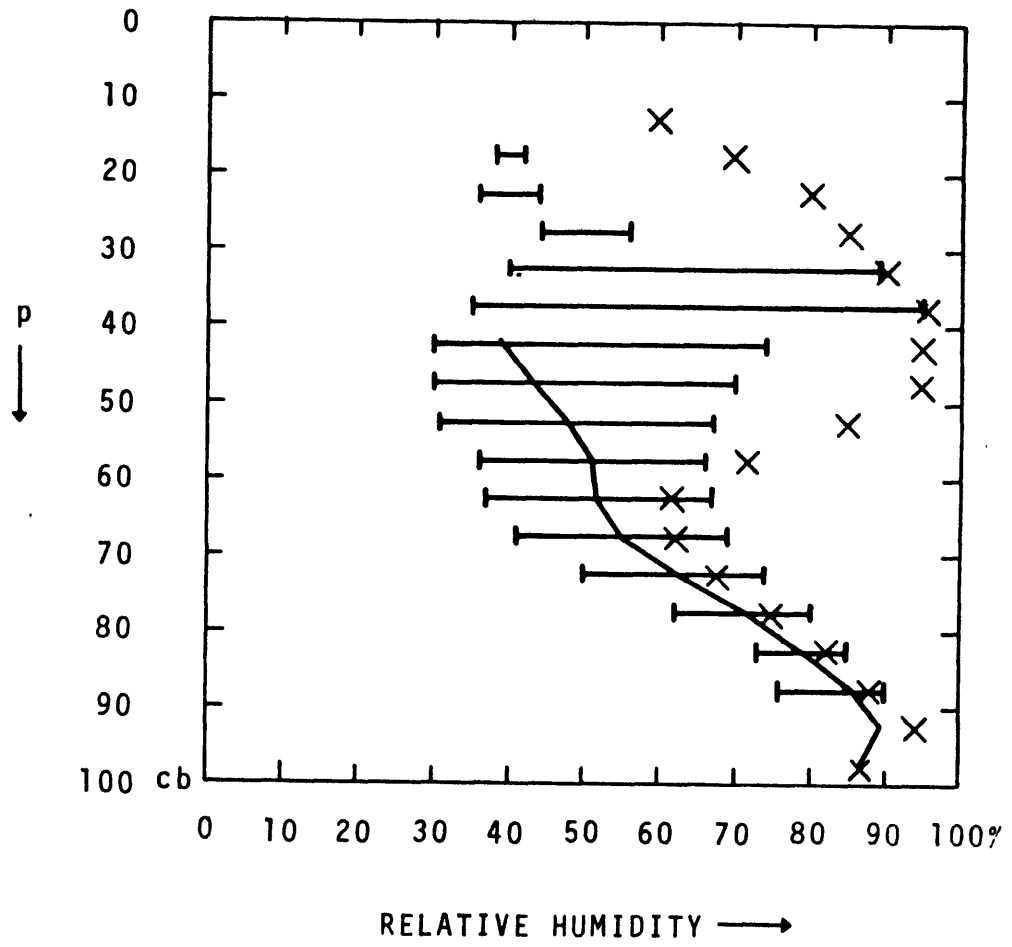


Figure 3-1b. Initial humidity soundings used in production runs. Solid line is LIE Palmyra 1200Z mean. The range over which relative humidity varies at each pressure level in the no-shear runs is indicated by the ⊢—⊣ at each level. At 12.5 cb, relative humidity is initially 40% in these runs. Initial relative humidity (constant in χ) in the runs having shear is indicated by a X at each level. At 92.5 and 97.5 cb, shear and no-shear humidities are equal.

3.2 Calculation of divergent horizontal flow

Experience with the hydrostatic primitive equations has amply demonstrated that careless initialization of the divergent component of the flow leads to development of spurious internal gravity waves of sufficient amplitude to obscure the meteorologically significant motions. In the case of a linear system for which both a "meteorological" wave (with phase speed $\approx u$, the speed of the basic zonal current) and a pair of gravity-inertia waves are solutions, Phillips (1962) showed that initializing with divergence implied by the quasi-geostrophic approximation resulted in virtually no gravity wave development. Considering the previous section's specifications of the geostrophic flow, we may define a length scale of 250 km and a horizontal velocity scale of 5 m sec^{-1}. With $f = .24 \times 10^{-4}$ sec^{-1}, the Rossby number for our problem is $5/[(.25 \times 10^{6})(.24 \times 10^{-4})] \approx 0.8$. Such a large value suggests that nonlinear effects will be important and indicates that initializing with the "quasi-geostrophic divergence" will not be as dramatically successful as in Phillips' linear case. In addition, two circumstances peculiar to our model preclude a straightforward use of this procedure: (a) The necessity of making special allowance for surface friction because of the crucial relation $M_c(p_s) = -\beta\omega(p_s)/g$ (section 2.3.1), and (b) the desirability of including the influence of cumulus-induced heating in the quasi-geostrophic divergence.

The quasi-geostrophic ω-equation appropriate to our domain and the special temperature and geostrophic wind inputs discussed in section 3.1, and including heating, is

$$\sigma(p)\frac{\partial^2\omega}{\partial x^2} + f^2\frac{\partial^2\omega}{\partial p^2} = 2f\frac{dV_g}{dp}\frac{\partial^2 v_g}{\partial x^2} - \frac{RP^x}{p}\frac{\partial^2\dot{\theta}}{\partial x^2} \quad (3.1)$$

The (horizontally uniform) static stability function, $\sigma(p)$ equals $(R^2T^2/p^2g^2)N^2$, where N^2 is the square of the Brunt-Väiäsäla frequency computed from Jordan's (1958) mean West-Indies hurricane-season sounding. Since there are 40 grid points, the complete solution to this equation may be expressed as

$$\omega = \sum_{i=1}^{20}\left[A_i \cos k_i x + B_i \sin k_i x\right], \quad k_i = 2\pi/L_i$$
$$L_i[m] = 10^6/i \quad (3.2)$$

Substituting this solution into (3.1) yields 40 equations for the unknown functions of p, A_i and B_i, $i = 1, 20$. Because of the special nature of the initial geostrophic flow, the first (baroclinic forcing) term on the RHS of (3.1) only appears in the equation for B_1. Since $\dot{\theta}$ is a nonlinear function of ω at 90 cb, convective heating has appreciable amplitude in wave number 2, but higher wave number components of the heating are ignored. Thus, the initial ω-field contains only wave numbers one and two. Solution for the corresponding Fourier coefficients, A_i and B_i, $i = 1, 2$, is by a standard relaxation technique.

3.2.1 Incorporation of surface friction

The starting point for the incorporation of surface friction is a "generalized" non-stratified Ekman solution for the boundary layer obtained

by solving the boundary layer equations

$$\frac{\partial}{\partial t}(u-u_g) = f(v-v_g) - g\frac{\partial}{\partial p}\left[-\rho^2 g \nu(p)\frac{\partial u}{\partial p}\right]$$
$$\frac{\partial}{\partial t}(v-v_g) = -f(u-u_g) - g\frac{\partial}{\partial p}\left[-\rho^2 g \nu(p)\frac{\partial v}{\partial p}\right]. \qquad (3.3)$$

The vertical discretization, finite-difference procedure and formula for the vertical variation of ν used in solving these equations are exactly those described in chapter 2. Starting from $u = u_g$ and $v = v_g$, the time-integration continues until $u-u_g$ and $v-v_g$ approach steady-state. The solutions for $u-u_g$ and $v-v_g$ each consist of two parts, the x-average, and its deviation, proportional to $\sin kx$. From this solution the initial v-field is determined as follows. First, the Ekman $v-v_g$ is added to v_g at each grid point to obtain a preliminary v. In order to satisfy the constraint that the domain average of v be zero, the domain average of this preliminary v is subtracted from each grid-point value to get the initial v-field.

Having obtained the frictional structure of u in the lowest levels, it is necessary to modify the u aloft so as to satisfy mass continuity, i.e., the divergence in the "Ekman" layer must be counterbalanced by convergence somewhere aloft. Three strategies for doing this were tested by making several integrations with a "dry" version of the model (i.e., equations (2.1)-(2.5), with $\dot{\theta} = 0$. These tests are summarized in table 3. In all these runs, values of the dependent variables were printed out at each time step for 2 preselected grid points, one in the lower troposphere and the other in mid- or upper troposphere. This greatly facilitated diagnosis

Table 3. Summary of input constants and friction-initialization strategy used in "dry-run" initialization tests

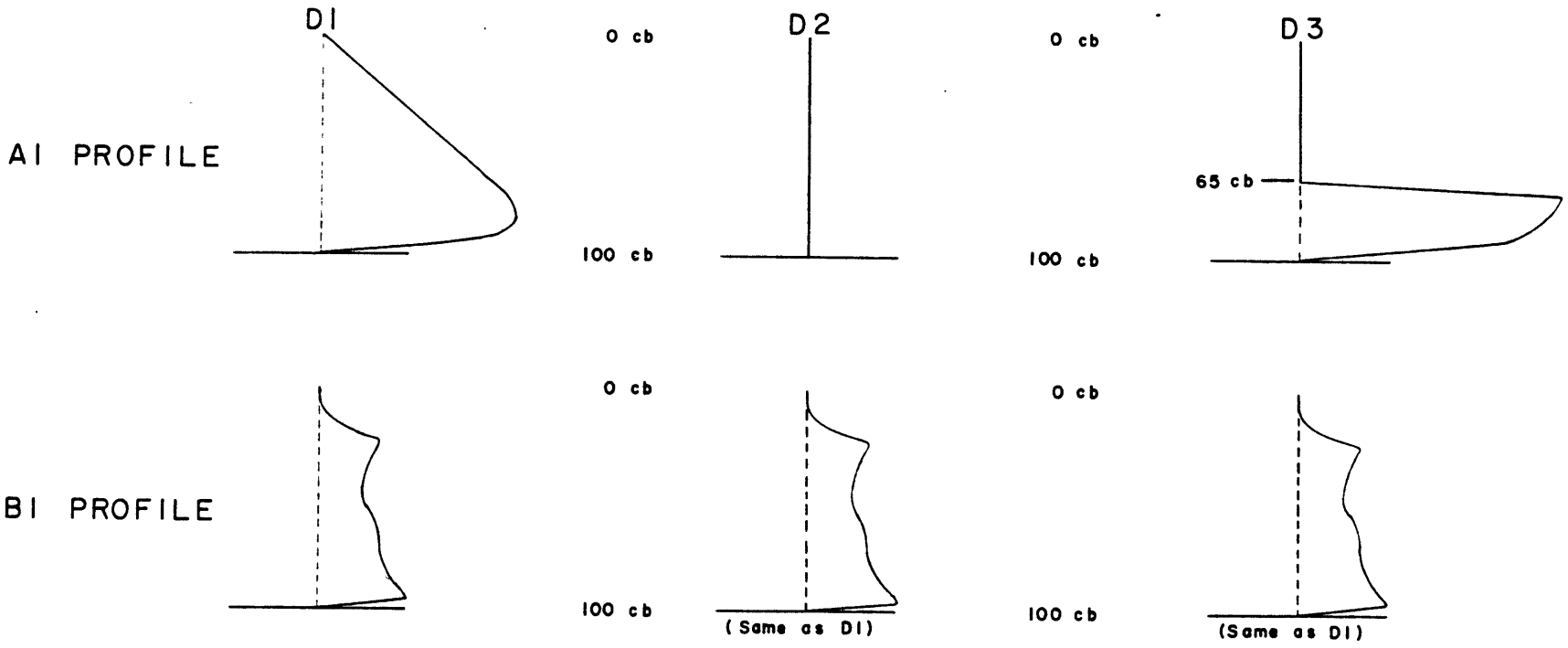
Run	Duration [hr]	Frequency of output [hr]	$\frac{\partial \theta}{\partial \psi}$ [°K/m]	Top of boundary layer [cb]	T [°K] of 97.5 cb	C_D	Initialization strategy number
D1	12	2	-10^{-6}	70	298.2	10^{-3}	1; return flow uniform $0 \leq p \leq 100$ cb.
D2	10	2	-10^{-6}	70	298.2	0 $\longrightarrow$	frictionless run
D3	12	2	-10^{-6}	70	298.2	10^{-3}	1; return flow occurs in 65-70 cb layer.
D4	12	2	$-.5 \times 10^{-6}$	70	298.2	10^{-3}	2
D5	10	2	$-.5 \times 10^{-6}$	85	299.06	10^{-3}	3
D6	39.1	6	0	85	299.06	10^{-3}	3

of the two-or six-hourly contoured printouts of the dependent variables. Figure 3-2 summarizes the results of each test.

In strategy 1, the frictional ω , derived from continuity, consists of 2 parts: (a) that due to horizontal boundary layer convergence implied by the Ekman solution for u , and (b) a "return flow" of arbitrary vertical structure, but of a magnitude such that the vertically integrated mass convergence as implied by (a) and (b) together is zero. The top of the boundary layer (as defined by the vanishing of ν) is at 70 cb in both strategy 1 experiments. The initial vertical temperature sounding is the non-altered LIE Palmyra 0000Z mean depicted in figure 3-1 as the solid curve above 92.5 cb and the dashed curve below. The boundary layer is therefore stratified, with a θ - increase from 97.5 to 92.5 cb of 0.87 K.

During the first experiment (D1) using strategy 1, a standing internal gravity-inertia wave rapidly developed and destroyed the boundary layer (figure 3.2). This discouraging result was followed by experiment D2 which showed conclusively that with no friction or heating the flow remained quasi-geostrophic in spite of our large Rossby number. The other test (D3) of strategy 1, with a different return flow structure (figure 3-2), had results similar to D1. The reason for the failure of strategy 1 is indicated by a straightforward analysis of the homogeneous form of (3.1). By assuming that $\sigma \propto 1/p^2$ it is possible to obtain solutions of the form $\omega = A\,(p/p_0)^b \cos(2\pi x/L)$, satisfying boundary conditions of $\omega = A\cos(2\pi x/L)$ at $p = p_0$, and $\omega = 0$ at $p = 0$. Here, L is a horizontal wave length and

Figure 3-2. Major results of dry run tests. The two rows of graphs present the initial ω-pattern: initially $\omega = A_1 \cos \ell_1 x + B_1 \sin \ell_1 x$. Frictional contributions to ω are all included in A_1, baroclinic in B_1.

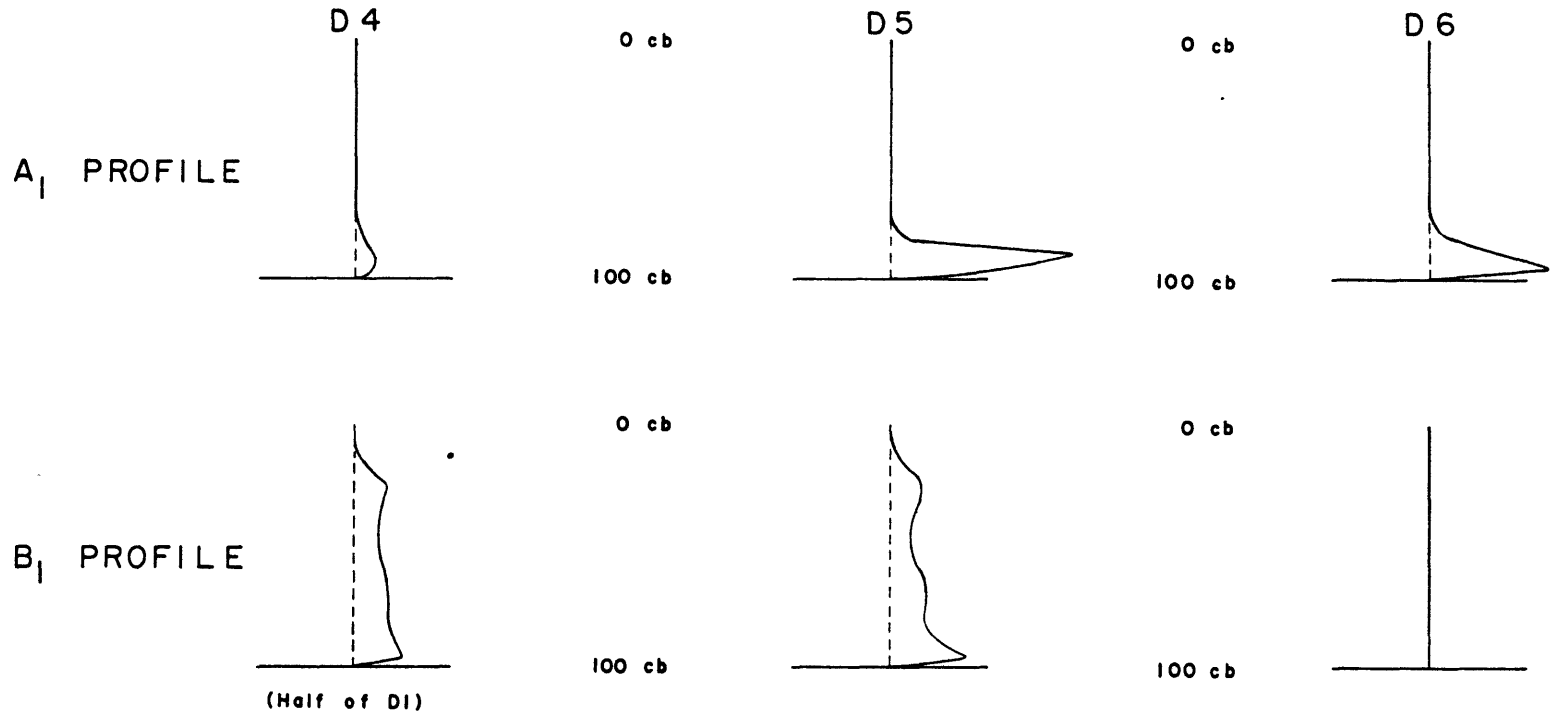


Standing gravity wave, period 5-6 hours, in 15-90 cb layer. Largest amplitude of about $.5 \times 10^{-4}$ cb sec^{-1} at 50-60 cb. Max $|\omega(90cb)|$ decreases to 40% of initial value by 4 hours.

Flow remains quasi-geostrophic throughout run -- no gravity wave. Max $|\omega(90cb)|$ changes little during run.

Separate standing gravity waves within the 90-70 cb, 70-60 cb, and 60-20 cb layers dominate the ω-pattern. Max $|\omega(90cb)|$ drops from $.6 \times 10^{-4}$ initially to $.2 \times 10^{-4}$ by 4 hours.

Figure 3-2. (Continued)



No gravity waves present -- flow remains quasi-geostrophic above 90 cb. Max $|\omega(90\,cb)|$ remains nearly constant at about $.15 \times 10^{-4}$ cb sec^{-1}.

ω at and below 90 cb decays to 50% of its initial max magnitude of $.5 \times 10^{-4}$ cb sec^{-1} by 6 hours and to $\sim$ 25% by 10 hours. No gravity wave activity.

ω at 90 cb decays to 50% of initial magnitude by 6 hours and to 10-15% after 24 hours. No gravity wave.

$$\beta = \text{constant} \approx \frac{\frac{f}{\frac{2\pi}{L}(N^2)^{1/2}}}{\frac{RT}{g}}$$

This corresponds to a "scale height" for the quasi-geostrophic ω of $f/[(2\pi/L)(N^2)^{1/2}]$, which, for $L = 10^3$ km, is roughly 450 m in the boundary layer of our model. This depth is the depth of a layer for which the Rossby radius of deformation is 1000 km, and is appreciably less than the neutral Ekman layer depth of $(2\nu/f)^{1/2} \approx$ 700 m. This violates the assumption in (3.3) that the Ekman depth is the smallest vertical scale height. This circumstance suggested to us that the failure of strategy 1 is because the boundary layer stratification is ignored; i.e., the ω produced by strategy 1 is too large in magnitude. From this we also concluded that the boundary layer return flow would tend to occur in a thin layer just above where ω reaches its peak magnitude. Some theoretical support to these conclusions is given by the more recently published study of linearized, stratified, quasi-steady boundary layers by Kuo (1973).

Strategy 2 is an attempt to incorporate the effects of stratification. The Ekman solution for u is ignored, but the solution for v is used in computing F_y according to formulae in Chapter 2. With the term $-f\,\partial/\partial p(\partial F_y/\partial x)$ added to the RHS, we solve (3.1) over the entire domain to obtain both the A_1 (friction) and B_1 (baroclinic) components of ω. The initial frictional ω turns out to be only about 15% of its neutral value; i.e., with a maximum magnitude of about 0.065×10^{-4} cb sec^{-1} ($\approx$ 0.06 cm sec^{-1}) at 90 cb, and is negligible above

85 cb. The only test of strategy 2 is with experiment D4, which showed no internal gravity-wave activity. We interpret this as indicating that this small ω is at least approximately correct for our postulated distribution of ν. The search for a usable initialization might have ended at this point had it not been that we felt somewhat bound by the then accepted practice of assuming $\beta = 1$ (i.e., $m_c = \bar{m}$). Since we desired to start our time integrations of the complete model with fairly vigorous convection, a maximum frictional vertical velocity of $\sim$ 0.1 cm sec^{-1} did not seem promising.

Strategy 3 is a compromise designed to preserve the larger neutral Ekman vertical velocities of strategy 1, but to suppress gravity-wave development. The top of the boundary layer is reduced to 85 cb, and θ at 97.5 cb increased to that at 92.5 cb (solid sounding curve on figure 3-1). The Ekman u is used at 97.5 and 92.5 cb only; the resulting ω at 90 cb serves as the lower boundary condition to the homogeneous equation for the A_1 appearing in equation (3.2). The baroclinically-forced ω is computed exactly as in other cases. Our rationale was that by steepening the lapse rate and making the boundary layer shallower, any gravity-inertia wave would have a long period. This, hopefully, would allow the cumulus convective heating to establish an amplifying, thermally direct, secondary circulation and so nullify the destructive effects of the gravity-inertia wave. Indeed, gravity-wave activity is absent in runs D5 and D6 and ω at 90 cb decays with time less rapidly than in runs D1 and D3. We thus decided to make do with strategy 3. However, we shall have more to say in chapter 4 regarding the performance of strategy 3 when heating is included.

3.2.2 Incorporation of cumulus-convection heating and computation of final u

The initialization of heating by cumulus convection and the computation of the corresponding ω require special care. The adiabatic portion of ω (baroclinic and frictional) is computed first, and an iteration procedure is then used to obtain wave number 1 and 2 components of the heating-induced ω, as follows:

(a) At each grid point, compute heating due to cumulus convection implied by the 90 cb adiabatic ω.

(b) Consider only wave numbers 1 and 2 of this heating.

(c) Solve (3.1) using the heating from step (b) as the only forcing function.

(d) At each grid point on the 90 cb level, add ω from step (c) to the adiabatic ω.

(e) Compute the resulting cumulus-convection heating and return to step (b).

At first we attempted to get by with only one pass through steps (a)-(d). The first ω-field is sufficiently inaccurate that an internal gravity wave develops when a full forecast is then made. No such problems occur when we allow the iteration process to continue until ω at successive iterations differs by less than 1%. This takes 8 iterations for $\beta = 1.0$ and 19 iterations for $\beta = 1.5$. These iteration counts are obtained using the temperature and humidity sounding corresponding to the complete model runs without shear, indicated on figure 3-1. A hand calculation suggests that convergence will not occur for this sounding if β is greater than about 1.7.

The initial u is determined as follows. Since $u_g = u_g(p)$, (2.4) may be written $\partial(u-u_g)/\partial x + \partial\omega/\partial p = 0$. We solve the finite difference form of this equation for $u-u_g$, subject to the constraint that the x-average of $u-u_g$ equals that obtained from the solution of (3.3). Finally, $u = u_g + (u-u_g)$.

None of the activities and conclusions reported on in this chapter should be regarded as universally applicable or exceptionally profound, but it is hoped that the reader who is constructing a numerical model will profit by the description presented here.

4. NUMERICAL MODEL RESULTS: CASES WITHOUT VERTICAL SHEAR OF THE ZONAL GEOSTROPHIC WIND

In this and the next chapter we discuss the numerical computations with the complete moist model. These fall naturally into two groups, depending upon whether or not vertical shear of the zonal geostrophic wind is present. Precipitating debris formed in an environment with shear can be carried away from its parent convective cloud and over cloud-free air. The runs having shear therefore provide the best test of our working hypothesis stated in chapter 1. These are discussed in chapter 5. However, experiments without the additional asymetries produced by shear prove relevant to the study of CISK and reveal some of the strengths and shortcomings of the model.

At each timestep all dependent variables have been printed out for two preselected gridpoints. In addition, an array showing which grid squares contain convective cloud and which do not, and another depicting where large-scale cloud water is located are available for each time step. This information is very helpful in determining the time evolution of the model disturbance.

The initial meridional wind (v, figure 4-1) and temperature fields are identical for all no-shear runs. The temperature sounding (constant in x) is depicted in figure 3-1a. The autoconversion coefficient, a, equals $.5556 \times 10^{-3}$ sec^{-1}, i.e., 1/30 minutes, in all no-shear computations. Table 4 summarizes the distinguishing features of each no-shear run. (For the assigned value of all parameters which are identical in all runs with the complete model the reader is referred to table. 2, chapter 2). The runs

Table 4. Free parameter values in no-shear runs

Run number	Timestep, Δt [sec]	Duration of run [hour]	Output interval [hour]	Ratio of upward mass flux through cloud base to large-scale mass flux at 90 cb, β	Autoconversion coefficient, a [sec^{-1}]	Maximum convective-cloud water mixing ratio, r_{ccm}
N0	180	18	2	1.0	$.5556 \times 10^{-3}$	.002
N1	180	12	3	1.0	$.5556 \times 10^{-3}$	.003
N2	180	18	6	1.0	$.5556 \times 10^{-3}$	.003
	(Differs from N1 in that during initialization friction included directly in ω-equation -- see section 3.2.1, "strategy 2")					
N3	180	6.95	3[1]	1.5	$.5556 \times 10^{-3}$	.003
N4	90	6	6	1.0	$.5556 \times 10^{-3}$	.003

[1]Output failed to appear at 6 hours.

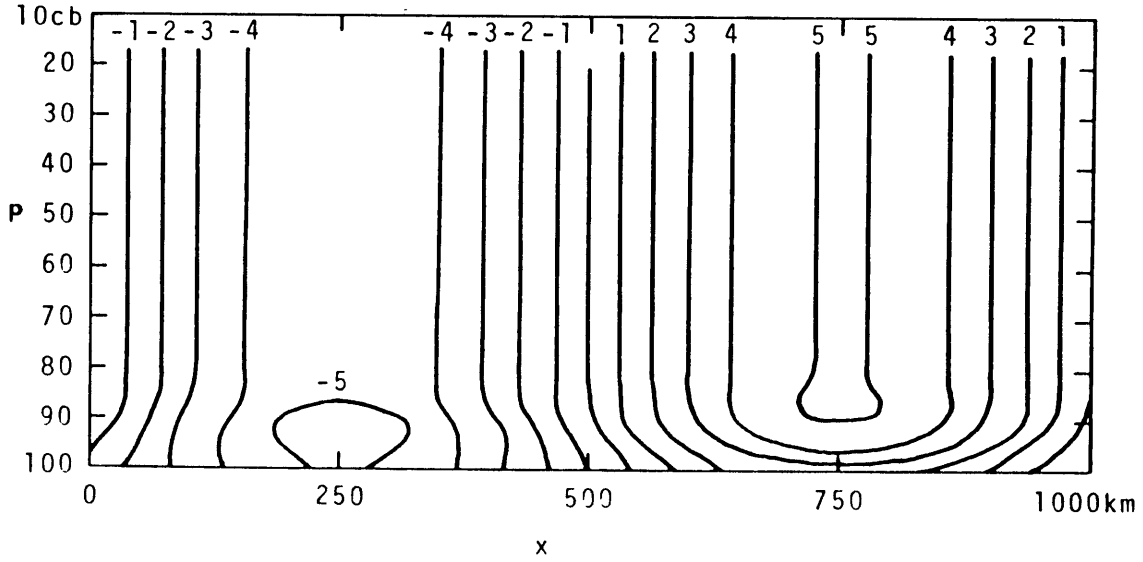


Figure 4-1. ν at 0 hours for all no-shear runs. Isotachs labeled in m sec^{-1}.

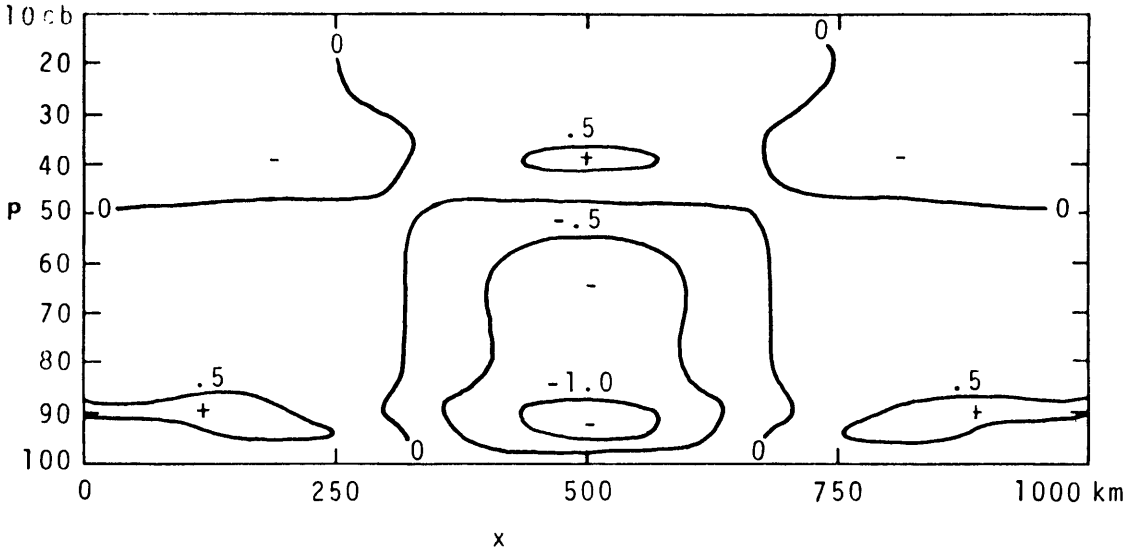


Figure 4-2. ω at 0 hours, run N1. Isolines are labeled in 10^{-4} cb sec^{-1} (approximately 0.5 cm sec^{-1} at 80 cb).

of primary interest are N1, N2 and N3. The initial relative humidity distribution for all no-shear experiments subsequent to N0 is based on the relative humidity of that run at t = 8 hours. The initial relative humidity for the N0 run had as its x-average at each level the LIE mean with an x-variation superposed such that the high humidity lay along the trough line (see figure 3-1b). Run N0's results featured a drastic weakening of the initial disturbance and negligible precipitation from a very meager large-scale cloud. In order to guarantee development of a more substantial large-scale cloud we decided to increase the initial humidity and to increase the maximum liquid water content in convective clouds, r_{lcm}, to .003 in all subsequent no-shear experiments. By choosing the predicted humidity of run N0 as the basis for the augmented initial humidity (also shown on figure 3-1b), we are anticipating the development of a large-scale cloud in a manner consistent with the behavior of our numerical model.

Run N4 is identical to N1 except that Δt = 90 seconds. The 180 second timestep used in experiments N0, N1, N2 and N3 is very close to the maximum allowable according to the linear computational stability criterion for this model. Run N4 was made as a precautionary check; at six hours the results of the two runs are almost indistinguishable.

4.1 N1 and N2: The basic no-shear experiments

We shall now consider the evolution of run N1 in detail. Figure 4-2 shows the initial ω-field, which is composed of friction and convection heating components. The frictional component is identical to the initial ω of experiment D6 (see figure 3-2). Figure 4-3 presents a comparison of the relative magnitudes of the friction and heating components at

selected levels. The ω due to friction is comparable to the heating ω at 90 cb and below. Wave number two of the heating produces a substantial ω ; in fact, at 97.5 cb wave number two of the heating ω has larger amplitude than wave number one. This is due to the near-zero static stability below 90 cb and to the circumstance that the "geostrophic scale height" (section 3.2.1) corresponding to wave number two is half that of wave number one.

Convective cloud is assumed to be present at all x for which ω at 90 cb is negative (section 2.3.1); this region, centered at x = 500 km, is 400 km (16 Δx wide. Initially, maximum cloud top in each column having convective clouds is within the 35-40 cb computational layer, and the largest detrainment occurs between about 35 and 50 cb. (Unfortunately, p_t , p_i and p_b appearing in (2.17) were not saved for any of the runs so it is not possible to reconstruct exactly the $h(p)$ profile. We believe that for the duration of most runs, 5 cb $< p_i - p_t <$ 10 cb.) The consequent evaporation of convective cloud water into the unsaturated environment results in cooling which accounts for the subsidence centered at 40 cb in the trough.

Figures 4-4 a-d, ω at three, six, nine and twelve hours, figures 4-5 a-d, the domain water budget for four consecutive three-hour periods, and table 5 reveal several of the important aspects of experiment N1. The water budget is computed using equations obtained by integrating (2.25)-(2.27) with respect to x over the length of the domain and with respect to time over the appropriate three-hour period. The five boxes symbolize various categories of water substance. The arrows indicate the <u>net</u> flow of water substance between these and to and from the sea. There is no storage

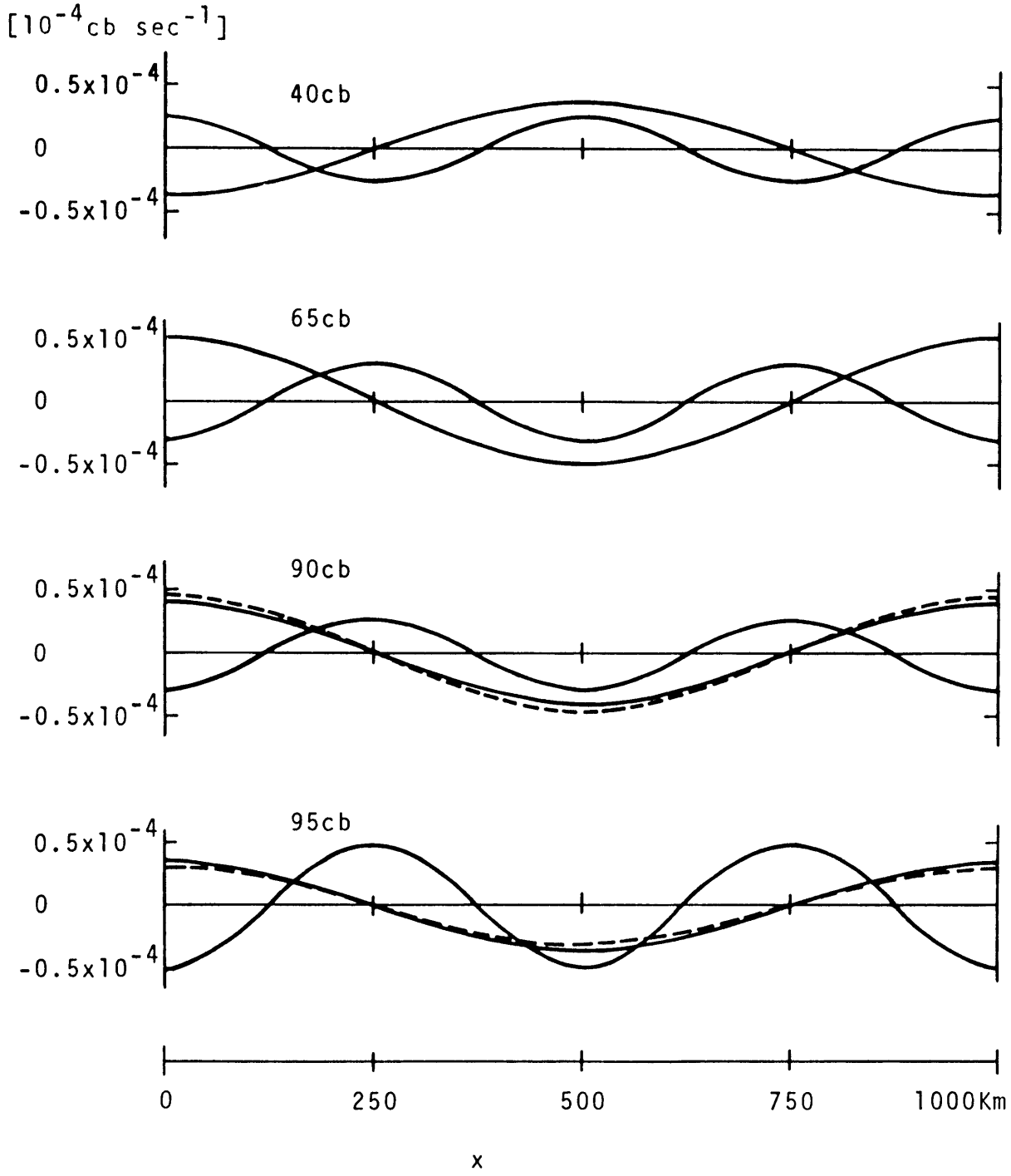
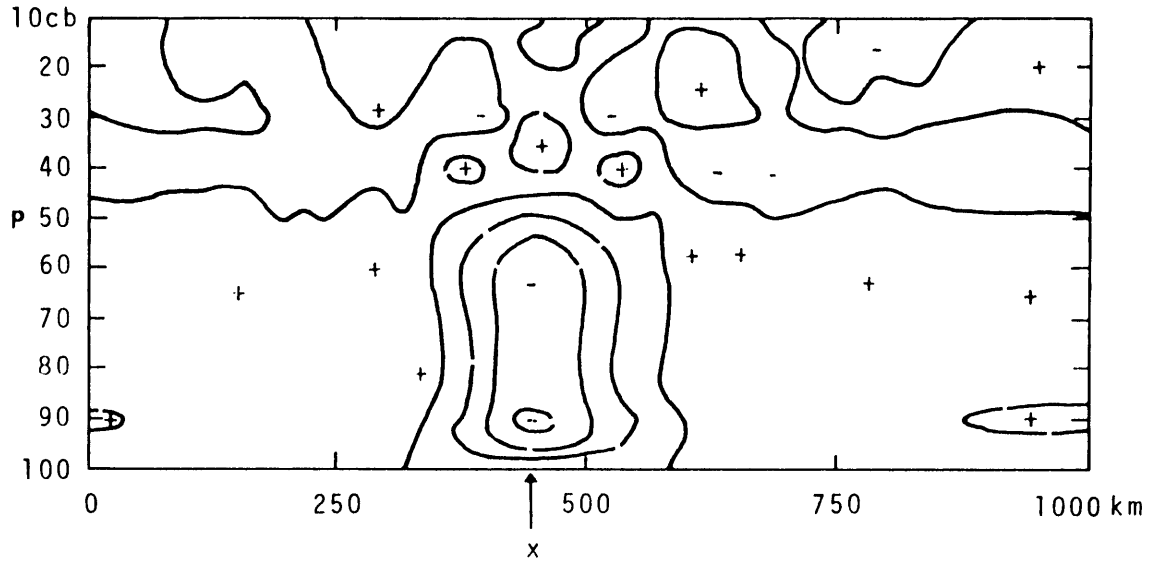
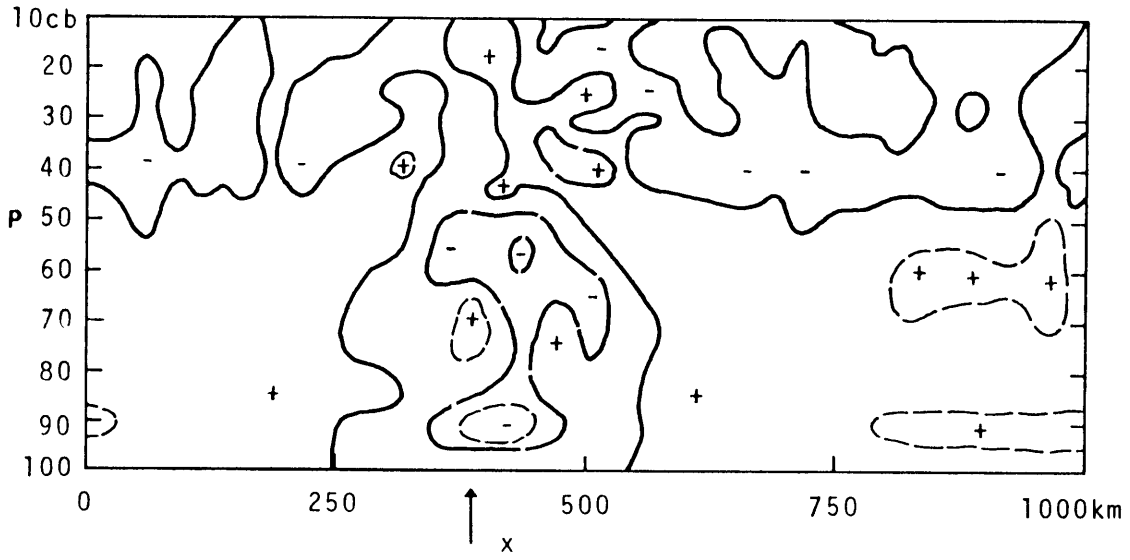


Figure 4-3. The partitioning of the initial ω, experiment N1, into frictional and heating components at selected levels. Solid curves are the wave number 1 and 2 portions of the ω forced by convection heating. Dashed curves at the two lower levels indicate the frictionally forced ω, which is negligible at the two higher levels.

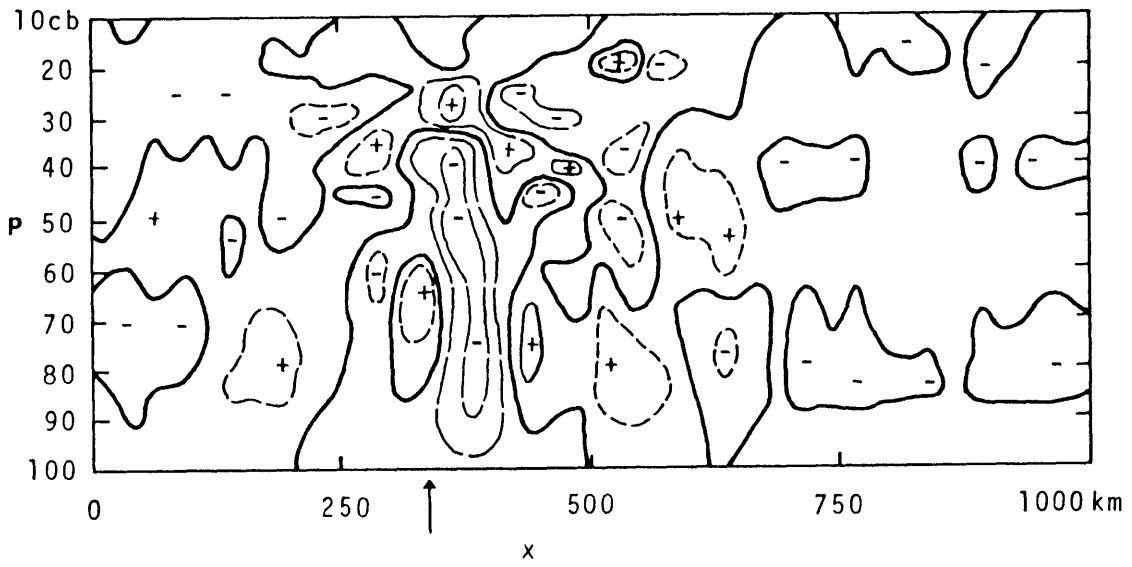


a. 3 hours

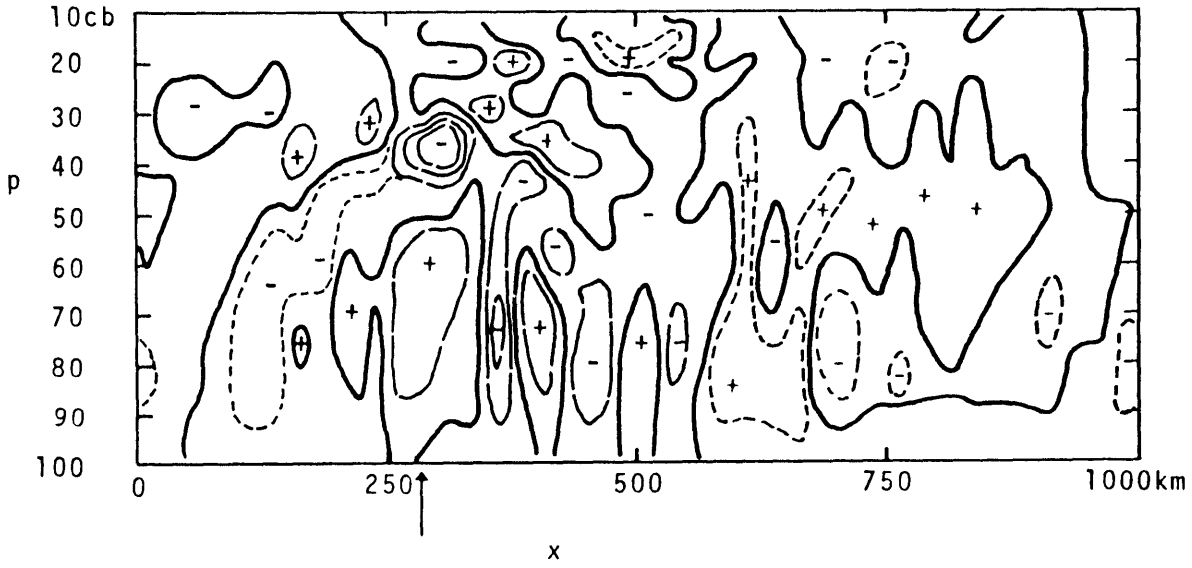


b. 6 hours

Figure 4-4. ω at three-hour intervals, experiment N1. Solid lines are the 0 isopleths. Long-dash lines are every 0.5×10^{-4} cb sec^{-1}; short-dash lines are intermediate (0.25, 0.75, etc.) isopleths. Pluses and minuses indicate local maxima and minima. The heavy, vertically pointing arrow below each diagram marks the trough-axis position based on a constant westward movement of 5 m sec^{-1} from χ = 500 km initially.

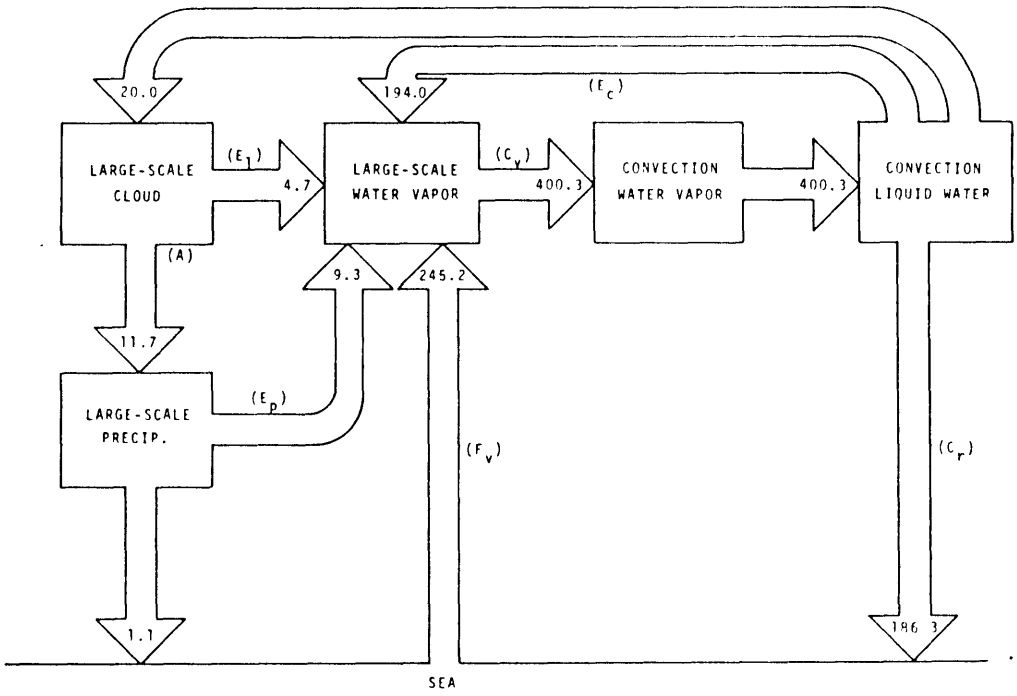


c. 9 hours



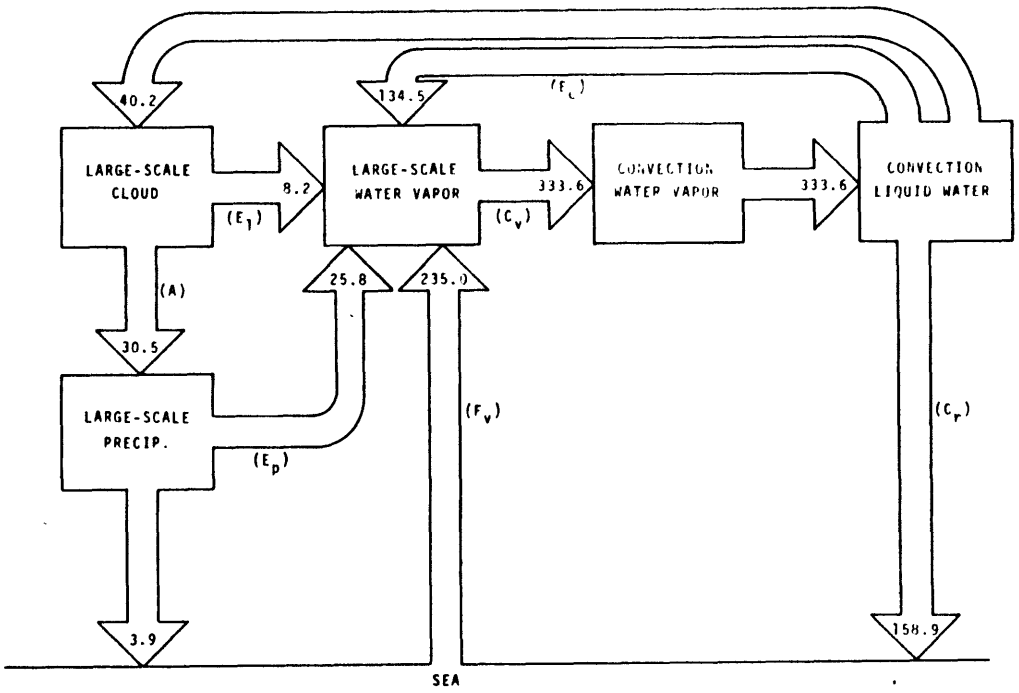
d. 12 hours

Figure 4-4. (Continued)

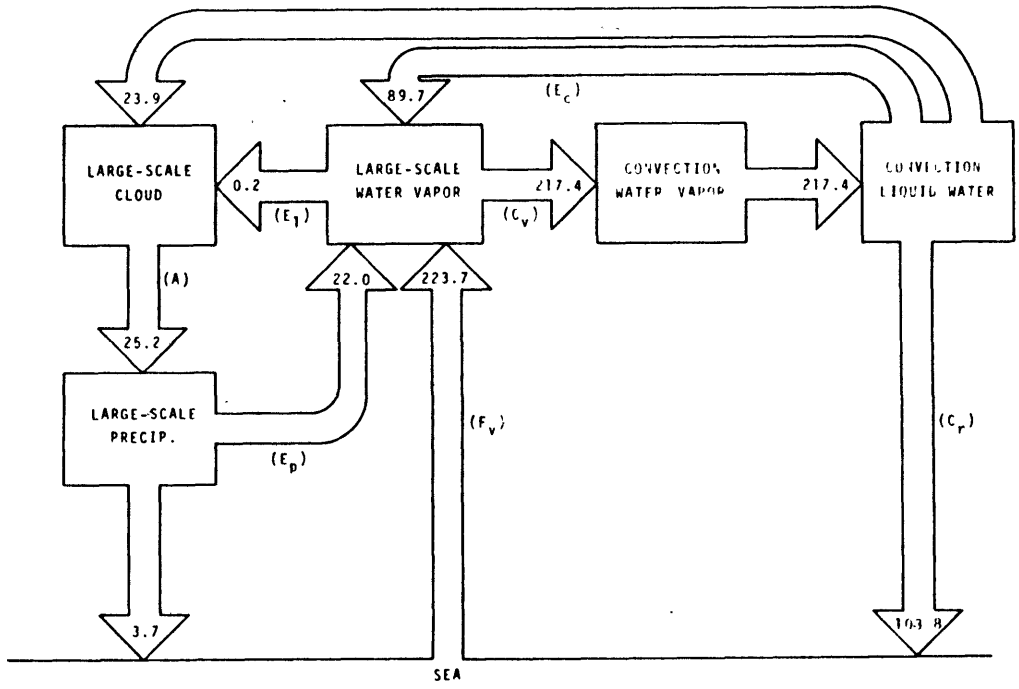


a. 0-3 hours

Figure 4-5. Domain water budget for run N1, by three-hour periods. Direction of flow is indicated by arrows; number in head of arrow indicates the net flow of water substance, in ton m^{-1}. Some of the arrows symbolize the χ -integrals of terms appearing in (2.25)-(2.27); these are so indicated by the symbols in parentheses.

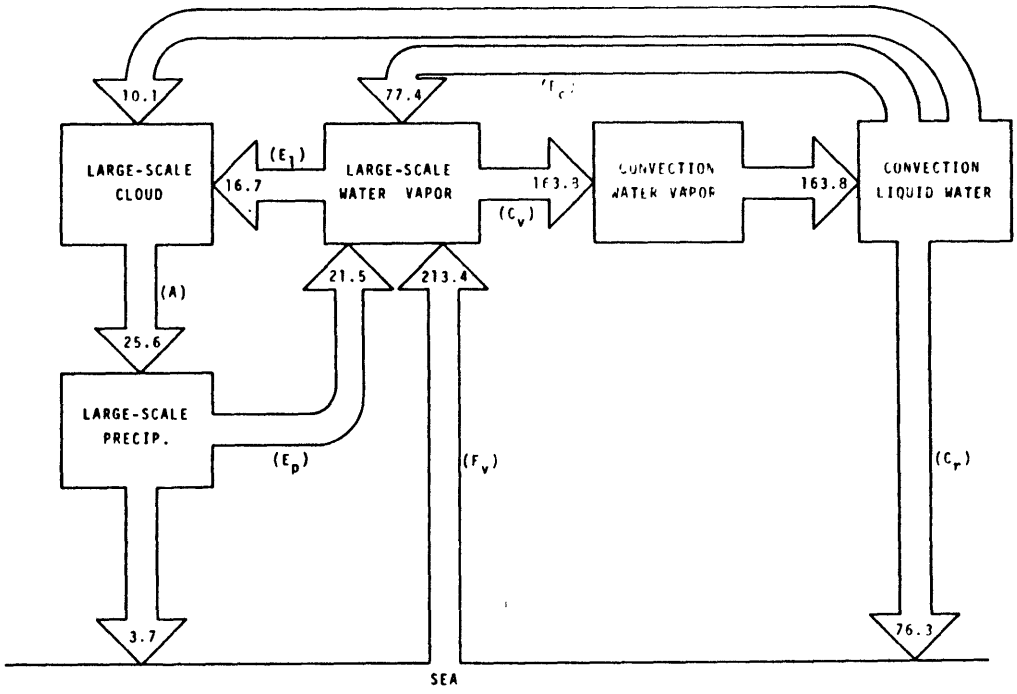


b. 3-6 hours



c. 6-9 hours

Figure 4-5. (Continued)



d. 9-12 hours

Figure 4-5. (Continued)

Table 5. Supporting and supplementary data for figures 4-4 and 4-17. The ω-values (all in units of 10^{-4} cb sec^{-1}) are extrema corresponding to important features on these figures. Liquid water mixing ratio, r_ℓ, is the maximum observed (in units of 10^{-3}) at the indicated time (hours). Maximum surface rainfall (mm) is over the preceding three hours

	0	3	6	9	12 hours
(1) Ascent below large-scale cloud	-1.17 500 km 95 cb	-1.57 437.5 km 90 cb	-1.06 437.5 km 55 cb	-1.63 362.5 km 50 cb	-1.25 362.5 km 65 cb
(2) Descent associated with large-scale precipitation evaporation	--	None	None	None	1.05 287.5 km 60 cb
(3) Ascent within large-scale cloud	--	None	-.34 387.5 km 35 cb	-1.25 362.5 km 40 cb	-2.73 312.5 km 35 cb
(4) Descent within or near large-scale cloud	.61 ← [At max detrainment] 500 km 40 cb	.82 537.5 km 40 cb	1.06 512.5 km 40 cb	1.46 362.5 km 25 cb	0.71 237.5 km 35 cb
(5) Maximum r_ℓ	0	0.05 437.5 km 37.5 cb	0.08 412.5 km 32.5 cb	0.06 387.5 km 32.5 cb	0.09 312.5 km 37.5 cb
(6) Maximum cumulus rainfall	--	1.02 462.5 km	1.27 437.5 km	1.00 387.5 km	.52 362.5 km
(7) Maximum large-scale rainfall	--	0.01 462.5 km	0.04 437.5 km	0.04 387.5 km	0.06 362.5 km

or depletion of water substance within the convective-cloud population because the convective-cloud water budget in each computational gridbox during each timestep is computed by assuming (section 2.3.2) that the population in that box is in steady state. It is possible to make an a posteriori check of this assumption for the domain as a whole by estimating the total cloud liquid water within convection using (2.16) with $b = 10^3$m, $\beta = 1.0$, and the values of ω (90 cb) at each grid point, (2.18) with estimates of p_b, p_t, and p_z, and a plausible profile of $r_{\ell c}$ with pressure. This procedure yields, for example, 32 ton m^{-1} at three hours and 19 ton m^{-1} at six hours, indicating that the rate of depletion of domain convective cloud liquid water is small relative to other terms in the water budget. There is insufficient information available to estimate the validity of the assumption in question within individual gridboxes.

The results of experiment N1 may be summarized as follows:

(a) The vertical circulation within the disturbance narrows and intensifies slightly for the first three hours, then weakens drastically.

(b) Rainfall from convective clouds is small by comparison with observations, indicating that with the large-scale environment present in this model, convection heating is probably less than would occur in nature.

(c) Propagating and amplifying internal gravity waves of horizontal wavelength 50-100 km appear in the region of convection below 50 cb by six hours and dominate the ω-field below 50 cb after nine hours.

(d) Above 50 cb a large-scale cloud forms and subsidence gives way to ascent under the influence of convection heating and large-scale condensation.

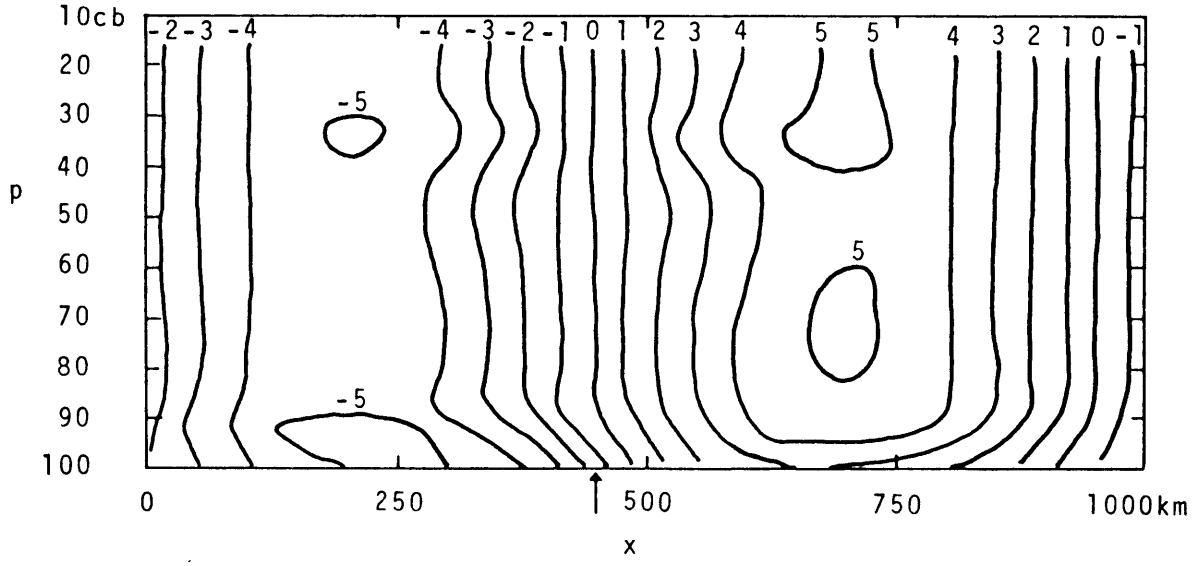
(e) Evaporation of large-scale precipitation appears to have only a minor effect on the time evolution of the flow.

We next examine each of these aspects in detail.

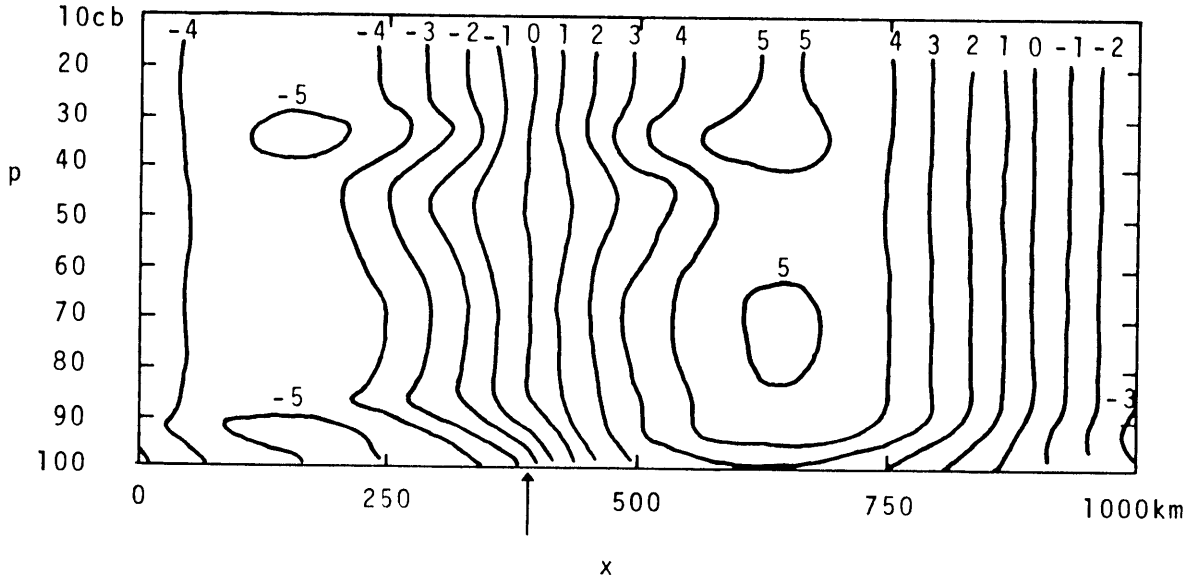
4.1.1 Narrowing and weakening of the large-scale disturbance

It is evident from figures 4-6a through c that the large-scale wave disturbance moves westward at roughly the speed of the -5 m sec^{-1} basic zonal current. We also observe that the disturbance narrows from a width of 400 km to 275 km during the first three hours as measured by the distance over which ω at 90 cb is continuously negative, but does not narrow substantially thereafter. Increase in intensity in the upward vertical motion during the first three hours is most pronounced above the 90 cb level; at 95 cb the magnitude of ω changes little. Subsequent to three hours, ω at 90 and 95 cb weakens, and the boundary layer character of the secondary flow disappears by nine hours as the vertical motion field in the boundary layer becomes simply a downward extension of the internal gravity wave activity (section 4.1.3 below).

The weakening of the initial disturbance is most dramatically illustrated by figure 4-7. In this figure the net upward mass flux through 90 cb (ton m^{-1} sec^{-1}) within the large-scale trough is plotted as a function of time. At nine hours and especially at twelve hours the estimate was made quite subjective by the presence of the internal gravity waves; the flux at nine hours is between χ = 225 and 425 km, and at twelve hours between χ = 25 and 525 km. Also on figure 4-7 is a similar plot for experiment N2, which is identical to N1 in all respects except that the boundary layer initialization employs "strategy 2," section 3.2.1. In con-

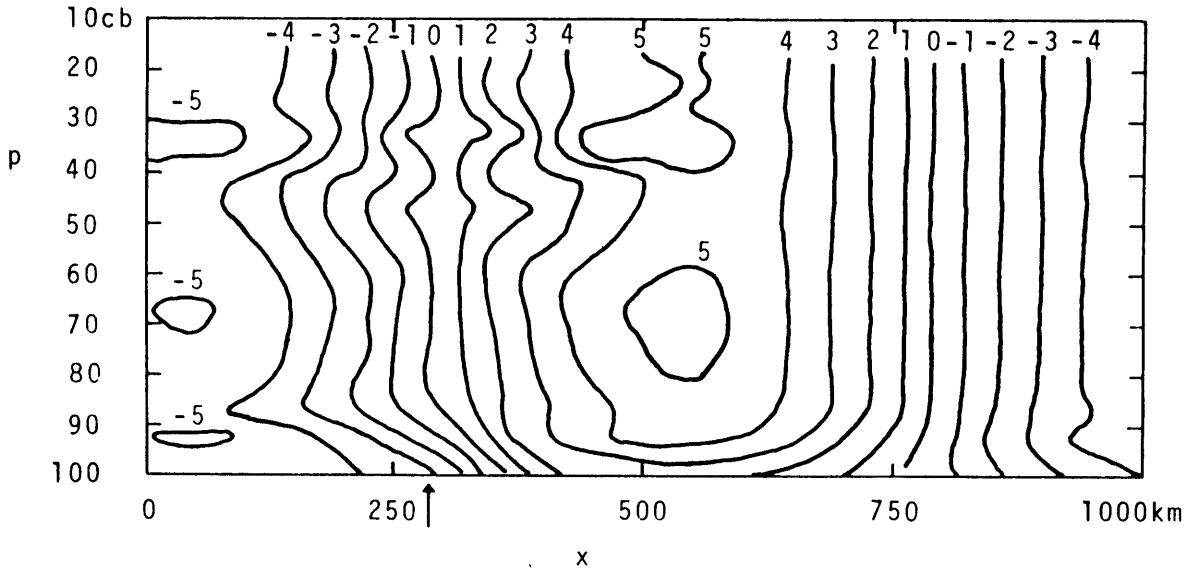


a. 3 hours



b. 6 hours

Figure 4-6. ~~, experiment N1. The vertically pointing arrow just below each figure marks the trough-axis position based on a constant westward movement of 5 m sec^{-1} from λ = 500 km initially. Isotachs are labeled in m sec^{-1}.



c. 12 hours

Figure 4-6. (Continued)

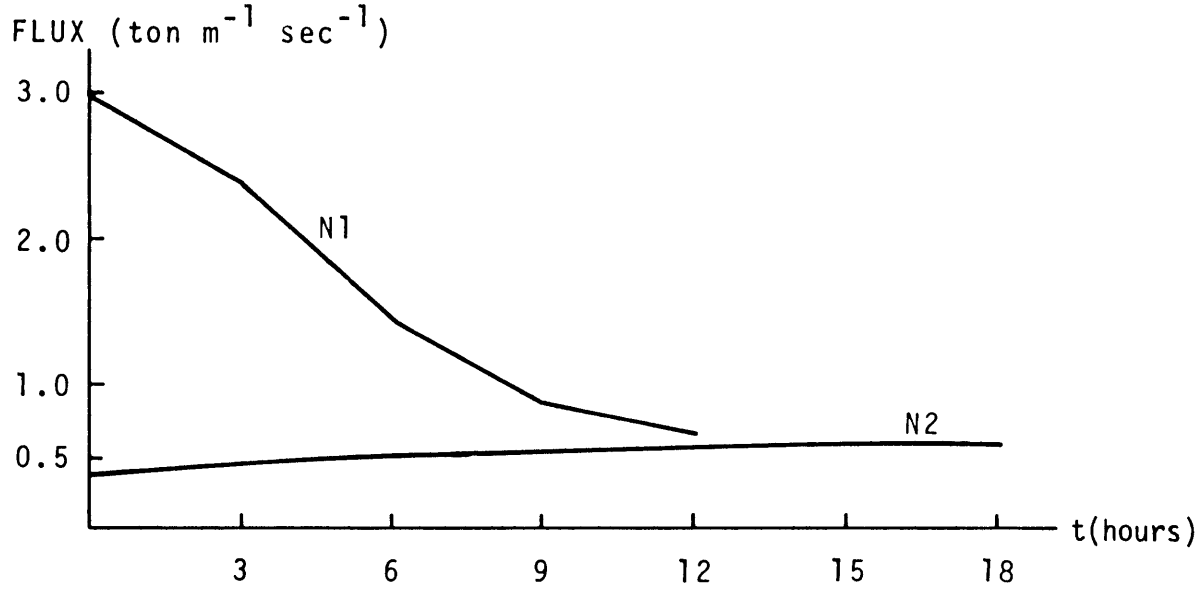


Figure 4-7. Upward mass flux through 90 cb within the large-scale disturbance as a function of time, runs N1 and N2. See text for additional details.

trast to experiment N1 the mass flux out of the 90-100 cb layer increases slowly; in fact the mass flux out of the boundary layer for the two runs seems to converge to a value of about 0.6 ton m^{-1} sec^{-1}. It is therefore clear that the behavior of runs N1 and N2 is similar to runs D6 and D4 (see figure 3-2 and table 3); the convection heating is insufficient to establish an amplifying direct vertical circulation in experiment N1.

We next investigate the details of the demise of the large-scale trough. This we may do by focusing on the evolution of the horizontal convergence, and, by implication, of ω . We may write (2.1) in the form

$$\frac{\partial u}{\partial t} = - u_g \frac{\partial u}{\partial x} - (u-u_g) \frac{\partial u}{\partial x} - \omega \frac{\partial u}{\partial p} + f(v - v_g) + F_x . \quad (4.1)$$

Because the important trends in horizontal convergence occur in the boundary layer, we will concentrate on the 97.5 and 92.5 cb levels. We have plotted (figure 4-8) the last four terms of (4.1) as a function of x at these two levels for the initial time, and at three and six hours. On figure 4-9 are plots of these four terms at 97.5 and 92.5 cb for experiment N2, at the initial time and at six hours. In these figures the nonlinear advective terms, $-(u-u_g)\frac{\partial u}{\partial x}$ and $-\omega \, \partial u/\partial p$, are added together. The individual terms are similar, with the horizontal advection usually having the larger amplitude. At the initial time the values of all nonviscous terms are computed from the Fourier components of u , v, ω and Φ . At three and six hours they are estimated from the printouts of u , v, ω and Φ . The sum of the last four terms in (4.1) is the local change of u in a coordinate system moving westward at u_g = -5 m sec^{-1}, and is shown as a solid line on the figures. We postpone discussion

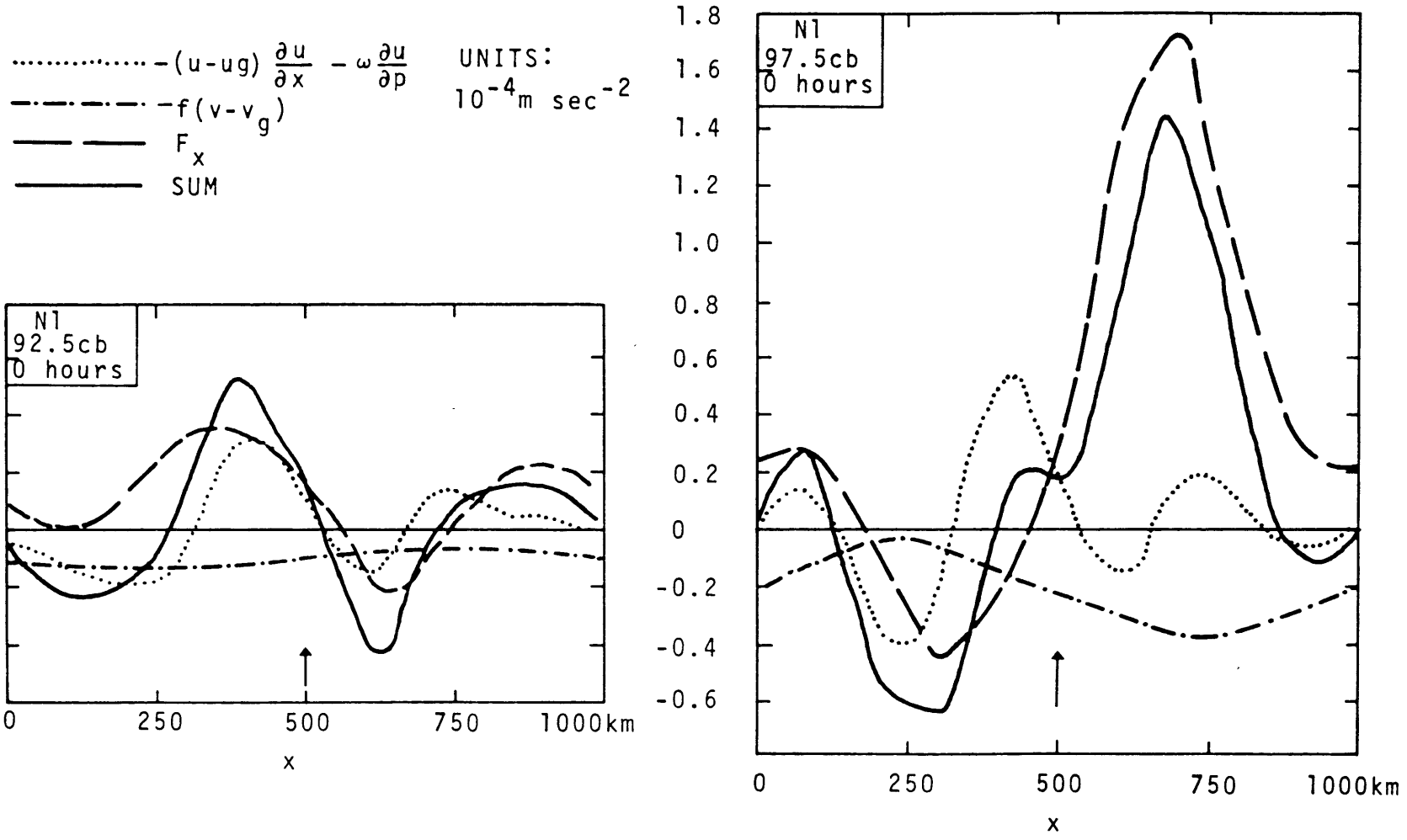


Figure 4-8. Comparison of the last four terms in (4.1), experiment N1. The legend above the 92.5 cb, zero-hour diagram applies also to figures 4-9 and 4-19. The vertically pointing arrows mark the trough axis position based on a constant westward movement of 5 m sec^{-1}.

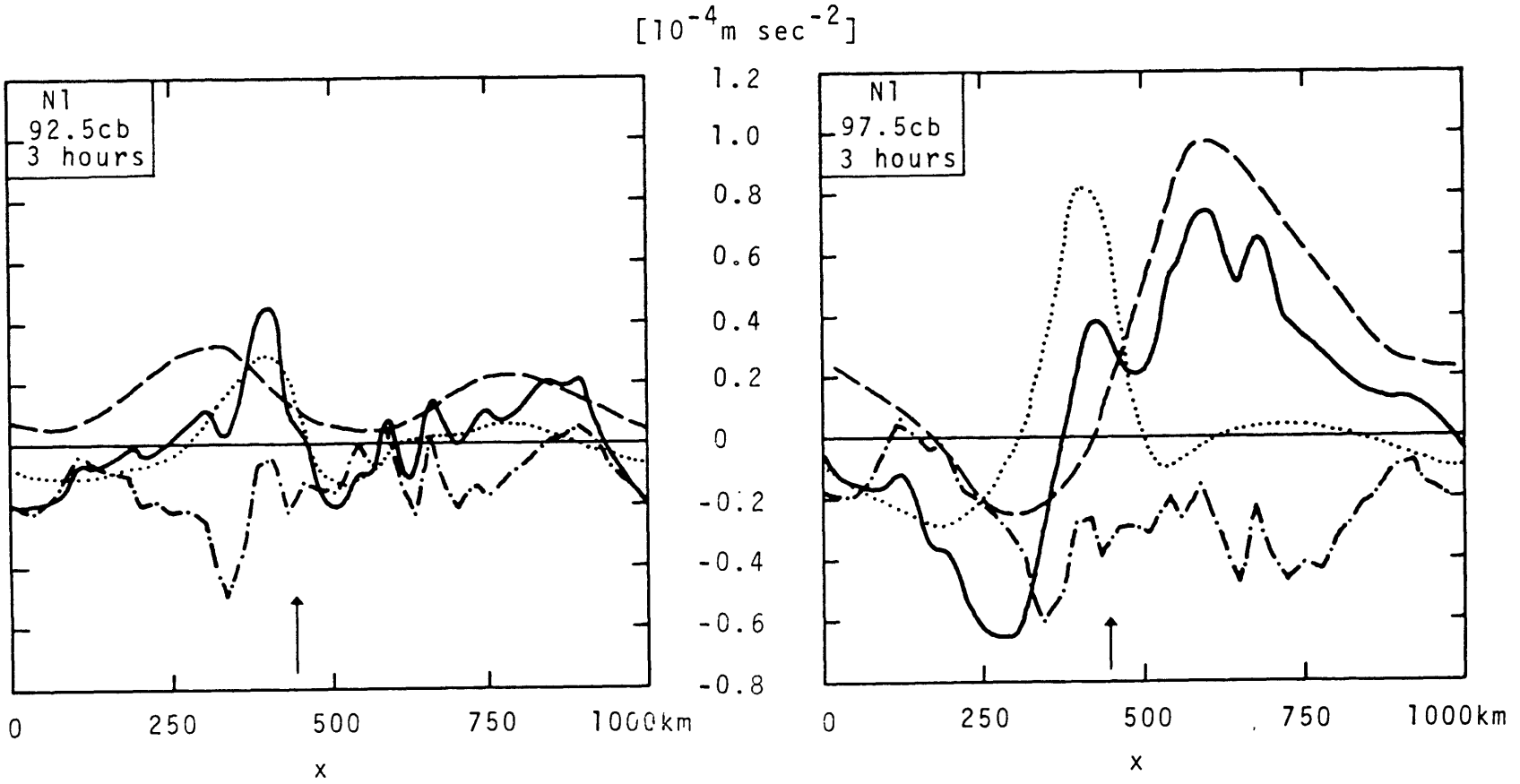


Figure 4-8. (Continued)

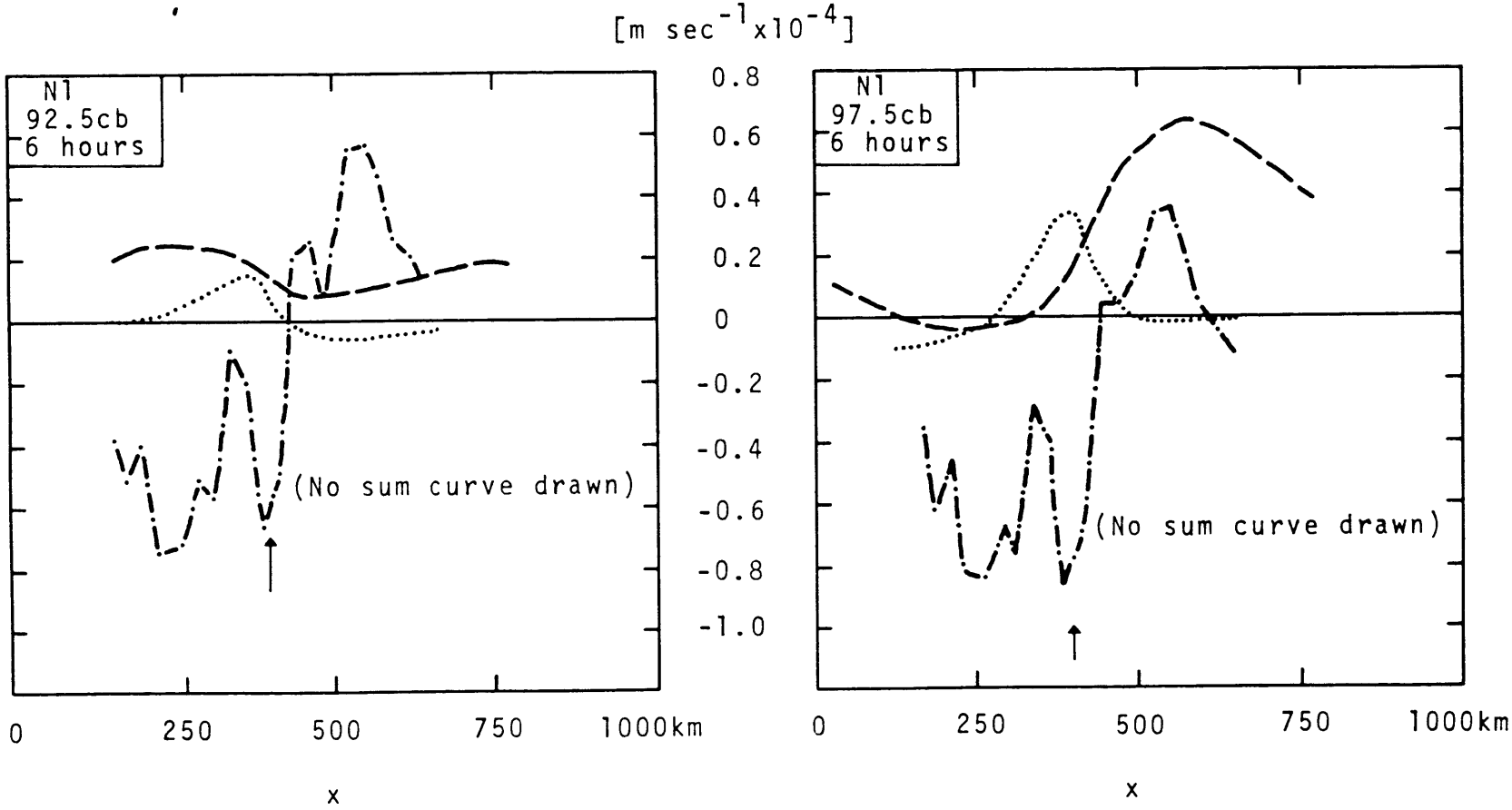


Figure 4-8. (Continued)

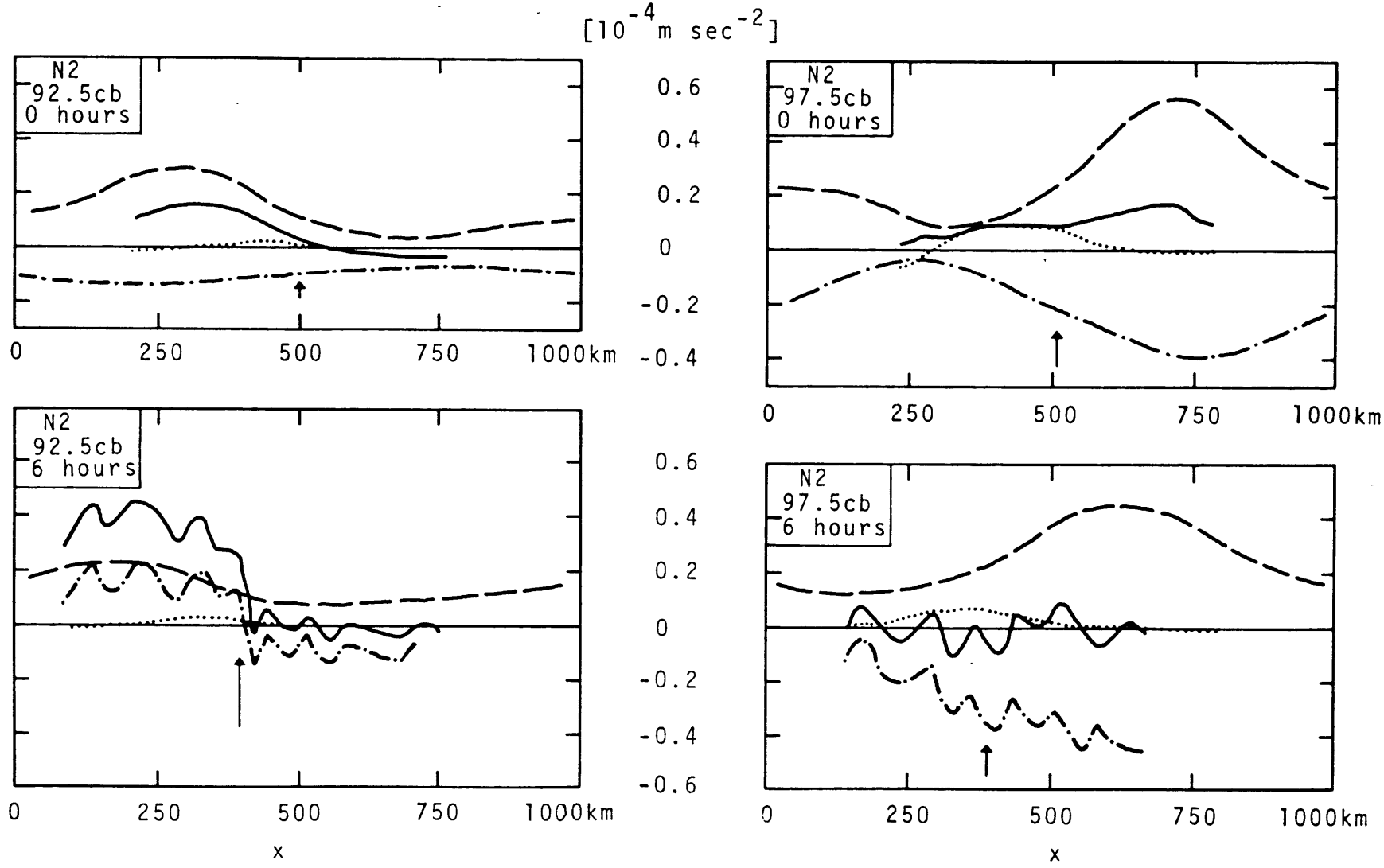


Figure 4-9. As figure 4-8, experiment N2.

of x-variations of $f(v-v_g)$ which are of length scale $\leqslant$ 100 km until section 4.1.3.

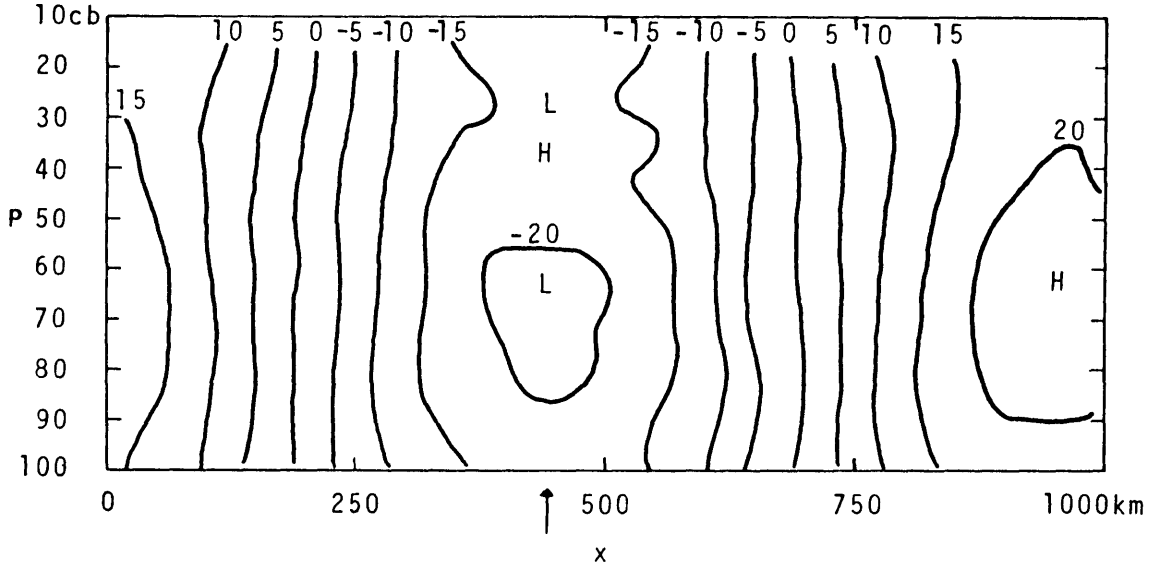
The generalized Ekman solution used to initialize the boundary layer does not take into account that portion of the horizontal divergent flow, manifested principally as strong inflow toward the trough axis at 97.5 cb, corresponding to the heating-induced ω. Consequently, there is, initially, inbalance between $f(v-v_g)$ and F_x in runs N1 and N2; during each run friction diffuses this inflow up into the rest of the boundary layer. Initially and at three hours the sum $f(v-v_g)+F_x$ is clearly in the sense of weakening the 90 cb vertical motion of experiment N1. Why, then, do we observe it to increase during the first three hours? Nonlinear advection acts to increase convergence in the 90-100 cb layer along the trough axis, but weakens it beyond a distance 50-75 km away from the axis. We conclude that nonlinear advection is responsible for the narrowing of the disturbance in experiment N1 and that this advection and <u>not</u> convection heating brings about the slight increase in large-scale upward motion at the trough axis. When the disturbance as a whole is considered, however, the weakening tendency of $f(v-v_g)+F_x$ is responsible for the decrease in upward mass flux through 90 cb noted on figure 4-7.

Because of the smaller $|\omega|$, the nonlinear advective terms in (4.1) are relatively less important in experiment N2 than in N1. Only in experiment N2 can the boundary layer be accurately described as a (stratified) Ekman layer. The narrowing of the region of ascent occurs much more slowly than in N1, from a width of about 400 km initially to about 350 km at three hours and 325 km at six hours. Maximum upward motion increases from $-.24 \times 10^{-4}$ cb sec^{-1} to $-.27 \times 10^{-4}$ cb sec^{-1} during this period.

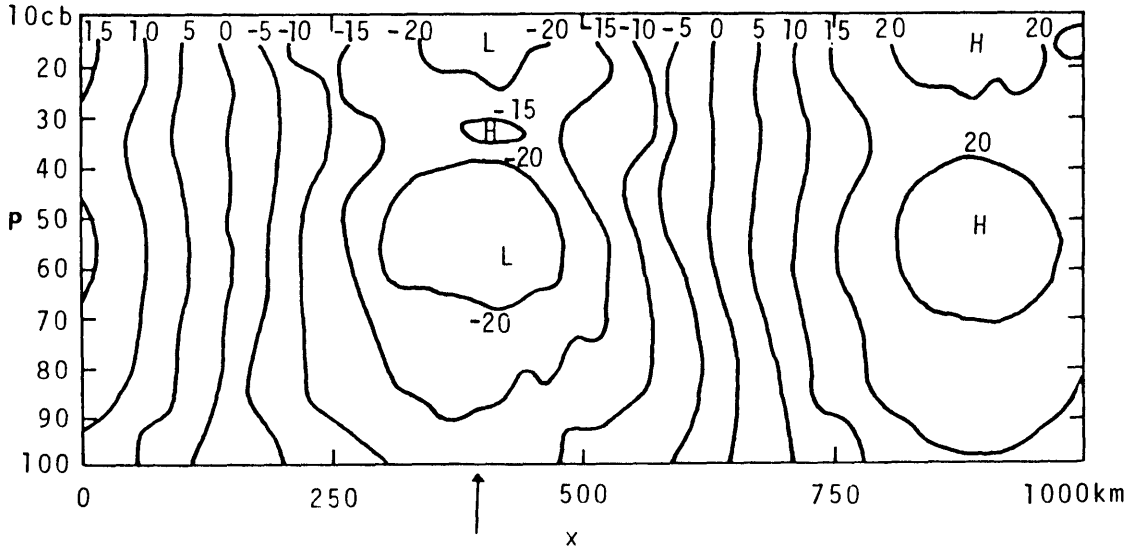
Decay of the large-scale transverse circulation in experiment N1 accelerates after three hours. The $f(v-v_g)$ term becomes highly destructive of convergence at both 97.5 and 92.5 cb by six hours. The growth in magnitude of $f(v-v_g)$ derives from diverging trends in v and v_g. We see from figures 4-1 and 4-6 that there is both a concentration and an increase of the relative vorticity, $\partial v/\partial x$, at low levels along the trough axis; non-geostrophic advection and convergence are responsible.

Initially the contours of $\Phi-\hat{\Phi}$, $\hat{\Phi}$ = x-average of Φ, are vertical, consistent with the initial distribution of v_g (section 3.1). If the zonal components of the pressure-gradient force and the Coriolis force are to remain balanced in spite of the concentration of relative vorticity, we should see intensification of the trough in the field of $\Phi-\hat{\Phi}$. Figure 4-10 shows that instead the trough weakens, further throwing the zonal motion out of balance. This weakening is associated with the development of a cold core in the trough below 70 cb, and especially below 85 cb, during the first six hours. An analogous weakening trend is observed in the ridge. By six hours the temperature at 92.5 cb within the trough is about 0.3 C colder than along the ridge line.

During the first six hours of experiment N2 convergence and ageostrophic advection of $\partial v/\partial x$ are insufficient to completely counter the vorticity dissipation, and the low level vorticity maximum weakens slightly. Only a meager low level cold core develops in the trough by six hours; the temperature difference between trough and ridge at 92.5 cb is only about 0.08 C. The six hour $\Phi-\hat{\Phi}$ field (not shown) closely resembles a westward translation of the initial field. As a consequence the x-variation of $f(v-v_g)+F_x$ is weakly in the sense of generating convergence in



a. 3 hours



b. 6 hours

Figure 4-10. $\Phi - \hat{\Phi}$, experiment N1. Contours labeled in m^2 sec^{-2}.

the trough when the whole layer 90-100 cb is considered. This is consistent with the slow increase in upward mass flux through 90 cb during the first six hours. At 12 and 18 hours, the estimate of upward mass flux is made subjective by the presence of internal gravity waves (section 4.1.3) which begin to obscure the initial disturbance. We see that whatever intensification is occurring is very slight and, during the first six hours at least, is apparently not a direct result of cumulus convection heating.

The difference in behavior between experiments N1 and N2 can only be attributed to the difference in initialization procedure and reinforces the conclusion of chapter 3 that "strategy 2" is intrinsically superior. The heating due to convection is insufficient to prevent the transverse circulation in run N1 from becoming indirect.

4.1.2 Parameterized convection and comparison with observation

We recall from section 2.3.2 that the influence of convection upon the large-scale changes of θ (i.e., T) and r_v appears as $C_\theta - P^{-\kappa}(L/c_p)E_c$ in equation (2.5) and as $C_{r_v} + E_c$ in (2.7). To facilitate comparison with other studies the heating terms in (2.5) are multiplied by P^{κ}. The terms, $-(L/c_p)E_c$ and E_c describe the rate of change of the large-scale temperature and mixing-ratio fields resulting from *in situ* evaporation of water detrained from convective cloud. The terms $P^{\kappa}C_\theta$ and C_{r_v} incorporate all other influences. We obtain E_c by a saturation adjustment process in which all detrained liquid water evaporates unless the large scale becomes saturated. If the large scale is saturated, only a portion of the detrained liquid water evaporates,

specifically, that required to maintain saturation in the face of warming by C_θ . Any detrained liquid water which does not so evaporate becomes part of a "large-scale cloud" ($r_\ell > 0$) and if subsequent evaporation of this cloud water occurs it is incorporated in E_ℓ . Referring to (2.21) with q_e replaced by $\bar{q}$, using the definition (2.17) that the upward mass flux within convective clouds, $M_c = \rho q_m$, and differentiating by parts,

$$p^\chi C_\theta = g\left[-p^\chi M_c \frac{\partial \bar{\theta}}{\partial p} + q_m \frac{\partial h}{\partial p}(T_c - \bar{T})\right] \tag{4.2}$$

$$C_v = g\left[-M_c \frac{\partial \bar{r}_v}{\partial p} + q_m \frac{\partial h}{\partial p}\left[r_s(T_c, p) - \bar{r}_v\right]\right]$$

The saturation mixing ratio corresponding to cloud temperature T_c at pressure p is $r_s(T_c, p)$. $\bar{T}$, $\bar{\theta}$ and $\bar{r}_v$ refer to large-scale values. Analogous expressions are derived by Arakawa and Schubert (1974), and many others. The first term on the righthand side of (4.2), commonly referred to as "compensating subsidence," warms and dries the large scale. The second is the detrainment of saturated cloud air having temperature T_c . The term, $p^\chi C_\theta$, is negative if and only if $T_c - \bar{T} < (p^\chi \partial\theta/\partial p)\left[1/\rho(\partial h/\partial p)\right]^{-1}$, which is always negative. This inequality is only satisfied near the level of maximum cloud top, p_t , and then only if $T_c - \bar{T}$ is negative at this level. This latter condition is determined by the solution of (2.15), which incorporates the effect of liquid water on buoyancy; the larger is r_{cm} , the maximum cloud water mixing ratio, the less likely is the cloud temperature

at p_t to be colder than that of the environment at p_t . Only when $T_c - \bar{T} < 0$ in a layer which is close to or at saturation does adjustment to saturation conditions (step 8, table 1) imply E_c to be negative. If any detrained water remains unevaporated after this saturation adjustment, and if $T_c = \bar{T}$, the net convection heating, $p^{\kappa} C_\theta - (L/c_p) E_c$, is positive if the large-scale temperature lapse rate is less than the moist adiabatic, and conversely. If this lapse rate is moist adiabatic, with the large scale saturated net heating equals $g \rho_m (\partial h / \partial p)(T_c - \bar{T})$. When there is concentrated detrainment within large-scale cloud, the net heating by convection is thus strongly dependent on τ_{ecm} : a large τ_{ecm} favors heating.

Figure 4-11 depicts the heat budget of the first three hours for the gridcolumn centered at 462.5 km. Curves depicting $p^{\kappa} C_\theta$ and $-(L/c_p) E_c$ at later times of experiment N1 and in other runs, both shear and no-shear, do not qualitatively differ in shape from those of figure 4-11. This vertical structure can be interpreted in terms of the cloud-top distribution function, h , defined by (2.17) and (2.18) and the large-scale temperature lapse rate. The fraction of the cloud population that is assumed "mature," h_m , is assigned the value .33 for all runs, but the cloud base pressure, p_b , the pressure at maximum cloud top, p_t , and the pressure at which clouds first lose buoyancy, p_1 , are all functions of the large-scale stratification, and so are variable in time and space. The h-profile depicted in figure 2-2 is for a cloud population having larger p_1 and p_t then the population which contributes to figure 4-11. This profile is nevertheless representative. The "mature-cloud detrainment layer," bounded by p_t and $2p_1 - p_t$, is the scene of

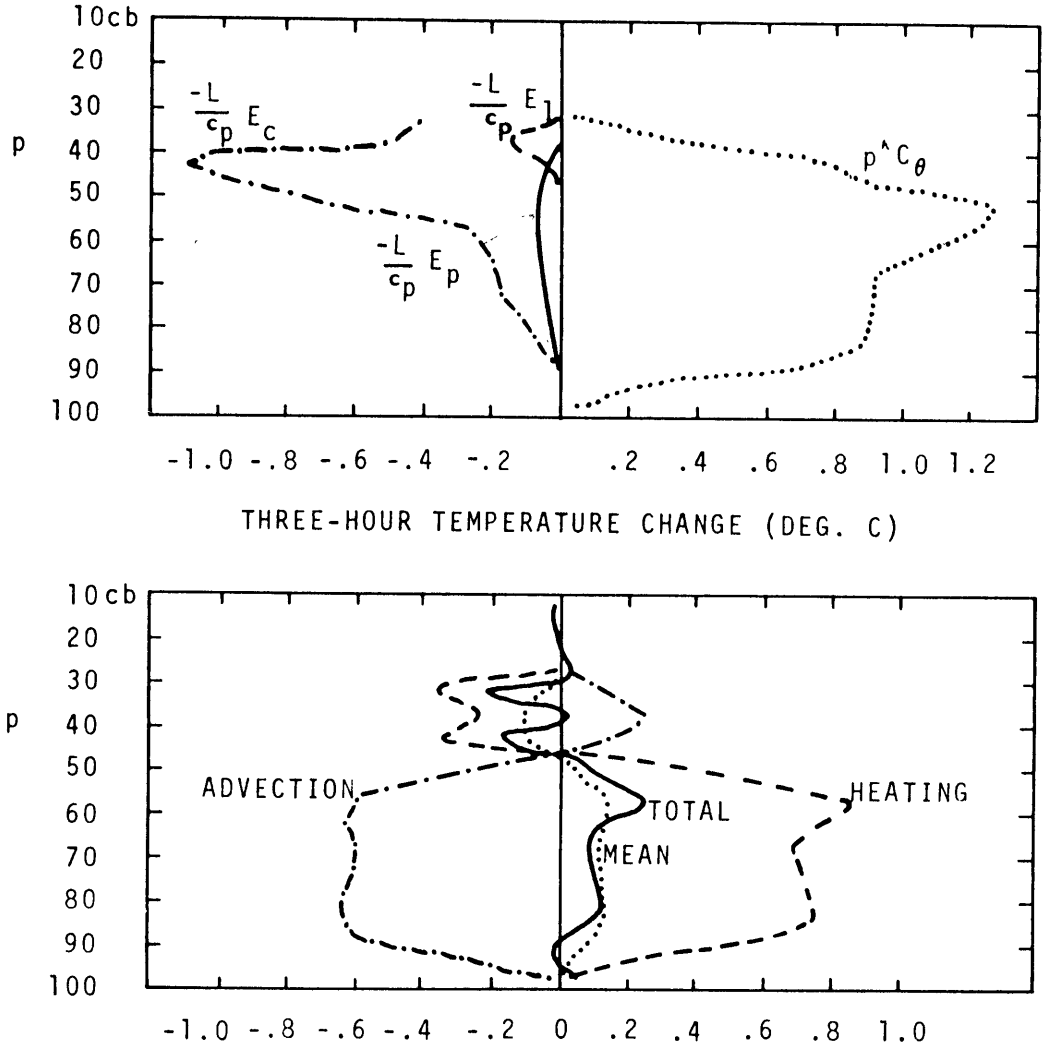


Figure 4-11. Experiment N1 heat budget in gridcolumn centered at 462.5 km, for the first three hours. The top diagram gives the vertical distribution of all the heating terms, which sum to the curve labeled "heating" in the lower diagram. The "advection" curve is obtained by subtracting the heating curve from the observed three-hour change of temperature ("total" curve). The "mean" curve is $\theta - \hat{\theta}$ at 462.5 km.

over 50% of the detrainment and so is the region in which the most concentrated detrainment (per unit pressure interval) occurs. From cloud base up to $2p_1 - p_t$, detrainment and M_c slowly increase as p linearly decreases.

Maximum cumulus cloud top falls initially within the 35-40 cb computational layer, but is found in the 30-35 cb layer after one hour. The base of the mature-cloud detrainment layer probably also rises somewhat but remains in the vicinity of 50 cb. The instantaneous discontinuity in detrainment rate at $2p_1 - p_t$ is smoothed somewhat by taking the budget over a three-hour period, but is still evident on figure 4-11. Below the concentrated detrainment layer, $T_c - \bar{T} \leq 1.5$ C; "compensating subsidence" is the principal contributor to $P^{-\kappa} C_\theta$. Since $\partial\theta/\partial p$ increases above 65 cb, the $P^{\kappa} C_\theta$ maximum occurs near the bottom of the concentrated detrainment layer, where M_c is maximum. The term, $-(L/c_p) E_c$, is comparatively small but increasing in magnitude with height below 55 cb. This is a reflection of modest detrainment, and, below 80 cb, that cloud liquid water content, $r_{\ell c}$, is less than $r_{\ell cm}$, the maximum permissible. The term, E_c, is initially very large above $2p_1 - p_t$. This leads to formation of a large-scale cloud at 37.5 cb along the trough axis by 45 minutes. The consequent reduced evaporation of detrained water shows up as the large decrease in E_c between 42.5 cb, which remains unsaturated, and 37.5 cb, and as a relative maximum in net convection heating, $P^{\kappa} C_\theta - (L/c_p) E_c$, at 37.5 cb. The consequences of this are of sufficient interest to warrant more detailed discussion in section 4.1.4, below.

Wherever there is convection we may write (2.5) as follows, using (4.2) together with $M_c(p_b) = -\left[\bar{\omega}(900cb)/g\right]$, and ignoring detrainment and non-convective heating:

$$\frac{\partial \bar{\theta}}{\partial t} = -u_g \frac{\partial \bar{\theta}}{\partial x} - (u - u_g)\frac{\partial \bar{\theta}}{\partial x} - \left[\bar{\omega} - \beta\,\bar{\omega}(900cb)\,\frac{M_c(p)}{M_c(p_b)}\right]\frac{\partial \bar{\theta}}{\partial p} \qquad (4.3)$$

The overbar indicates a large-scale variable. The term $-(u-u_g)\,\partial\bar{\theta}/\partial x$ is everywhere small in magnitude during the first six hours of experiment N1 by virtue of both the small magnitude of $(u-u_g)$ and of $\partial\bar{\theta}/\partial x$. The $\partial\bar{\theta}/\partial p$ term in (4.3) therefore approximately describes the local rate of change of θ with respect to a coordinate system moving westward with the disturbance. At the trough axis during the first six hours of experiment N1, $-\bar{\omega}(p) \lesssim -\bar{\omega}(900cb)$ and, below about 55 cb, $M_c(p) > M_c(p_b)$, and detrainment is small. The warming above 85 cb is thus accounted for. At 92.5 and 87.5 cb, $-\bar{\omega} \approx -\bar{\omega}(900cb)$, and $M_c \approx M_c(p_b)$, so that heating by convection closely balances cooling resulting from large-scale ascent; the boundary layer experiences no warming. At the ridge axis, $-\bar{\omega}\,\partial\bar{\theta}/\partial p$ is positive above 95 cb. Hence, the trough becomes cooler than the ridge between 95 and 85 cb; in fact, during the first six hours, the temperature difference between ridge and trough increases at roughly the same rate as in experiment D6. On figure 4-11 the trough is also seen to be cold with respect to the domain x-average, consistent with the geopotential field depicted in figure 4-10. The same processes also occur during experiment

N2. Vertical motion during the first six hours of that run is only 20 to 25% of that during the corresponding portion of run N1, and the temperature difference between ridge and trough is proportionally smaller.

The water-vapor budget at 462.5 km contemporaneous to figure 4-11 is shown in figure 4-12. (Individual curves of $C_{\sim}$ and E_c are depicted in figures 4-14 and 4-15.) Convection dries the large scale below 55 cb; compensating "subsidence" dominates over detrainment. This drying is nearly balanced by advection, which is principally due to the large-scale upward motion. Subgrid-scale diffusion of water evaporated from the sea plays only a minor role.

Knowledge of how cumulus convection affects the heat and moisture budgets on larger scales is sketchy. Consequently, there is no completely adequate procedure for judging the validity of our parameterization. In this discussion we will make use of the recent observational studies by López (1972), Ogura and Cho (1973), Reed and Recker (1971), and Yanai, Esbensen and Chu (1973). (Henceforth these will be referred to as L, O, R, and Y, respectively.) Table 6 summarizes the data sources and procedures of each of these. It is important to note that each involves time averaging or compositing in some form. Studies of this type on individual tropical disturbances are not yet available. An important element of the studies of L, O, and Y is the presence of a spectrum of cloud sizes, either observed (L), computed (O), or implied (Y). The dynamics of the cloud model used by O and Y are identical to those discussed in chapter 2. L's cloud model (1973) is somewhat more complicated.

Some properties of the composited disturbance (L and R) or of the time-averaged flow field (O and Y) are given in table 7. For comparison,

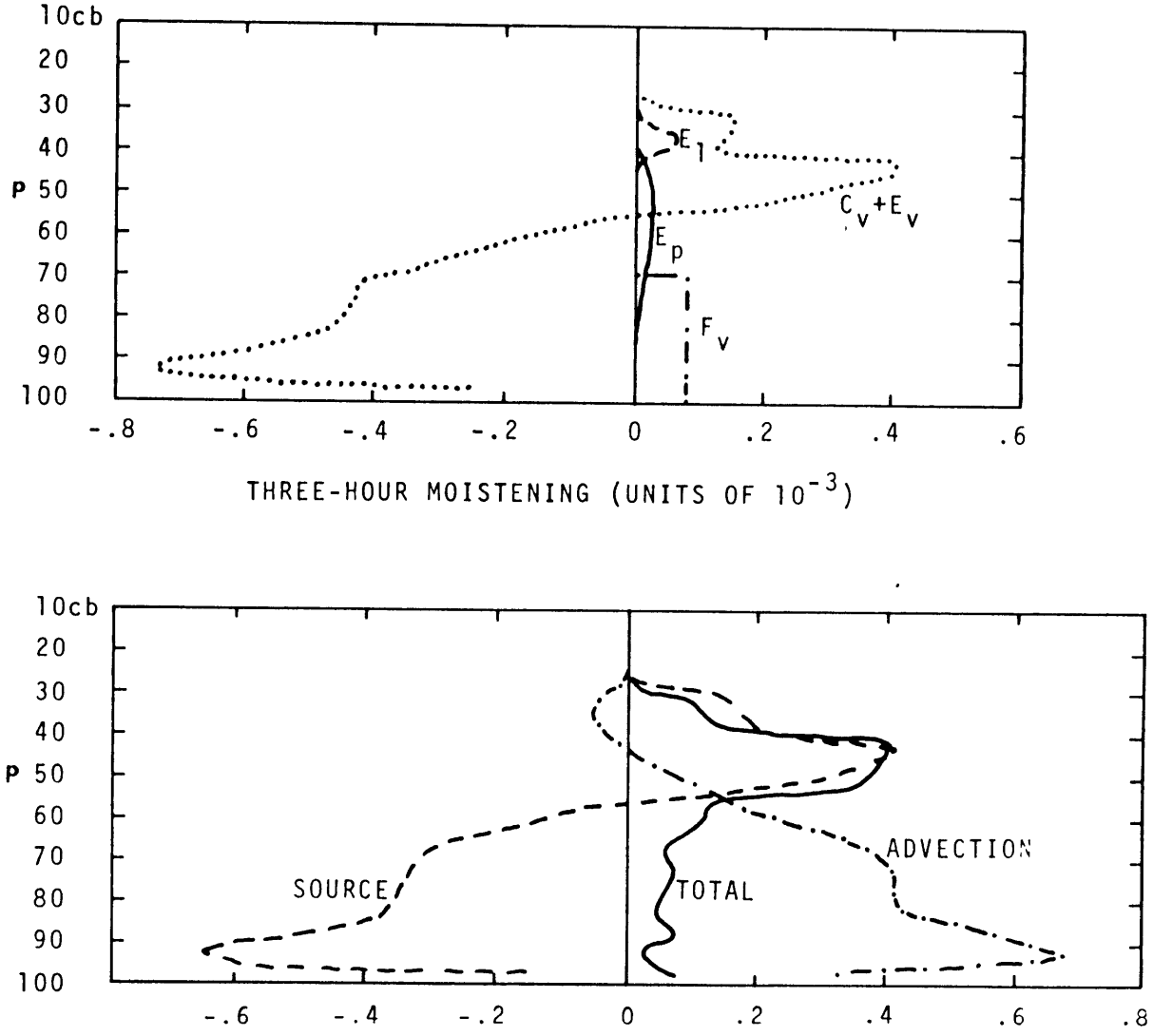


Figure 4-12. Experiment N1 water vapor budget in gridcolumn centered at 462.5 km, for the first three hours. The top diagram gives the vertical distribution of all source terms, which sum to the curve labeled "source" in the lower diagram. The "advection" curve is obtained by subtracting the "source" curve from the observed three-hour change of r_v ("total" curve).

Table 6. Observational studies of cumulus ensembles

Study	Data source	Estimated min resolvable scale	Procedure
L (López, 1972)	T and r_w sounding from Caribbean disturbances August-September, 1968. (u, w, ω) from Williams and Gray (1973) composite of 537 "conservative" cloud clusters in central and western Pacific	$\sim$ 800 km	Basic tool is cloud model of Lopez (1973). Spectrum of total upward mass flux through cloud base during cloud lifetimes is inferred from Caribbean disturbance radar study. The resulting cloud population is tuned to 25 mm day^{-1} rainfall, that estimated by Williams and Gray (1973) from moisture convergence into conservative clusters.
O (Ogura and Cho, 1973)	April-July, 1956 average of 4 times daily Marshall Islands radiosonde data (Nitta, 1972)	$\sim$ 1500 km	Basic cloud model is one-dimensional, updraft only, constant radius. Detrainment is at level of 0 buoyancy. Convective precipitation is parameterized, with no evaporation. Spectrum of cloud sizes obtained to produce convection heating implied as residual from earlier study by Nitta on same data.
R (Reed and Recker, 1971)	Twice daily radiosonde data, July-September, 1967, in Kwejalein, Enewetok, Ponape triangle, composited with respect to phase of large-scale disturbance.	$\sim$600 km	No explicit cloud model used. Cloud environment vertical motion is obtained by adiabatic method. Cloud-scale nonbuoyant saturated downdraft mass flux is implied from residual of cloud-environment moisture budget. In-cloud upward mass flux computed as residual of the above 2 fluxes and the kinematic, large-scale (mean) ω .

Table 6. (continued)

Study	Data source	Estimated min resolvable scale	Procedure
Y (Yanai, Esbensen, and Chu, 1973)	April-July, 1956, 4-times daily Marshall-Islands radiosonde data	$\sim$1500 km	Similar to 0 except that the computations are made for each observation time and the average of all these is presented.

Table 7. Comparison of various N1 results with observation. Precipitation efficiency of convection is defined as "implied" rainfall ÷ upward flux of water vapor through cloud base. The relative vorticity, ω, and rainfall of study L are from Williams and Gray (1973). "Implied" rainfall is that computed to fall out of the derived convective-cloud population. The row labeled "B" is data from experiment N1, the first three hours in the gridcolumn centered at 462.5 km

Study	90 cb Relative vorticity [sec^{-1}]	90 cb Large-scale ω [cb sec^{-1}]	Rainfall [mm day^{-1}]	Precipitation efficiency of convection	Observed rainfall rate ÷ $-\left(\frac{\omega}{g} r_v\right)\Big\|_{90cb}$
L	$.9 \times 10^{-5}$	$-.56 \times 10^{-4}$	25	$\leqslant .37$	3.0
O	not available	$-.23 \times 10^{-4}$	11 (implied) 9.6 (observed)	.28	2.9
R	$.8 \times 10^{-5}$	$-.51 \times 10^{-4}$	15.3 (implied) 22 (observed)	$\sim .80$	3.1
Y	$.5 \times 10^{-5}$	$-.35 \times 10^{-4}$	18 (implied) 10 (observed)	.47	2.0
B	3.1×10^{-5}	-1.2×10^{-4}	8.2	.44	.48

the same parameters for the first three hours of run N1 are also listed. An approximation for the ratio of the convective-cloud rainfall to the total mass of water substance which passes upward through cloud base or is entrained above cloud base is provided by our definition of precipitation efficiency. "Implied" rainfall is that computed to fall from the convective cloud population of O and Y, and is a residual of R's moisture budget.

Table 7 data from the observational studies suggests a linear relationship between the relative vorticity at 90 cb and the 90 cb ω . Extrapolation of this relationship to the vorticity of N1 gives a 90 cb ω of -2×10^{-4} cb sec^{-1} at the trough axis. In the foregoing section we argued that the 90 cb ascent in experiment N1 (initially, -1.17×10^{-4} cb sec^{-1}) is itself artificially large because stratification in the Ekman layer has been ignored in the initialization. Thus there is a substantial discrepancy between observation and the most accurate model results without shear and with $\beta = 1.0$. A definitive explanation for this is elusive; discrepancy of scale and hence of the influence of stratification (Kuo, 1973, and section 3.2.1 of this work) and of nonlinearities, errors arising from compositing, and, by comparison to L, R, and Y, reduced heating by convection relative to ω at 90 cb are offered as possibilities.

Although they are not shown, it is worthwhile nothing that the observed vertical profiles of large-scale ω computed by these authors (L used Williams and Gray, 1973) are similar: little boundary layer character is evident, i.e., divergence is not concentrated near the surface, and the minimum ω is reached at 30-50 cb, being from 2.5 (R) to 4 (Y) times the value at 90 cb. This contrasts sharply with the vertical profiles of ω in experiments N1 and N2, particularly at the initial time. Differ-

ence in the vertical distribution of convection heating is likely responsible for this discrepancy.

Uncritical acceptance of these observational studies and of their relevance to our numerical work is precluded by the use of composited or averaged data and by the disparity in horizontal scale. To the extent that the influence of convection upon a larger scale is a nonlinear function of the large-scale variables, neither simple averaging nor compositing can be depended upon to reveal an accurate relationship. Stated another way, there is no guarantee that the composited or averaged disturbance, including the inferred convection, represents an instantaneously observable state of the atmosphere. A crude example of how such inconsistency may arise in the case of Y's averaging procedure is seen in the following. Assume that in fact $M_c = \bar{M}$, i.e., that the large-scale mass flux equals the mass flux upward in convective clouds when $\bar{M} > 0$, but that $M_c = 0$ if $\bar{M} \leq 0$. Then, in arbitrary units, a time average of $\bar{M}$ of 1 is implied by the $\bar{M}$ - time sequence: 3, 3, 1, -1, -1. However, the time average of M_c is 1.4, whence $M_c/\bar{M} = 1.4$. We do not intend to suggest that such an overestimate has been made, but the possibility exists.

It is clear from table 6 that the horizontal scale described by the observational studies is an order of magnitude larger than that resolvable in our numerical model. In the jargon of the GATE (GARP Atlantic Tropical Experiment), the observational studies monitor only the A:D or B:D scale interactions, whereas this model is designed for the expressed purpose of studying the B:C and C:D interactions. (A, "wave" scale, 10^3 to 10^4 km; B, "cluster" scale, 10^2 to 10^3 km; C, "mesoscale," 10-10^2 km; D, "cumulus" scale, 1-10 km; Betts, 1974). Convection within a tropical disturbance is

frequently organized on the mesoscale; the relationships between the mesoscale flow field and convection are likely to be at least quantitatively different from those between the cluster or wave scale and convection.

Another limitation of these studies, particularly those of L, O, and Y, is use of simplified convective-cloud models. For example, convective-scale downdrafts are ignored by the models of O and Y. We speculate that inclusion of these would provide a portion of the cooling and moistening of the lower troposphere which these studies attribute to the large number of small clouds.

Keeping in view these cautionary remarks, we note the following points of disagreement between L, O, R, Y and B, as revealed by table 7 and figures 4-13, 14 and 15:

(a) The linkup of convection with the large-scale through $M_c = -\omega(90cb)/g$ produces less convective activity than observed, i.e., β is observed to be greater than one.

(b) Observed cloud populations possess a spectrum of sizes, the effects of which are not duplicated by the cloud populations assumed in the model.

(c) Liquid water content of detrained cloud air is considerably larger in our model than is indicated by these studies.

The rightmost column of table 7 shows that the studies of L, R, and Y are consistent in finding the ratio of rainfall rate to upward moisture flux on the large scale through 90 cb to be several times that of experiment N1. That this is a consequence of $M_c/\bar{M} >> 1$, and not of highly "efficient" convection is evident from table 7 and figure 4-13.

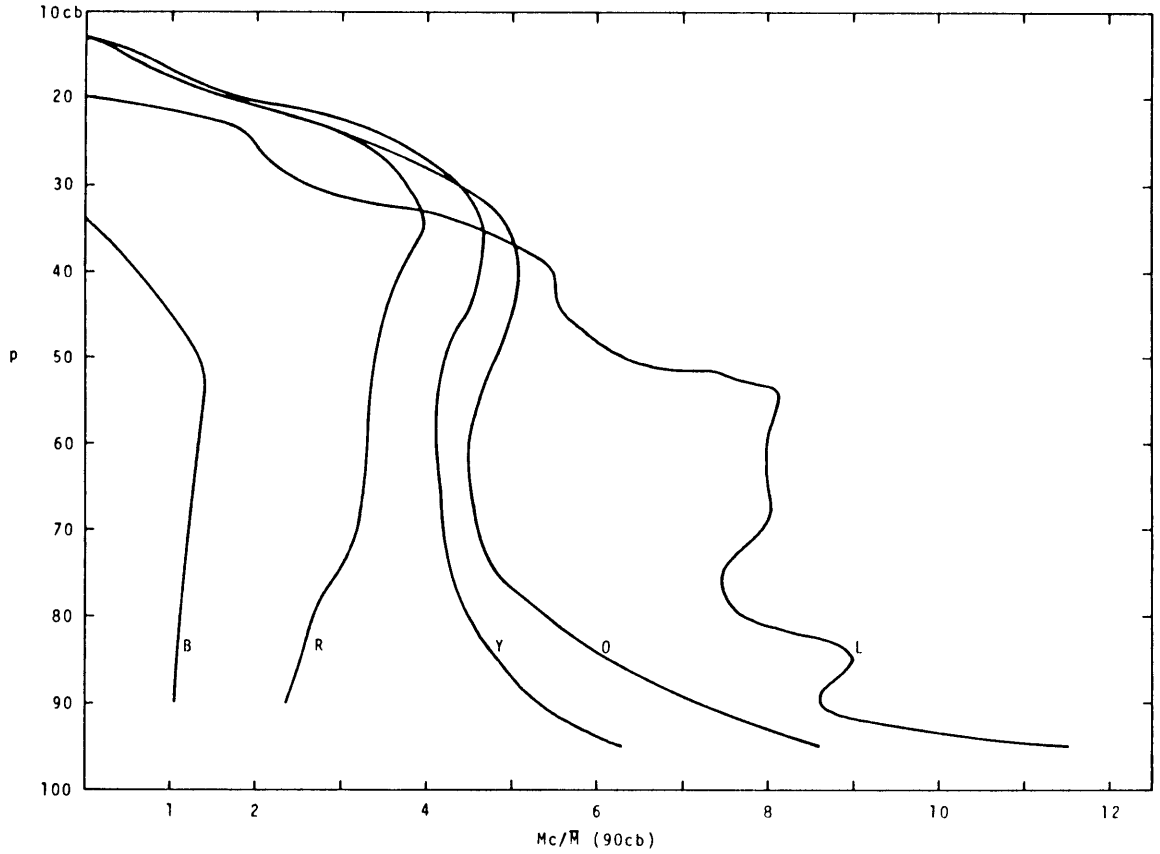


Figure 4-13. Normalized in-cloud mass flux, $M_c/\bar{M}(90cb)$, derived from the observational studies of table 6. The curve labeled "B" is an estimate of this flux for the first three hours of experiment N1 at 462.5 km.

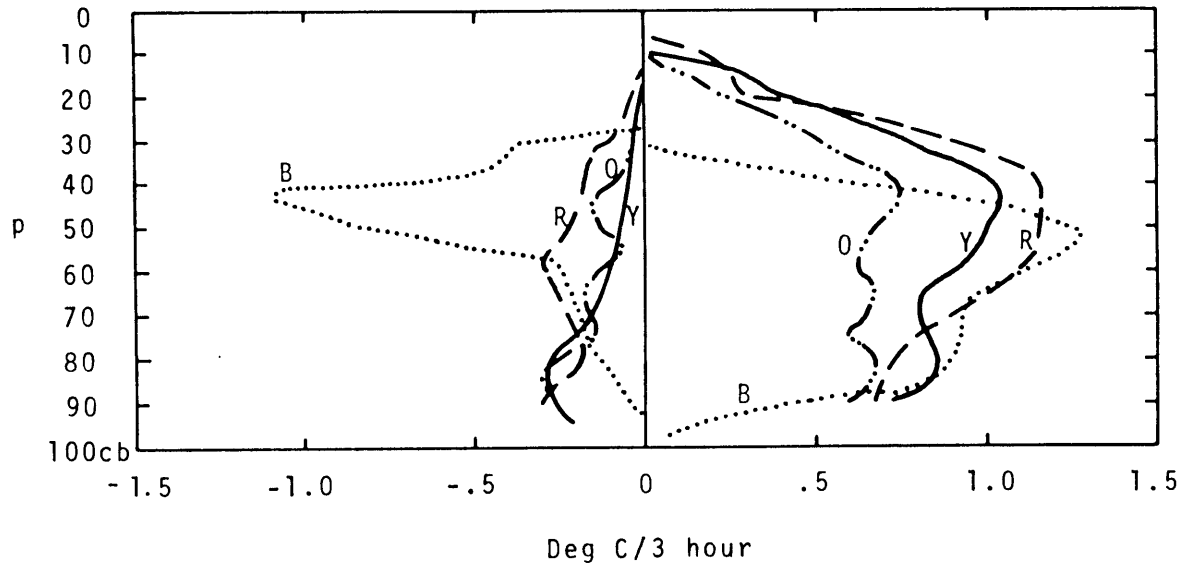


Figure 4-14. Comparison of the heating produced by convection as determined from various studies. The curves to the right of the zero line are for $C_e P^x$ or its equivalent, curves to the left are cooling by detrained liquid water. The letters adjacent to the curves refer to the studies listed in table 6. Information from Lopez (1972) is insufficient to allow construction of the L curves.

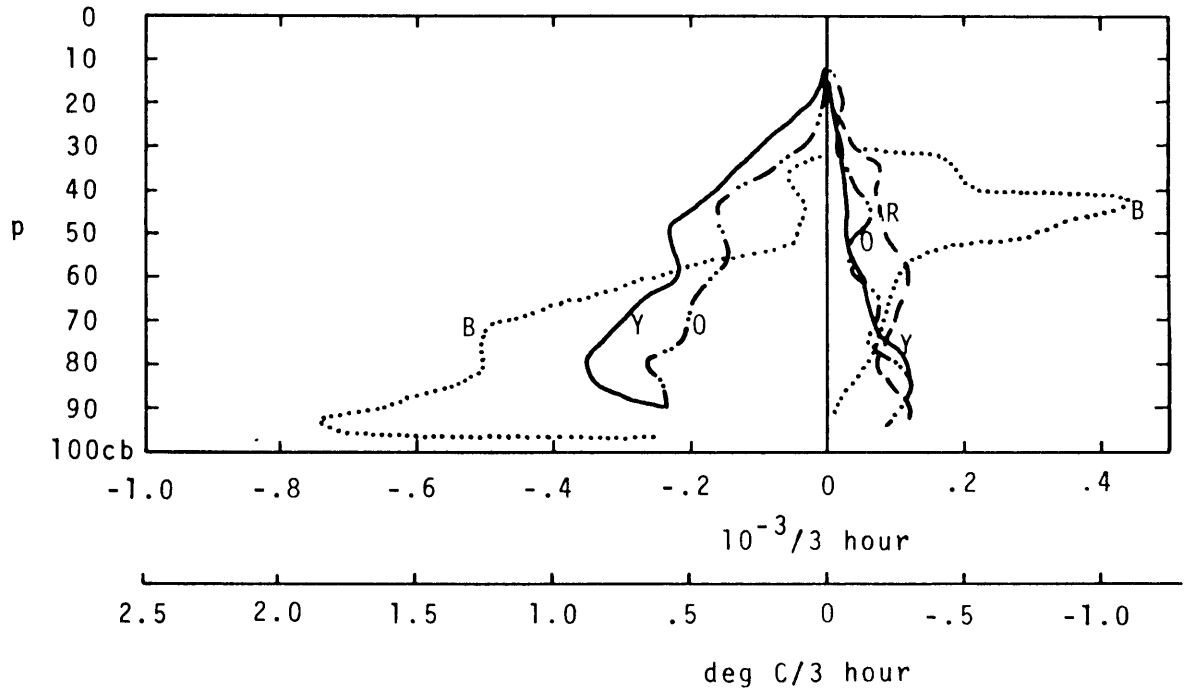


Figure 4-15. Comparison of the rates of change in large-scale water vapor produced by convection as determined from various studies. To the right of the zero line are the curves describing E_c, moistening by detrainment of liquid water; to the left is C_{vv}, the drying caused by "compensating subsidence" plus the moistening resulting from detrainment of saturated air. The letters adjacent to the curves refer to the studies listed in table 6. Information from L and R is insufficient to allow construction of their C_{vv} curves; E_c for L is also unavailable.

The spectra observed by L and computed by O have in common that there are many small clouds (tops below 75 cb) and large ones (tops above 50 cb) but relatively few in between. This accounts for the shape of the normalized M_c curves of studies L and O in figure 4-13; the large clouds appear to account for roughly half of the M_c at cloud base. Y did not compute an explicit spectrum, but their results imply a similar size distribution. The M_c computed by R is not subject to the constraints imposed by the choice of a particular cloud model. This curve cannot be rejected out of hand in spite of its being computed as a residual after the making of a few gross assumptions, particularly in inferring the downward mass flux due to evaporation.

The low-level moisture budget within the experiment N1 disturbance is dominated by near balance between large-scale moisture convergence and depletion by the cumulus. However, the observational studies suggest that much of the moisture which rises through cloud base has previously subsided between clouds. At low levels above cloud base, detrainment of water substance from the small clouds and large-scale convergence replenish the water vapor lost to the subcloud layer via "compensating subsidence." Likewise, the observed heating by $P^X C_\theta$ is partially canceled by the effects of detrainment from small clouds rather than being nullified exclusively by $-\omega\, \partial\theta/\partial p$. The major differences apparent in figures 4-14 and 15 are thus in E_c and $-(L/c_p)\, E_c$. At low levels these stem primarily from the presence or absence of small clouds; aloft the greater water content of detrained air in B is largely responsible. The largest $r_{\ell c}$ computed by L and Y doesn't exceed .001, compared with B's $r_{\ell cm}$ = .003. (No liquid water profiles are given by O.) The large

clouds observed by L, Y, and probably O are therefore more efficient than in B. When total cloud populations are considered, the inefficient small clouds cause the (table 7) efficiencies to be similar to B. The parameterizations used by L and Y to obtain r_{ec} are not of sufficiently compelling sophistication to be used as a strong argument against r_{ecm} = .003. Liquid water contents of 3 to 4 g m^{-3}, equivalent to r_{ec} of .002 to .003, are observed within active convective clouds (e.g., Kyle and Sand, 1973, Simpson and Wiggert, 1971).

4.1.3 Internal gravity waves below 50 cb

Figure 4-8 indicates that pronounced geostrophic inbalance develops on length scales of 50-100 km three hours into experiment N1. This feature, which is the direct result of minor temperature change on a similar horizontal scale, is a precursor to the emergence of spacial variations in the six hour ω-field (figure 4-4b). These are internal gravity waves, confined mainly between 50 and 100 cb and evident also in runs N0 and N2. They appear to originate close to the trough axis and propagate away from it at 12-16 m sec^{-1} with respect to the basic zonal flow. For example, in figure 4-4b, developing small-scale ascent regions are discernible at about 275 km and 500 km. By nine hours (figure 4-4c) these move to 50 km and 625 km, and at twelve hours they are barely detected at about 900 km (i.e., -100 km), and at 725 km.

After an emergence period of three to six hours, when growth is seemingly more rapid, the amplitude of the ω-variations associated with these waves increases linearly at a rate of about $\pm$ .2 x 10^{-4} cb sec^{-1} per three hours. A similar pattern of growth is observed in runs N0 and N2. There

is a slight tendency for the ascent regions to be warmer than the areas of descent, as would be expected with amplifying waves. No such smaller-scale oscillations appear in any of the dry runs; the parameterization of cumulus convection is responsible for their appearance. This does not necessarily reveal a flaw in the cumulus parameterization, for it is well known that internal gravity-wave activity in nature is frequently initiated by cumulus convection. The modest growth rate suggests that these internal waves can be suppressed by including horizontal diffusion of momentum and temperature, a practice followed in other published studies (Rosenthal, 1970, for example) employing hydrostatic primitive equations and cumulus parameterization.

Syōno and Yamasaki (1966) have investigated the linear motions possible in a three-layer model with parameterized unconditional convection heating proportional to $-\omega$ at the top of the boundary (lowest) layer. Potential temperature in the boundary layer of this model is kept identical to that in the middle layer, and the partition of the heating between the middle and top layers is made a free parameter. Syōno and Yamasaki determined that a variety of gravity wave modes are possible. Which of these should be expected in any given situation is determined by the convective heating per unit large-scale mass flux out of the boundary layer and the partitioning of this heating between the two levels above the boundary layer. If heating (cooling) by convection is sufficient to allow $\partial\theta/\partial t$ to be positive at the first level above the boundary layer when ω at top of boundary layer is negative ($\partial\theta/\partial t$ negative when ω is positive), a rapidly amplifying stationary wave is possible. With heating just above

the boundary layer insufficient to meet the above criteria, a set of amplifying propagating waves can occur if heating in the top layer is large.

Because of the greater vertical resolution in the present model an exact comparison between it and that of Syōno and Yamasaki is impossible. However, the simple vertical structure of our waves encourages us to explore further. Considering the layer between 100 and 50 cb as equivalent to Syōno and Yamasaki's three-layer vertical domain, the maximum heating by convection is in the top portion. A rough estimate of where our vertical distribution of convection heating might fit on Syōno and Yamasaki's stability diagram is that it corresponds to slow growth of the amplifying propagating waves. In view of these circumstances, we conclude that the gravity waves in our model are related to Syōno and Yamasaki's amplifying, propagating waves.

4.1.4 Large-scale cloud and precipitation

In this section we concentrate on the development of large-scale cloud and precipitation and of the consequences of this upon the motion field. Consider first figure 4-16, which is a step-by-step plot for the first three hours of ω (40 cb) and θ, r_ℓ, and r_p (each at 37.5 cb) at χ = 462.5 km. As we know from section 4.1.2, this is a location of concentrated detrainment of convective cloud air; the influence of this detrainment is dramatically evident. In spite of strong subsidence and negligible horizontal advection, θ drops by 0.2 K during the first 51 minutes of the run. (This cooling allows the maximum convective cloud top to penetrate into the 30-35 cb computational layer after one hour.) During the next time step a large-scale cloud ($r_\ell > 0$) develops and the tem-

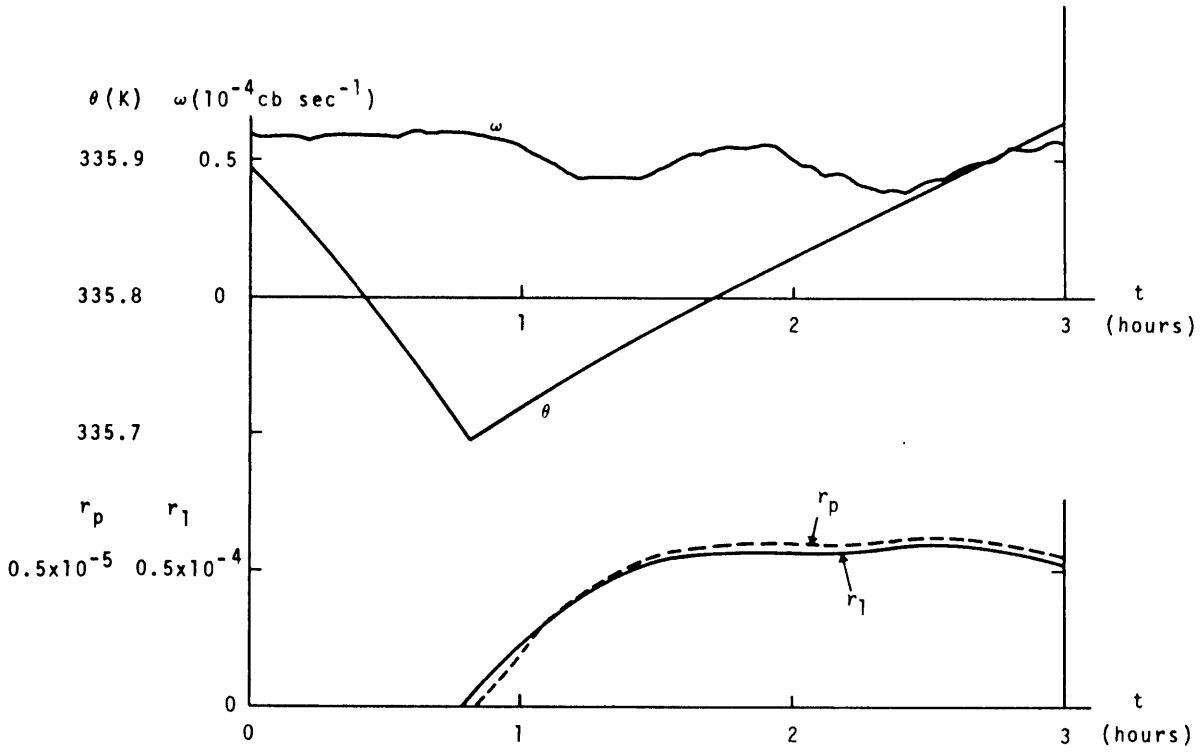


Figure 4-16. Step-by-step plots of θ, ω, r_l, and r_p, at x = 462.5 km. ω is at 40 cb, other variables at 37.5 cb.

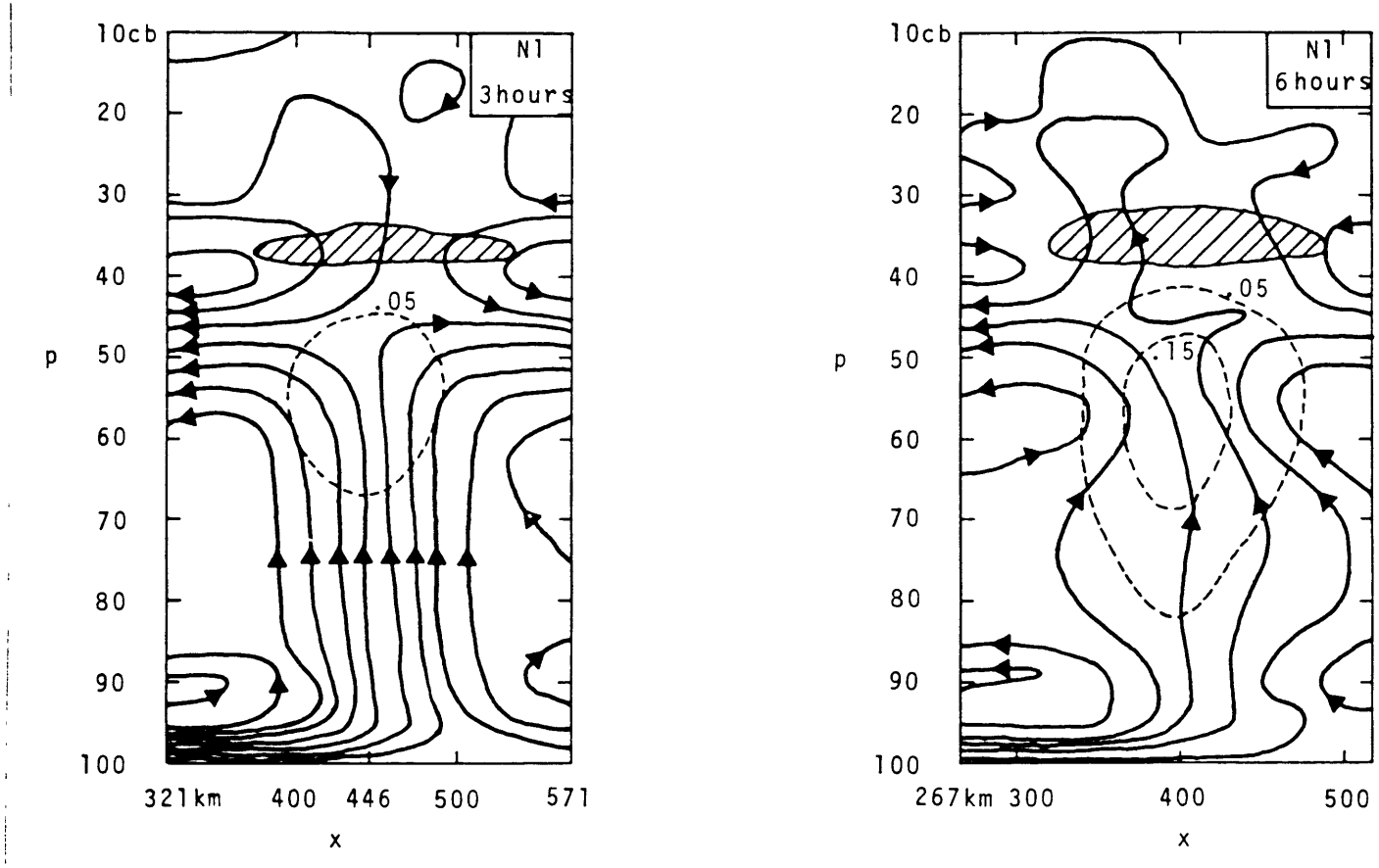
perature abruptly starts to rise. One time step later, precipitation (r_p) forms. Following this, r_ℓ increases to an equilibrium level of about 0.05×10^{-3} at which detrainment from convection balances the auto-conversion plus the large-scale cloud evaporation ($E_\ell > 0$). All the while θ is increasing steadily under the influence of net convective heating, $p^\kappa C_\theta - (L/c_p) E_c$. (Because the lapse rate is only very slightly less than moist adiabatic, large-scale subsidence is a minor contributor to the warming.) This sequence of events is typical for the 37.5 cb level in the vicinity of the trough axis. Out farther, and above and below, where the detrainment of convective cloud material is not so great and/or where the large scale is initially drier, the march of events is slower and no large-scale cloud develops. Consequently, $\theta - \hat{\theta}$ ($\hat{\theta} = \chi$ -average of θ) at three hours is slightly positive within the large-scale cloud and negative adjacent to it. Because this warming occurs within only one computational layer, the influence on the three-hour ω-field is not yet readily discernible.

The first order time discontinuity in θ derives from the assumption that all liquid water detrained from convective cloud evaporates instantaneously. With the large scale unsaturated, the top portion of a cumulonimbus will typically remain visible as a distinct entity for the order of an hour after the remainder of the cloud has dissipated. In nature we would therefore anticipate a gradual change from $\partial\theta/\partial t$ negative to positive as the large scale becomes more and more filled with cumulonimbus remains. This is not considered a serious model shortcoming because the period of a free gravity-inertia wave having dimensions of the large-scale cloud is of order one day.

Beyond three hours, evolution of the motion field continues to be described accurately by the linear terms in the momentum equations; the nonlinear advective terms are generally an order of magnitude smaller than the imbalance between Cariolis and pressure-gradient forces. Heating by convection complicates the dynamics; we are not observing simple gravity wave activity. Figure 4-17 shows large-scale cloud and streamfunction for the ageostrophic flow, got by solving $\partial\psi/\partial p = -(u-u_g)$, and $\partial\psi/\partial x = \omega$. The isolines of ψ are 2 ton sec^{-3} which translates to a mass flow of approximately .2 ton m^{-1} sec^{-1} between consecutive streamlines.

Warming within the large-scale cloud at 37.5 cb creates substantial inbalance between the Coriolis force and pressure-gradient force by six hours at 32.5 and weaker inbalance in the opposite sense at 42.5 cb as can be seen by comparing figures 4-6b and 4-10b in the vicinity of the trough axis. Consequently, ω becomes negative in the center portion of the large-scale cloud by six hours and continues to decrease through twelve hours. The center portion of large-scale cloud is about 0.4 C warmer than the surroundings during the six to nine hour period, that is after ω has become negative. During this period the net heating by convection approximately balances slow cooling by moist-adiabiatic ascent, thus providing a little extra kick to the ascent within the large-scale cloud.

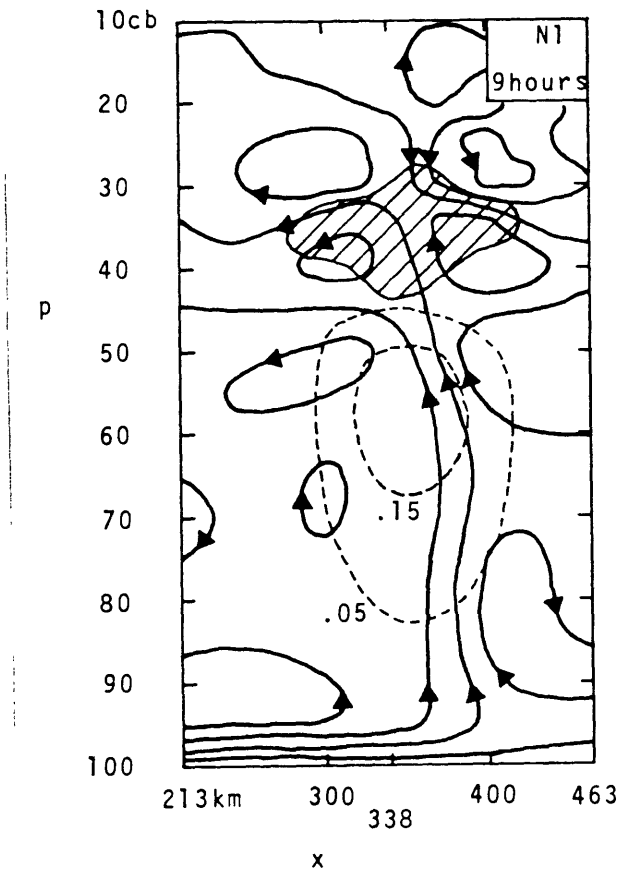
Strong descent at nine hours just above the large-scale cloud results from cooling by evaporation of detrained liquid water. At six hours, areas of descent flanking the ascent region remain from the original area of subsidence. These gradually weaken as the region of active convection continues to narrow and detrainment of liquid water decreases or vanishes altogether. The narrow region of large-scale ascent below 50 cb just east of



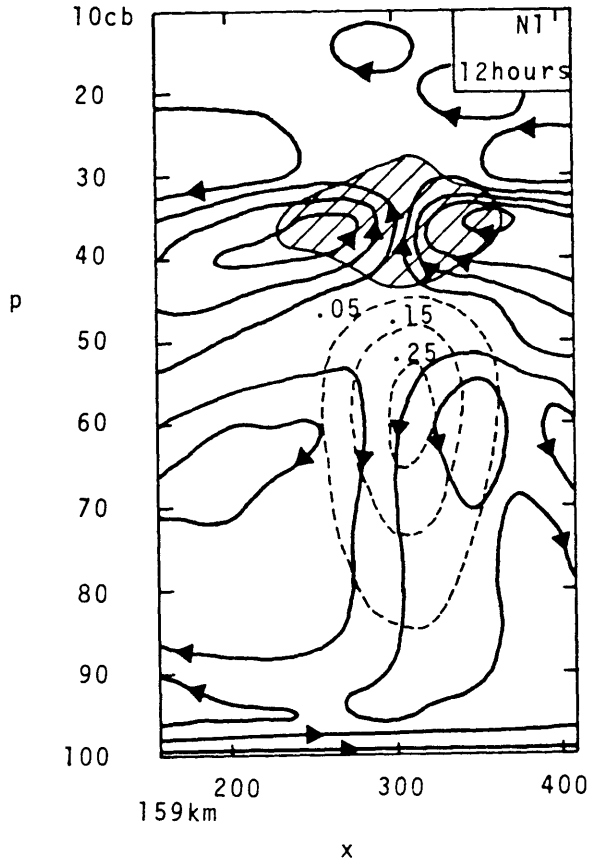
a. 3 hours

b. 6 hours

Figure 4-17. Large-scale cloud ($\zeta_z > 0$, hatched), ageostrophic streamfunction (mass flow between like-pointing streamlines: .204 ton m^{-1} sec^{-1}), and isotherms of cooling by evaporation of large-scale precipitation (dashed) during the preceding three hours, for run N1. For each time, the diagrams depect only that portion of the domain that is within 125 km of the trough-axis position, based on 5 m sec^{-1} westward movement. Isotherms of evaporation are depicted 27 km west (1.5 hours trough motion) of their true location. See table 5 for supplementary data.



c. 9 hours



d. 12 hours

Figure 4-17. (Continued)

the trough axis at nine hours has apparently become the upward motion associated with one of the internal gravity waves discussed in section 4.1.3 and by twelve hours has moved to about 450 km. The large-scale cloud is therefore "on its own" after nine hours. Because the lapse rate of temperature within the large-scale cloud becomes very slightly greater than the moist adiabatic after nine hours (probably due to evaporation of detrained liquid water above the large-scale cloud) we observe the vertical motion to continue increasing. In summary, the large-scale subsidence, driven by convective cloud detrainment and associated with large-scale evaporation, evolves into large-scale ascent in which condensation is the primary heating mechanism. This can also be seen from the trend in the domain integral of E_ℓ during the N1 computation (figure 4-5).

Convective activity never becomes sufficiently intense to discharge large amounts of liquid water into the upper troposphere; large-scale condensation is responsible for the maximum liquid water concentration of $.086 \times 10^{-3}$ and the largest three-hourly rainfall of .06 mm observed during the entire run (table 5). Although the vertical motion in the large-scale cloud becomes about 6 cm sec^{-1} by twelve hours, the amount of water vapor available at 35 cb is too small for the large-scale circulation to be directly responsible for substantial precipitation. The precipitation process is dominated by autoconversion because of the small η_ℓ . Collection of cloud drops by rain, A_c , never becomes more than about 5% of A_v at any point.

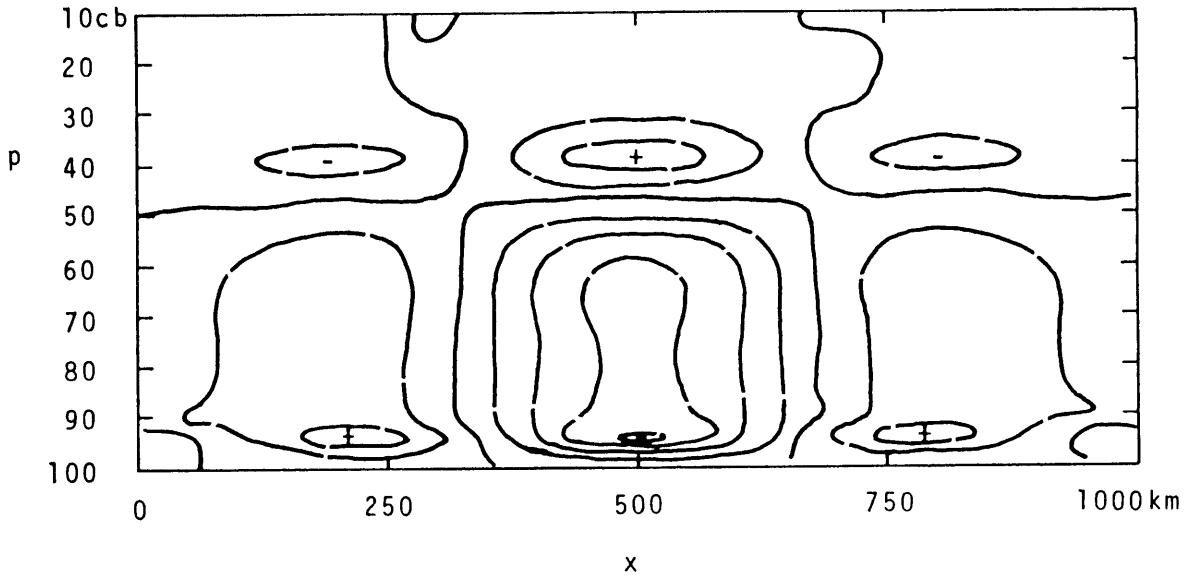
Cooling by precipitation evaporation, depicted on figure 4-17, is typically about an order of magnitude smaller than the convective heating terms in (2.5) during the first six hours. Consequently, precipitation

evaporation cannot be responsible for the weakening of the initial disturbance. Nine- to twelve-hour evaporation cooling at (337.5 km, 57.5 cb) of 0.3 C is the largest observed at any point during experiment N1, and for this period is comparable to the convection-heating terms in this grid-column. The coincidence of the sinking motion with maximum evaporational cooling on figure 4-17d argues for this subsidence being the result of evaporation. Comparison of the ω- field of experiment N1 with those of experiments N0 and N2 suggests that this evaporation is sufficient near the trough axis to disrupt the low and middle tropospheric gravity waves discussed in section 4.1.3. We conclude that precipitation evaporation is of slight significance during the last few hours of the run.

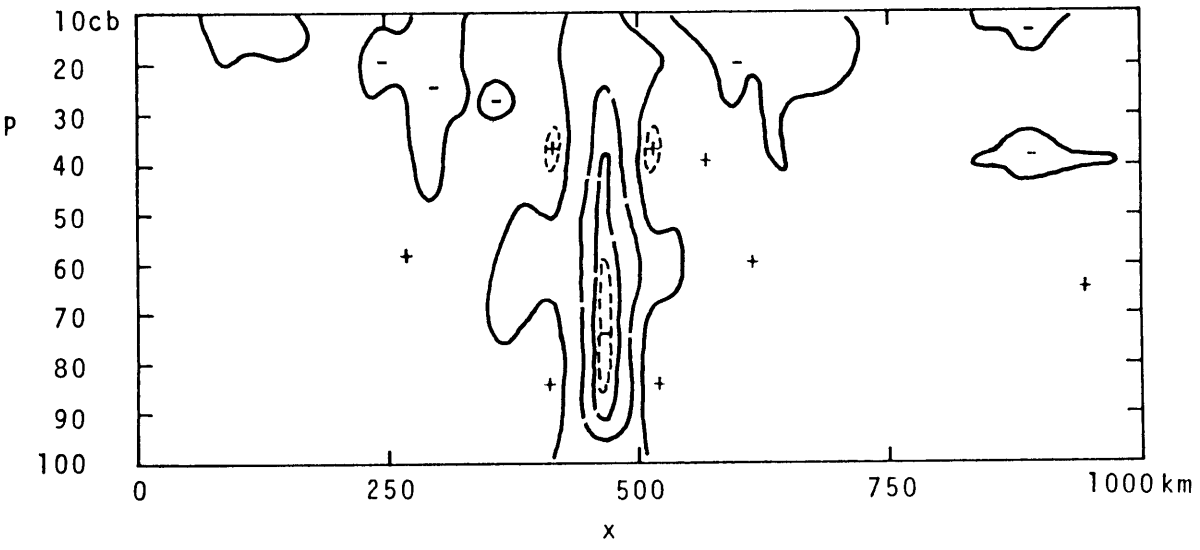
4.2 Experiment N3: $\beta = 1.5$

Experiment N3 is motivated by the comparisons made in section 4.1.2 suggesting that M_c should be assumed greater than $\bar{M}$ at 90 cb (i.e., β should be greater than one). N3 is in all respects similar to N1, save that $\beta = 1.5$ (see table 4), thus it constitutes an unambiguous test of the importance of β. Run N3's history can be conveniently split into two stages: for about the first three hours, very rapid amplification (in terms of ω) and narrowing of the trough, then breakup of the main ascent region followed by gradually increasing confusion. The run terminated at 6 hours 57 minutes when θ at 97.5 cb dropped below 291 K.

The initial ω-field is presented in figure 4-18. At the trough axis the heating component of this field is about four times its counterpart in N1. The frictionally forced component of this ω is about 15% of the total in the trough. From figure 4-19 we see that in the boundary layer,



a. Initial. Contour interval: 10^{-4} cb sec^{-1}. Maximum ω = 2.65 x 10^{-4} cb sec^{-1} at (500 km, 40 cb), minimum ω = -4.07 x 10^{-4} at (500 km, 95 cb).



b. 3 hours. Contour interval: 10 x 10^{-4} cb sec^{-1}. Maximum ω = 6.21 x 10^{-4} cb sec^{-1} at (512 km, 40 cb), minimum ω = -26.22 x 10^{-4} cb sec^{-1} at (462.5 km, 80 cb).

Figure 4-18. ω during experiment N3. Solid lines are the zero isopleths.

with respect to a coordinate system moving westward with the trough at 5 m sec^{-1}, the local change of u, its advection, and the x-component of friction are all large by comparison to the difference (which is the same as in experiment N1, figure 4-8) between the x-components of the Coriolis and pressure-gradient forces.

Referring to equation (4.3), we note that the effect of setting $\beta = 1.5$ is to warm the trough between 95 and 55 cb [the upper limit of validity of (4.3)], commencing at the initial time. Furthermore, since the warming along the trough axis is greater than the subsidence warming outside the disturbance, at low levels the pressure-gradient force directed toward the trough overcomes the opposition of the Coriolis force and at 87.5 and 92.5 cb acts in concert with friction to accelerate the large-scale inflow. At 97.5 cb the inflow is retarded by friction so that ω at 95 cb increases much less rapidly than above. This deepening mechanism is the "allobaric" effect discussed by Syōno and Yamasaki (1966) and Bates (1973). In the boundary layer the nonlinear advection of x-momentum performs much the same function as in experiment N1 in that it tends to concentrate the low-level convergence at the trough.

In contrast to the situation in run N1 the nonlinear advection and the geostrophic inbalance <u>both</u> intensify the upward motion. The three-hour portrayal of the terms in the x-momentum equation (figure 4-19) indicates that nonlinear advection has become dominant as the horizontal scale decreases and the vertical circulation increases. However, by three hours precipitation evaporation has reversed the sense of the geostrophic imbalance in the immediate vicinity of the strongest ascent.

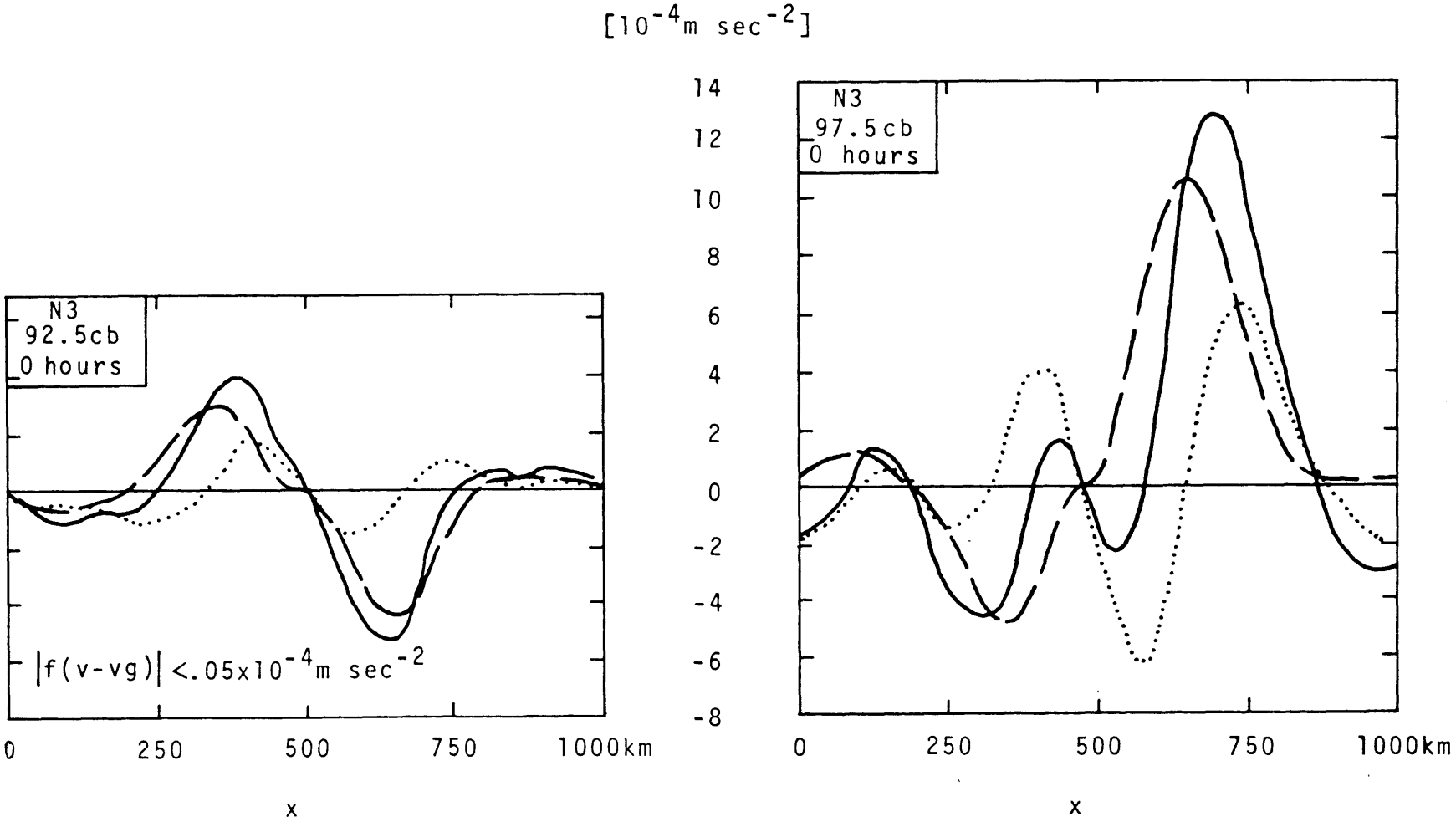


Figure 4-19. As figure 4-8, experiment N3.

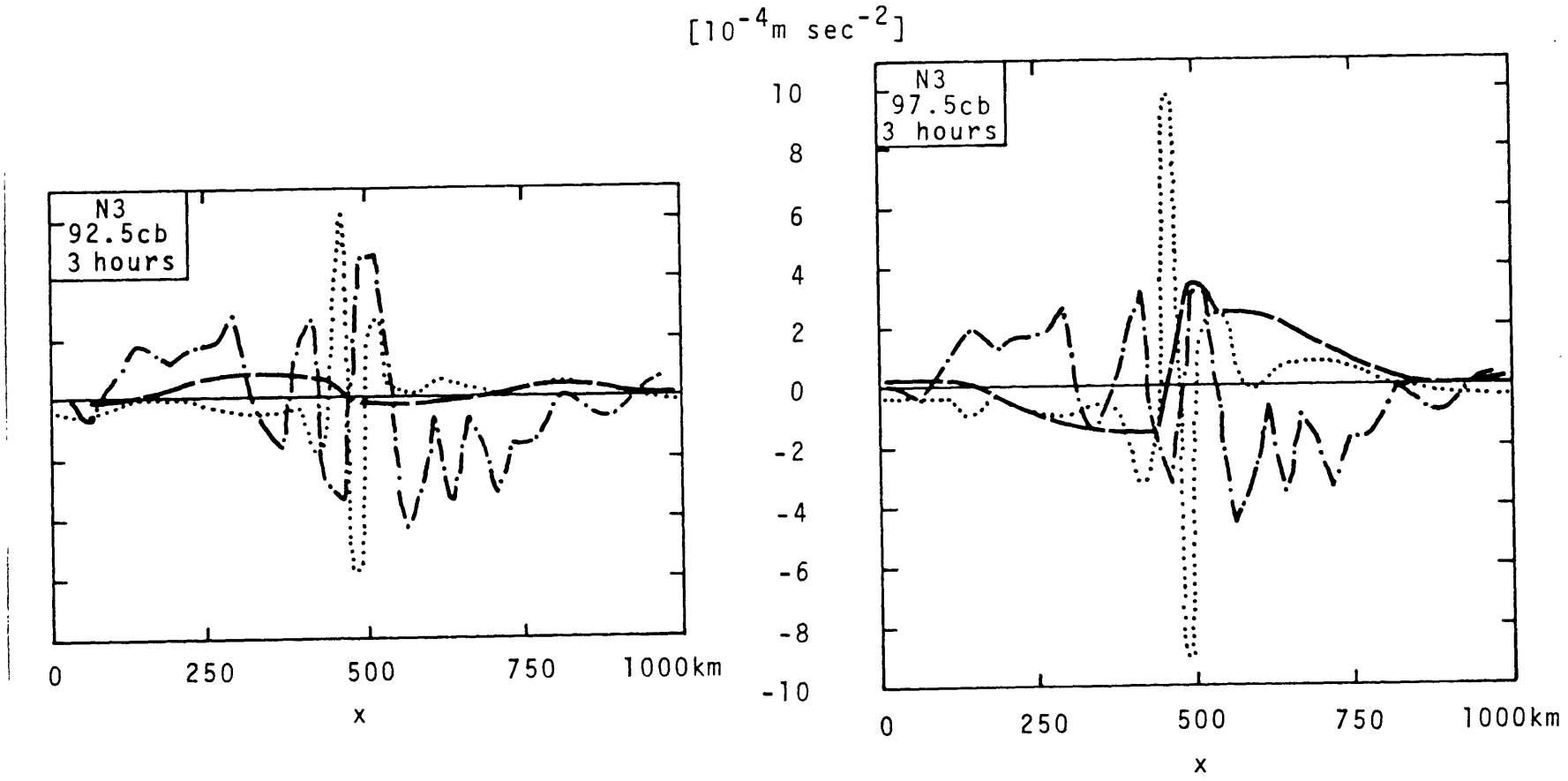


Figure 4-19. (Continued)

Figure 4-18b shows the tremendous strengthening and concentration that takes place in the vertical circulation. Maximum vertical velocities are close to 30 cm sec^{-1}, and, in spite of the narrowing of the ascent region from about 350 km initially to 75 km at three hours, large-scale upward mass flux also increases at all levels except 95 cb. For example, the upward mass flux through 90 cb is 10.1 ton m^{-1} sec^{-1} at three hours, an increase of 27% from the initial flux; greater percentage increases are observed above. By contrast the corresponding mass flux in N1 is only 76% of its initial value. The magnitude of the large-scale vertical motion implies that the fractional area occupied by convective clouds, γ, is appreciable. Indeed, using (2.16) with the maximum upward motion at 90 cb gives γ = .34. That this may have serious consequences for the accuracy of the N3 computations is apparent from the discussion in Appendix C.

The more intense convection in this run results in large-scale cloud formation at 37.5 cb by 12 minutes, and 15 minutes later this cloud has a larger liquid water content than that of experiment N1 ever possesses. Subsidence within this cloud diminishes rapidly after 30 minutes, and ascent appears in the central portion by 1 hour 15 minutes. The mixing ratio of large-scale cloud, r_ℓ, achieves a maximum of 1.1 x 10^{-3} ($\approx$ .4 g m^{-3}) at 27.5 cb by three hours.

Significant large-scale precipitation is produced by this cloud. Because r_ℓ is large, collection of cloud water by raindrops, A_c, contributes 20% of the precipitation during the first three hours. I estimate that half of the large-scale precipitation evaporation during the first three hours occurs within the last 30 minutes. The greatest large-scale rainfall accumulation at p_∞ during the first three hours is a mere

0.3 mm at 462.5 km. Only about 13% of the large-scale precipitation which forms during this period reaches P_{00} ; most of the remainder evaporates. Maximum cumulus rainfall is respectable -- 13.6 mm falls at 462.5 km during the first three hours.

The heat budget for the first three hours in the gridcolumn centered at 462.5 km, figure 4-20, shows that the various heating terms, except for $-(L/c_p)\,E_l$, have much the same general shape as during the corresponding period of experiment N1. All terms are about an order of magnitude larger. Comparing the net three-hour change to the "mean" curve we see that the disturbance has developed a warm core at low levels and in the upper troposphere. We have discussed formation of the low-level warm core previously. The warmth at high levels is due to net convection heating under saturated conditions with a lapse rate only slightly less steep than the moist adiabatic. Between 80 and 60 cb the disturbance is distinctly cold-core. Large-scale precipitation evaporation is probably responsible. As mentioned earlier, there is reason to believe that in this layer $\partial\theta/\partial t > \partial\hat{\theta}/\partial t$ initially, and that most of the relative cooling occurs after two hours. The step-by-step time series of θ at (462.5 km, 87.5 cb) shows that warming stops at about 2 hours 30 minutes, that is, when large-scale precipitation evaporation becomes sufficient to nullify the warming by convection. By three hours the evaporation cooling has created a lower troposphere "mesohigh" just east of the trough axis. It does not closely resemble a classic thunderstorm high which has greatest intensity at the surface, but its influence does reach into the boundary layer, as witnessed by the plots of $f(v-v_g)$ on figure 4-19.

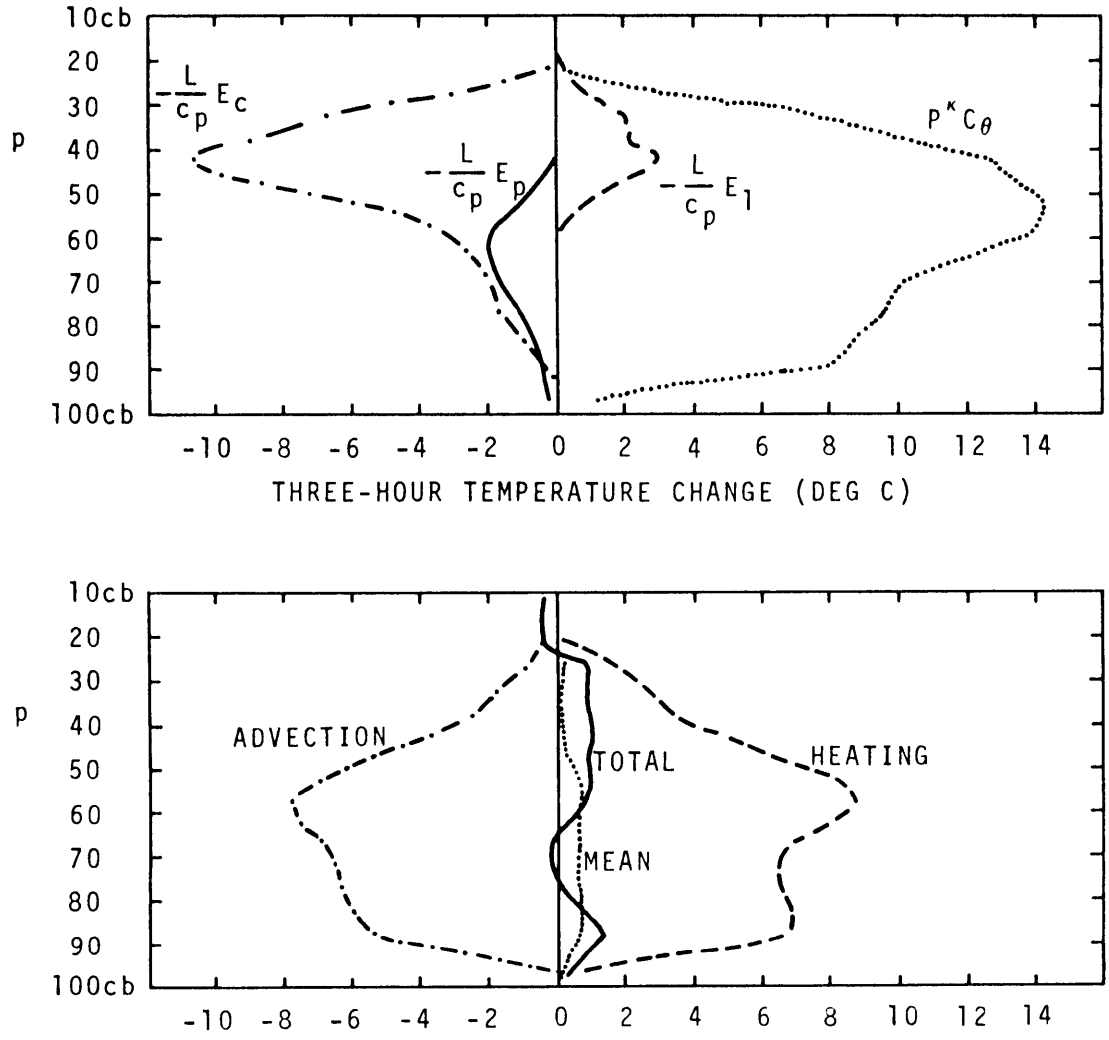


Figure 4-20. As figure 4-11, experiment N3.

At three hours the stage is thus becoming set for the weakening and breakup of the main ascent region. Because of my programming error the large-scale fields were not printed out as intended at six hours. Beyond three hours a reliable diagnosis of the processes that led to the early termination of the run is impossible. It does appear from a few trajectories that are available that the concentrated large-scale ascent along the trough axis reaches its peak strength soon after three hours and then rapidly reverses direction, most likely as a result of large-scale precipitation evaporation. The large-scale cloud above, however, maintains its identity. Soon after three hours vertical motion variability of short horizontal wavelength appears away from the trough axis and by six hours has spread throughout the domain. The amplitude and structure of these variations and whether or not they are related to waves discussed by Syōno and Yamasaki (1966) are not known.

We have already noted that the "allobaric" process is an important contributor to the amplification in this run. Figure 4-19 shows that friction is clearly acting to retard the inflow in the 90-100 cb layer. Thus, excluding nonlinearities, this system is dynamically analogous to the rapidly amplifying gravity waves discussed by Syōno and Yamasaki (1966) which occur if, at the top of the boundary layer, $\partial\theta/\partial t$ is positive where ω is negative (see section 4.1.3, above). We observe an e-folding time for ω of roughly 90 minutes. Bates (1973) determined that for e-folding times less than $\sqrt{3}/f$ the "allobaric convergence" is opposed by friction, as in run N3.

There are a number of shortcomings of the model which are revealed by this run. The disturbance becomes so narrow by three hours that one is

inclined not to put too much confidence in the results after this time because of space truncation error in the finite differences. The lack of a cloud size spectrum and the consequent minimum of detrainment of low levels together with $\beta = 1.5$ is responsible for spurious drying below 90 cb. This is particularly evident with the 90-95 cb computational layer where moist air is selectively removed by the convection and replaced by drier air subsiding from above. The drying is to an extent self-limiting. Sufficient drying will cause the LCL of air at 97.5 cb, which determines cloud base pressure (section 2.3.1), to become well above 90 cb, where the lapse rate of temperature is less favorable for convection development.

One may well question the realism of the development which occurs in this computation. Unfortunately, paucity of knowledge concerning observed tropical mesoscale systems precludes a sure judgment. Mesoscale blowups of convective activity are commonly observed via satellite in convectively active regions of the tropics but the dynamics remain obscure. The constraint of $\partial/\partial y = 0$ is also a consideration here; if experiment N3 had been carried out in a cylindrical domain one suspects that a tropical storm would have tried to form.

4.3 Conclusions from no-shear computations

Our principal conclusion is that, without vertical shear of the zonal wind, $\beta > 1$ is a necessary condition for intensification of the initial disturbance. This is in agreement with the analytic results of Israeli and Sarachik (1973). Basing their argument upon Arakawa's "quasi-equilibrium assumption" relating cumulus activity to the large-scale (Arakawa and Schubert, 1974), they determined that a necessary condition for growth of

an infinitesimal perturbation is that $M_c > \bar{M}$ at cloud base. [In our model, $\bar{M}(p_c) \approx \bar{M}(p_{cb})$]. We have not attempted to determine whether or not the Arakawa quasi-equilibrium assumption would imply $\beta > 1$ in our model.

We have seen that the observational studies are unanimous in indicating $\beta > 1$, although this result must be considered preliminary because of the averaging procedures used. It is not known to what extent the studies of Yanai et al. (1973), and Ogura and Cho (1973) best describe deepening or non-deepening situations, but they indicate, as does López (1972) for non-developing ("conservative") cloud clusters, that the warming by "compensating subsidence" is ameliorated by liquid water detrainment and evaporation from small clouds (figure 4-14), a consideration ignored by Israeli and Sarachik. Therefore, when convection is parameterized in terms of a one-dimensional cloud model with no downdrafts and when a spectrum of cloud sizes is allowed, deepening depends on not only M_c as compared with $\bar{M}$, but also upon this size spectrum.

We are now in a position to explain why in this model the stability of the large-scale wave disturbance is so sensitive to the disposable parameter, β. With respect to the moving wave disturbance in experiments N1 and N2, $\partial\bar{\theta}/\partial t \approx 0$ in the trough and is positive in the ridge at 92.5 and 87.5 cb. During the early hours of experiment N3, there is warming at both ridge and trough, but the warming at the trough axis is greater than in the ridge. On the basis of this evidence we suggest the following stability criterion appropriate to this model for amplification of convectively driven disturbances: β such that at 87.5 and 92.5 cb the trough warms more rapidly than the ridge. Applying (4.3) to both trough and ridge, ignoring

$-(u-u_g)\,\partial\bar{\theta}/\partial x$, and noting that at 87.5 and 92.5 cb, $M_c \approx M_c(p_c)$, and that $\partial\bar{\theta}/\partial p$ is approximately uniform in x, the stability criterion reduces to the following condition: β such that

$$(\beta-1)\,\bar{\omega}(90\,cb)\Big|_{\substack{\text{trough}\\ \text{axis}}} + \bar{\omega}(90\,cb)\Big|_{\text{ridge}} < 0.$$

For experiment N1 the expression on the left hand side is about $.6 \times 10^{-4}$ cb sec^{-1}; the initial ω-field of experiment N3 yields -0.5 to -1.0×10^{-4} cb sec^{-1}, depending on the choice of $\bar{\omega}$ in the ridge. We therefore suggest $\beta \approx$ 1.25 as the marginal stability value corresponding to the neutral Ekman initialization. No experiment with this value for β has been made, although shear computations with β = 1.35, to be reported on in the next chapter, do show some amplification. Neither have additional computations been carried out incorporating boundary layer stratification in the initialization as in experiment N2. However, we see no reason to doubt that the foregoing remarks are applicable.

This sensitivity of the model to the rate of heating in the low levels is also a feature of older models designed for the study of CISK which do not use explicit cloud dynamics as the basis for the vertical partitioning of convection heating, but which also relate convective activity to a low-level, large-scale vertical moisture flux (e.g., Syōno and Yamasaki, 1966, Yamasaki, 1968). Moreover, Geisler's (1972) quasi-geostrophic diagnostic study indicates that for relatively short wavelength disturbances such as we are discussing the response of the low-level vorticity field (and, by implication, upward mass flux) to heating is large only if this heating

extends down to low levels. The widely-used Kuo (1965) parameterization scheme makes the rate of convection heating at any level proportional to $T_c - \bar{T}$, where T_c is the cloud temperature, equal to the temperature of the moist adiabat corresponding to conditions at cloud base. The result is that most of the heating by convection is confined to the middle and upper troposphere. Moreover, there is not the potential for the positive feedback loop observed in experment N3; if warming should occur at low levels, $T_c - \bar{T}$ becomes smaller, decreasing the heating rate. To the author's knowledge, no computation employing the Kuo scheme has produced a growth rate as large as that observed during N3. From the foregoing we conclude also that deepening would not have occurred had run N1 ($\beta = 1$) been repeated with r_{lcm} set to zero. We anticipate that the main difference would be found above 50 cb, where detrainment of liquid water would be absent.

Comparison of runs N1, N2 and N3 shows clearly that even for r_{lcm} as large as .003, $\beta > 1$ is a prerequisite for the formation of a dense large-scale cloud. Otherwise, the convection is insufficiently vigorous to discharge large amounts of liquid water into the upper troposphere, and the large-scale vertical motion which develops is too weak to bring about sufficient large-scale condensation. In all runs we observe initial descent in the concentrated detrainment layer above 50 cb to reverse sign after the large-scale cloud forms. This occurs because E_c decreases sharply at the moment of large-scale cloud formation so that within the cloud net cooling by convection becomes net heating. Once ascent begins, the large-scale cloud is augmented by large-scale condensation. The largest r_l occurs during this phase in both experiments N1 and N3.

Precipitation evaporation appears to have been responsible for breakup of the large-scale disturbance in N3, in contrast to the almost negligible effect observed in N1 and N2. The reasons for this difference are that the large-scale cloud becomes denser and thicker, and the tendency for the evaporative cooling to occur at lower levels, and thereby to attack the most vulnerable portion of the disturbance. For example, the maximum evaporation cooling observed at 87.5 and 92.5 cb in the first three hours of experiment N3 is about 25 times the maximum three-hour cooling at those levels during experiment N1, whereas the evaporation integrated from the base of the large-scale cloud to p_∞ is only about eight times as large in experiment N3. The heavier rainfall rates are responsible for this; from equation (2.23), the fractional rate of evaporation is larger for smaller values of r_p . Thus, a much larger r_p is available for evaporation at low levels in N3 than in N1.

5. NUMERICAL MODEL RESULTS: CASES WITH VERTICAL SHEAR OF THE ZONAL GEOSTROPHIC WIND

5.1 Free parameters and initial conditions

In this chapter we discuss results of computations in which shear of the zonal geostrophic wind is present. The main emphasis is upon the efficacy of large-scale precipitation evaporation in establishing a large-scale downdraft. We choose the initial conditions and free parameters with the aim of maximizing the precipitation evaporation while otherwise keeping the flow as simple as possible.

There are two time scales inherent to the evaporation problem. The first, τ_s, equals $L/$[zonal wind in concentrated detrainment layer minus zonal phase speed of disturbance ascent region], where L = width of disturbance ascent region. An air parcel moves from the upshear end to the downshear end of the concentrated detrainment layer in time τ_s. The second, τ_A, is the time scale of the cloud microphysics. If A_c, the rate of collection of cloud water by precipitation, is much less than the autoconversion rate, A_u, $\tau_A \approx 1/a$, where a is the autoconversion coefficient. Otherwise, it is effectively reduced. The ratio, τ_s/τ_A, determines where with respect to the convection the large-scale precipitation will fall. This ratio is infinite for all no-shear runs, and we have seen that evaporation is superposed upon the large-scale ascent, tending rather to weaken it than to establish a separate area of descent. For a sufficiently small τ_s/τ_A (that is, either very strong shear or small a), the bulk of the large-scale cloud material is carried away from the large-scale ascent region before falling out as precipi-

tation. Furthermore, for a given large-scale ω at 90 cb, and ignoring lateral variation in $r_s - r_w$, we should expect the largest rate of precipitation, hence, evaporation to be associated with infinite τ_s/τ_A, and small values of τ_s/τ_A to result in widespread, light precipitation and, consequently, less evaporation. To make these ideas quantitative we assume a steady state disturbance of width L moving at u_g at 90 cb. Taking $x = 0$ at the upshear end of the disturbance, we assume that the rate of liquid water production is uniform in x over the interval $[0, L]$. We arbitrarily choose to maximize the precipitation in the interval $[L/2, 3L/2]$, thus striking a compromise between the two extremes mentioned above. For maximum precipitation, $\tau_s/\tau_A \approx 3.2$. When this analysis was performed we had only runs N1 and N2 to go on; we chose an L of 200 km and concentrated detrainment layer centered at 45 cb. Assuming that u equals u_g at 45 cb, and that $A_c << A_u$, the combination $\partial\theta/\partial y = -1.2 \times 10^{-6}$ K m^{-1} and $a = .1389 \times 10^{-3}$ sec^{-1} (τ_A = 2 hours) yields $\tau_s/\tau_A \approx 3.2$.

The foregoing is based on the premise that the large-scale anvil[1] cloud is "dead," that is, that large-scale condensation is not a significant source of additional liquid water. As we shall see, this premise is invalid, especially after the first few hours of anvil life, and therefore the above analysis has limited applicability. We do, however, make reference to τ_s/τ_A in judging whether or not the optimum evaporation influence is achieved in any given run.

---

[1] Following Zipser (1969) we broaden the traditional definition of "anvil" to include, as on figure 1-2, a widespread, dense, and precipitating middle and high cloud layer of cumulonimbus origin. Accordingly, we refer to the model large-scale cloud as an anvil.

The north-south temperature gradient, $\partial\theta/\partial y$, is the same in all shear runs. The zonal geostrophic wind, shown in figure 5-1, has u_g = -5 m sec^{-1} at 97.5 cb, the no-shear value. Because of the strong flow aloft, it is necessary to take Δt = 90 sec in all shear computations. Temperature is uniform in x, and its vertical variation is that portrayed on figure 3-1a. The initial v is identical to that depicted on figure 4-1 above 85 cb; below, there are minor differences because the vertical shear is taken into account in the generalized Ekman initialization of the boundary layer. Likewise, the field of $\underline{\phi} - \hat{\phi}$ is identical to that of the no-shear runs, that is, with isopleths vertical and a range of $\pm$ 20 m^2 sec^{-2}. The initial ω includes the effects of both friction and baroclinicity in addition to heating. Initialization of the boundary layer is by strategy three, section 3.2.1. Figure 5-2 illustrates the contributions to initial ω by friction and by baroclinicity at various levels. The amplitude of the friction component alone is revealed by ω at 500 km; the amplitude of the baroclinic component is apparent at 250 and 750 km.

Table 8 lists the assigned values of each varied parameter for each shear computation. The purpose of runs S5 and S6 is to enable us to evaluate other computations in light of more plausible values of r_{ecm} and a. An r_{ecm} of .006 is equivalent to a liquid water content of 3 to 4 g m^{-3} at cloud top, typical of vigorous, growing cumulus over south Florida, according to Simpson and Wiggert (1971). The catch is that much of this water is in the form of precipitation-size drops which fall out rather than participating in lateral detrainment. Cloud liquid water content is generally less than 2 g m^{-3} at the 45-50 cb level. Furthermore, liquid water measurements of $\sim$1 g m^{-3} in "inactive cloud matter at the

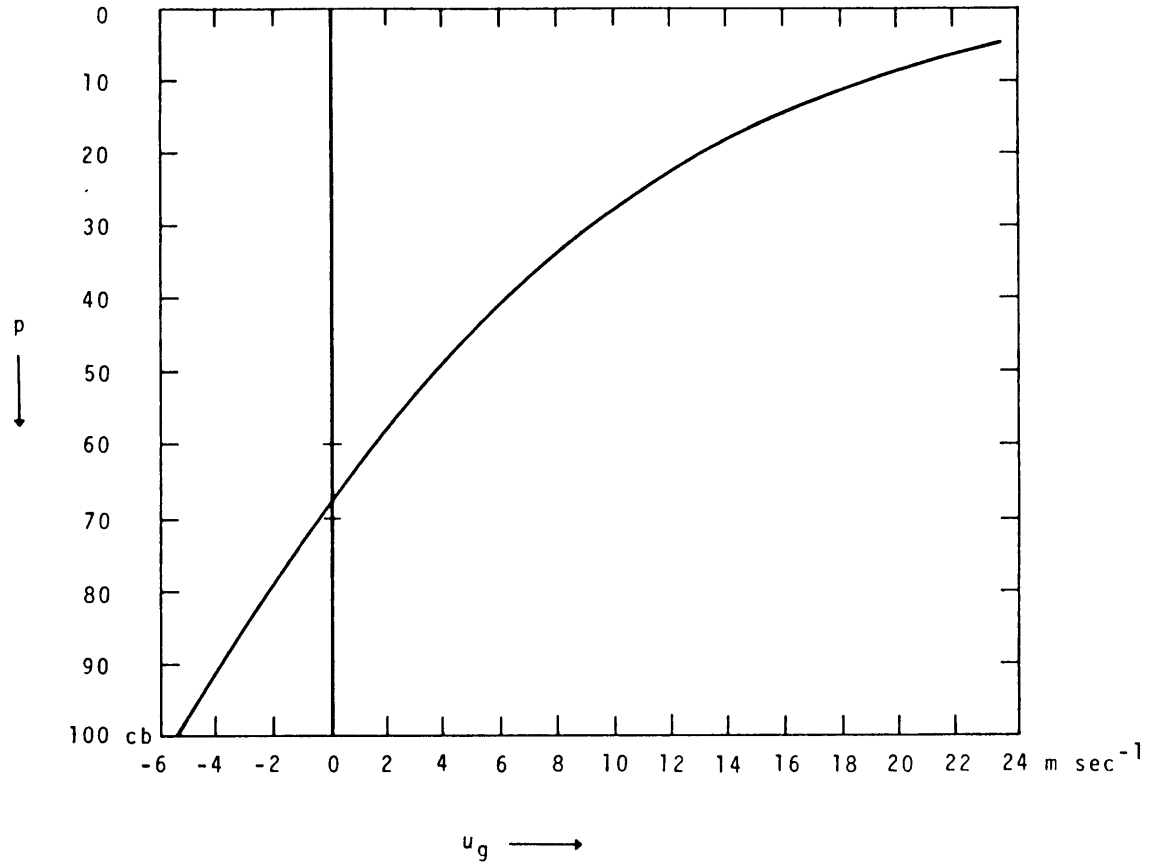


Figure 5-1. Zonal geostrophic wind, shear experiments. This profile corresponds to $\partial\theta/\partial y = -1.2 \times 10^{-6}$ K m^{-1}.

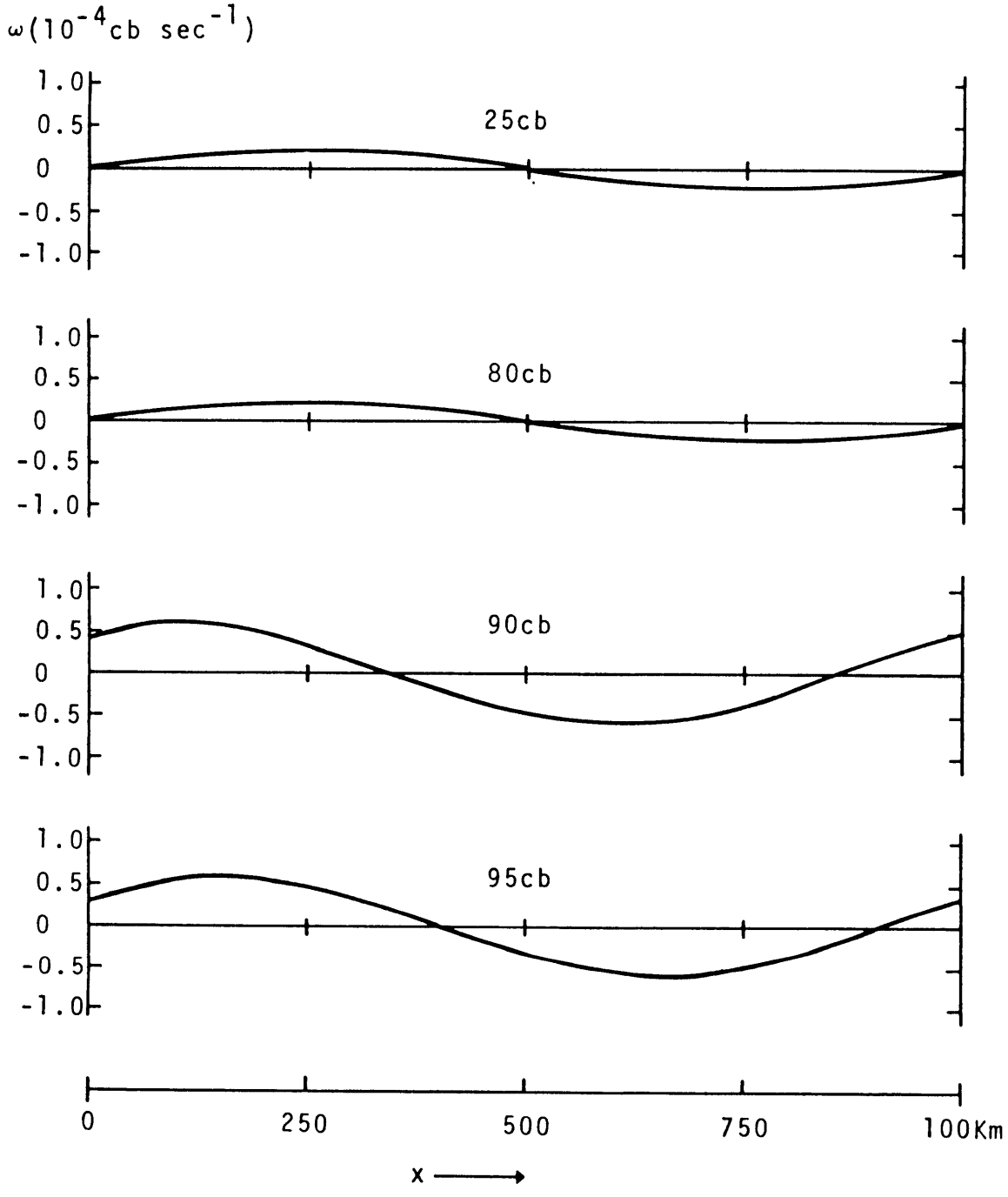


Figure 5-2. Initial frictional plus baroclinic ω at various levels, shear computations.

Table 8. Free parameter values in shear runs

Run number	Duration of run	Output interval	Ratio of upward mass flux through cloud base to large-scale mass flux at 90 cb, β	Autoconversion coefficient, a	Maximum convective cloud water mixing ratio, r_{cm}	Precipitation evaporation included?
S1	9	3	1.35	$.1389 \times 10^{-3}$	.006	YES
S2	6	3	1.35	$.1389 \times 10^{-3}$	.006	NO
S3	12	3	1.00	$.1389 \times 10^{-3}$	.006	YES
S4	12	3	1.00	$.1389 \times 10^{-3}$	.006	NO
S5	12	3	1.00	$.1389 \times 10^{-3}$	.002	YES
S6	9	3	1.00	$.5556 \times 10^{-3}$	.006	YES

periphery of the updraft" are reported by the same authors. This last, equivalent to $r_{\ell c} \sim .002$, seems most relevant to the choice of $r_{\ell cm}$ because cloud air which is detrained is, by definition, inactive cloud. We further conclude that a choice of $r_{\ell cm}$ greater than .003 is unreasonable. In view of the parsimonious precipitation from the N1 anvil (run N3 had not been performed at this point), we chose $r_{\ell cm}$ = .006 in order to maximize anvil development. That we did so is evidenced by the precipitation efficiency of convection (section 4.1.2 definition) of 2% to 4%.

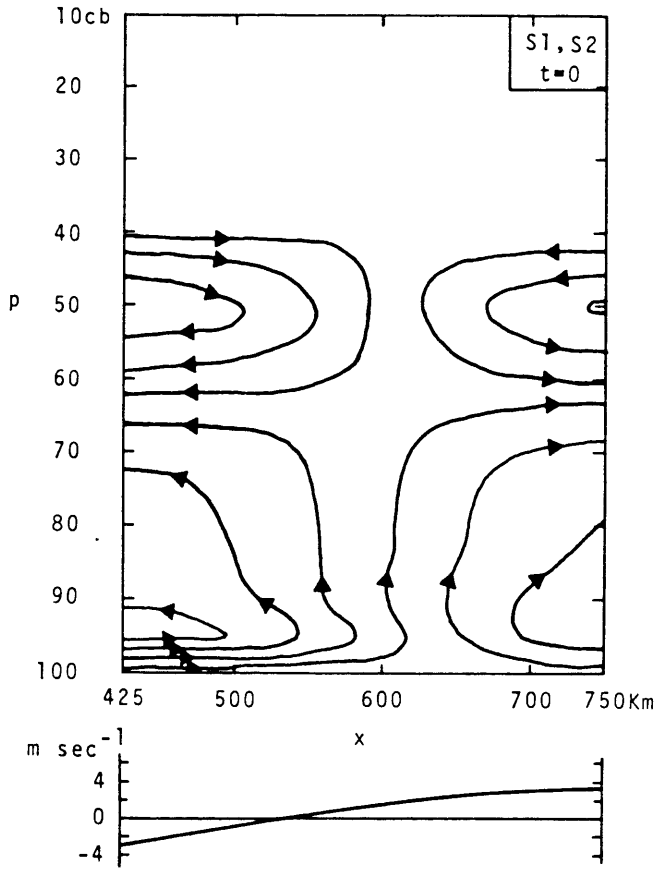
5.2 Runs with and without large-scale precipitation evaporation: $\epsilon = 1.35$

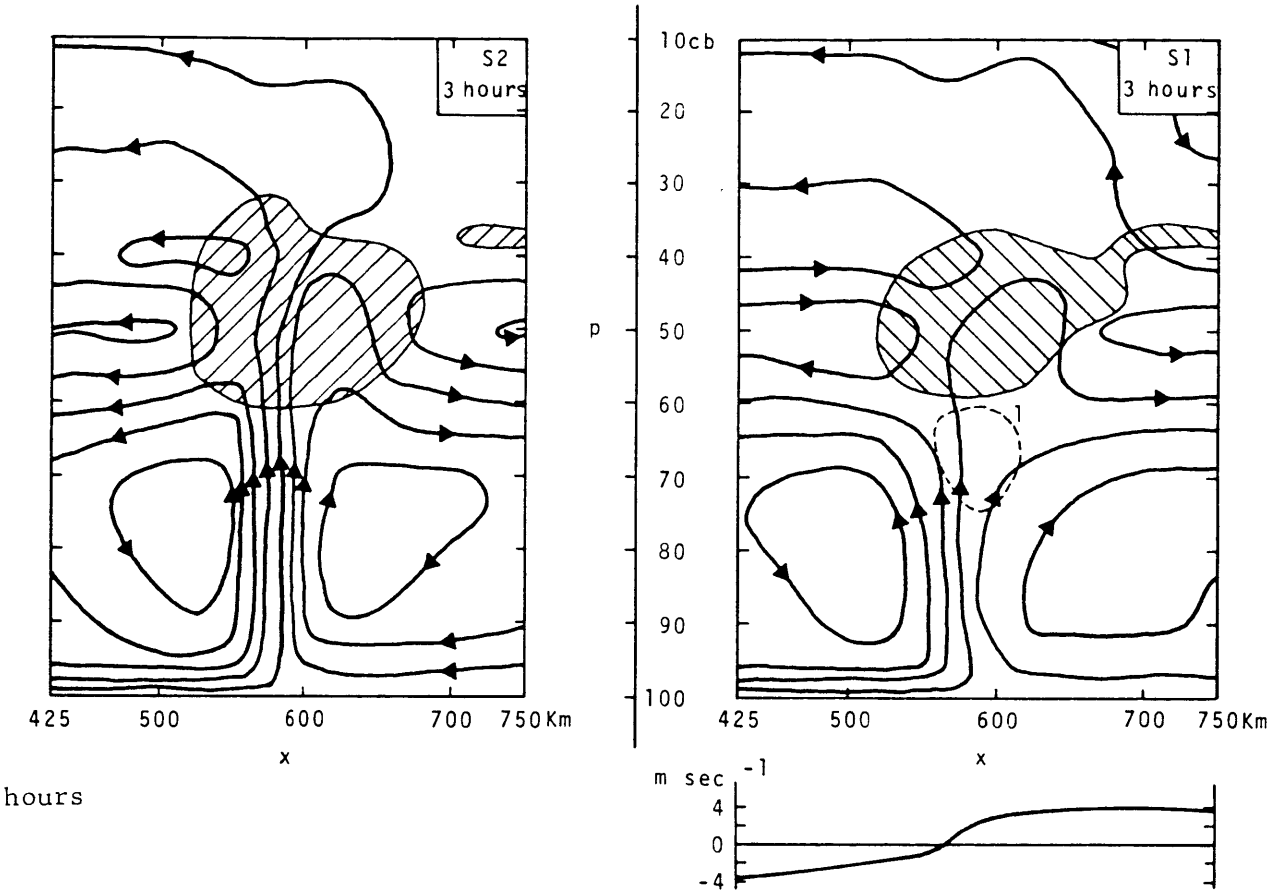
That precipitation evaporation can have a dramatic impact is demonstrated by experiments S1 and S2. These differ only in that E_p is computed according to formula (2.23) in experiment S1, but is always zero in S2. The initial "ageostrophic streamfunction" (see section 4.1.4) in the region of convection is depicted in figure 5-3. In this and in figure 5-4 the streamlines are drawn in intervals of 1.02 ton m^{-1} sec^{-1}. Highest convection cloud top is initially within the 45-50 cb layer. Relative to the ascent beneath, subsidence driven by evaporation of detrained liquid water, centered at 50 cb, is stronger and at a lower level than in the no-shear runs. This is explained in terms of the larger $r_{\ell cm}$.

5.2.1 Time history of experiments S1 and S2

The time history of runs S1 and S2 is depicted in figures 5-4, 5-5, and 5-6. Table 9 supplements these with data on ω, r_ℓ and rainfall. Evaporation of large-scale precipitation is seen to have the following major effects.

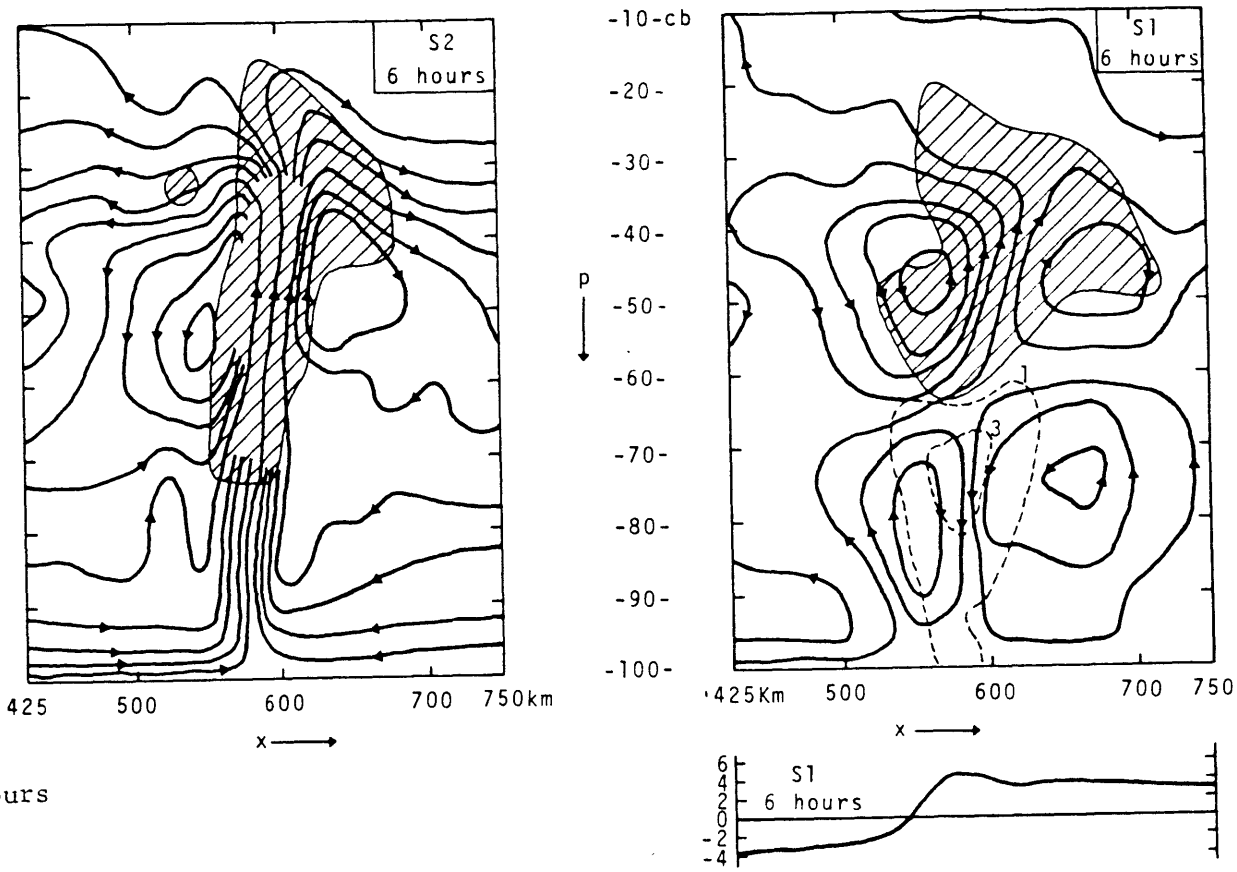
Figure 5-3. Initial ageostrophic streamfunction, runs S1 and S2. Mass flow between like-pointing streamlines: 1.02 ton m^{-1} sec^{-1}. Minimum ω = -2.90 x 10^{-4} cb sec^{-1} at 612.5 and 637.5 km, 95 cb). Maximum ω = 2.76 x 10^{-4} at (587.5 km, 50 cb).





a. 3 hours

Figure 5-4. Ageostrophic streamfunction (streamlines are solid lines with arrows), large-scale cloud (hatched), and isotherms of cooling by evaporation of large-scale precipitation during preceding 3 hours (dashed, degrees C) for runs S1 and S2. Below each diagram depicting conditions in experiment S1 the $\sim$ -profile at 97.5 cb is included. Mass flow between like-pointing streamlines is 1.02 ton m^{-1} sec^{-1}.



b. 6 hours

Figure 5-4. (Continued)

c. 9 hours, S1 only

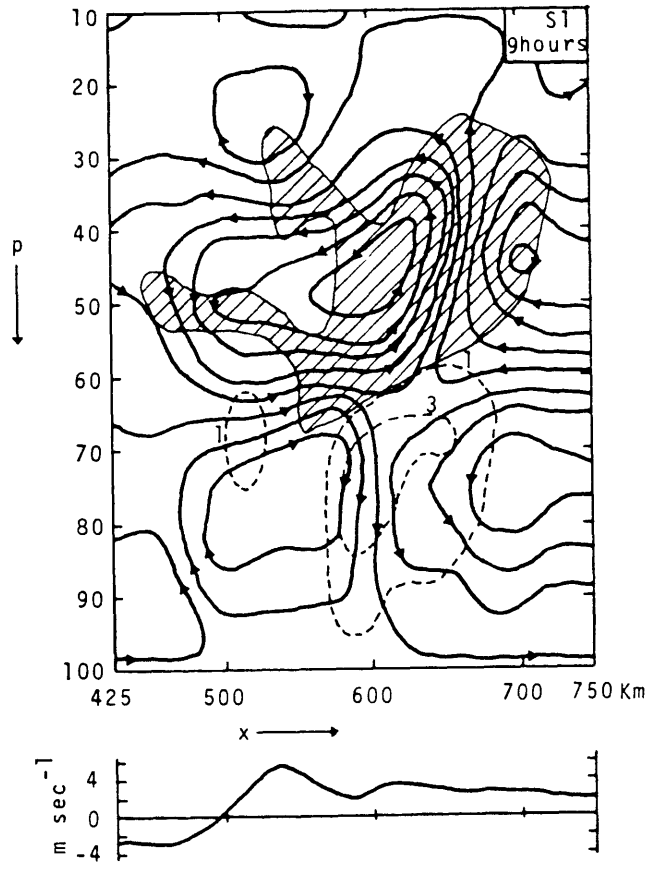
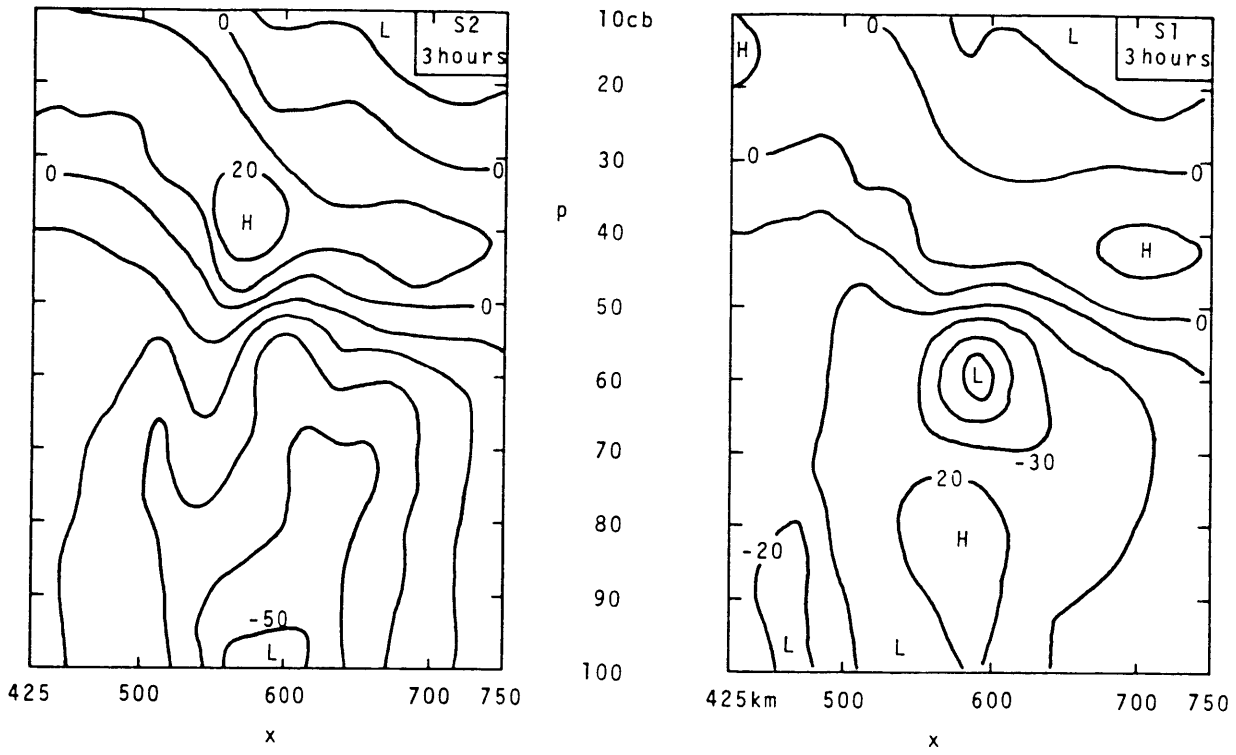
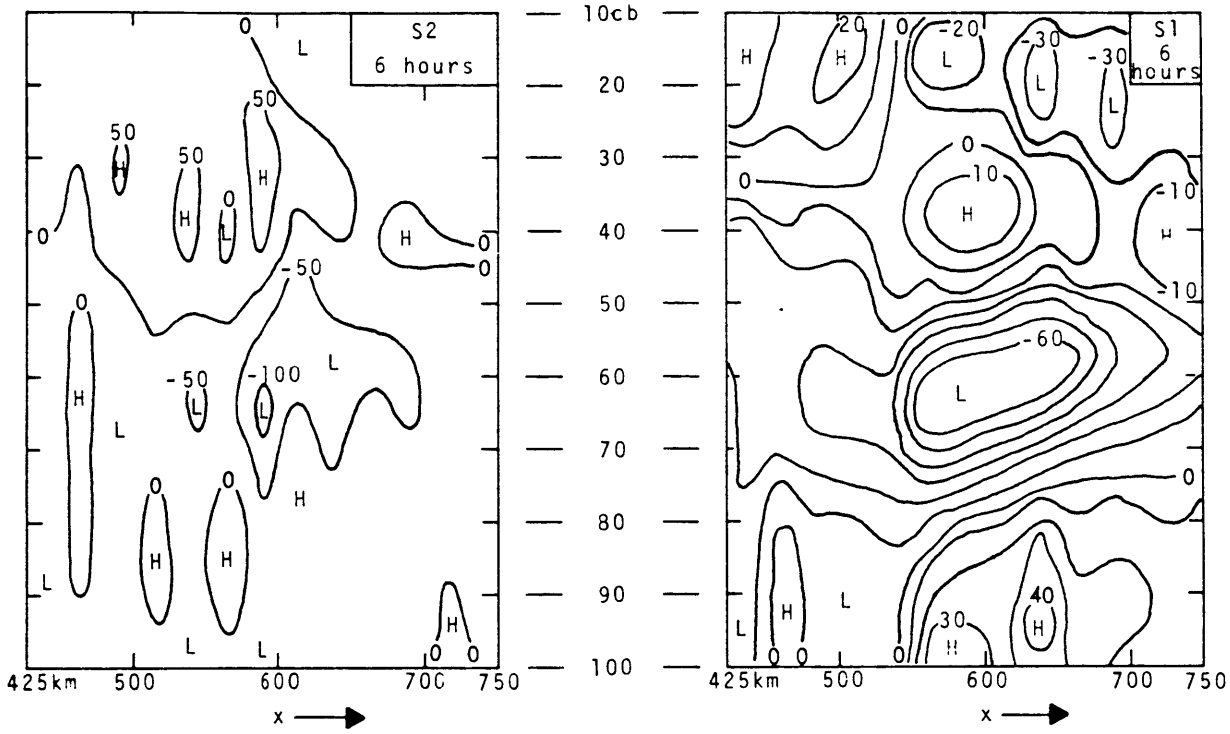


Figure 5-4. (Continued)



a. 3 hours. Contour interval: $+10\ m^2\ sec^{-2}$

Figure 5-5. $\bar{\Phi} - \hat{\bar{\Phi}}$, experiments S1 and S2. Contours labeled in $m^2\ sec^{-2}$. At 6 and 9 hours, experiment S1, $\bar{\Phi} - \hat{\bar{\Phi}}$ is extrapolated to 100 cb using $\bar{T} - \hat{\bar{T}}$ at 97.5 cb, in order to reveal the true strength of the mesohigh.



b. 6 hours. Contour intervals for S1, 10 m^2 sec^{-2}; for S2, 50 m^2 sec^{-2}

Figure 5-5. (Continued)

c. 9 hours, S1 only. Contour interval 20 m^2 sec^{-2}, with some dashed intermediate contours.

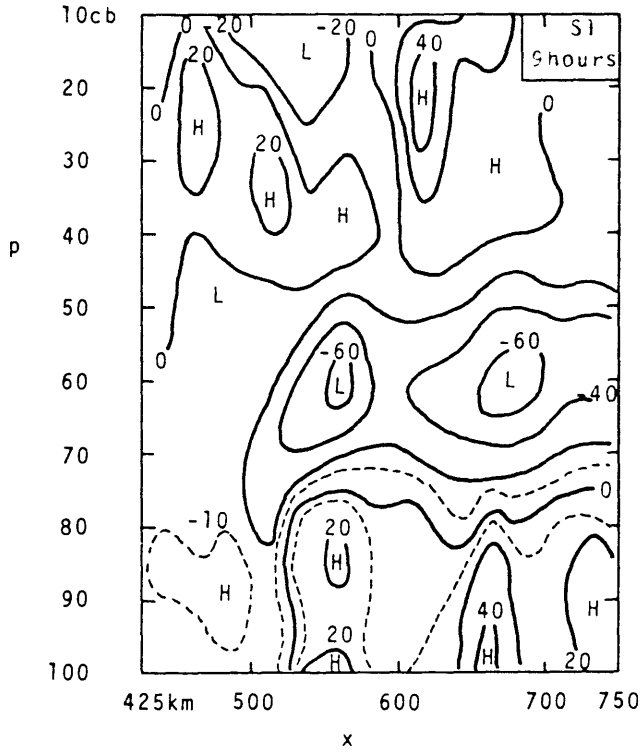
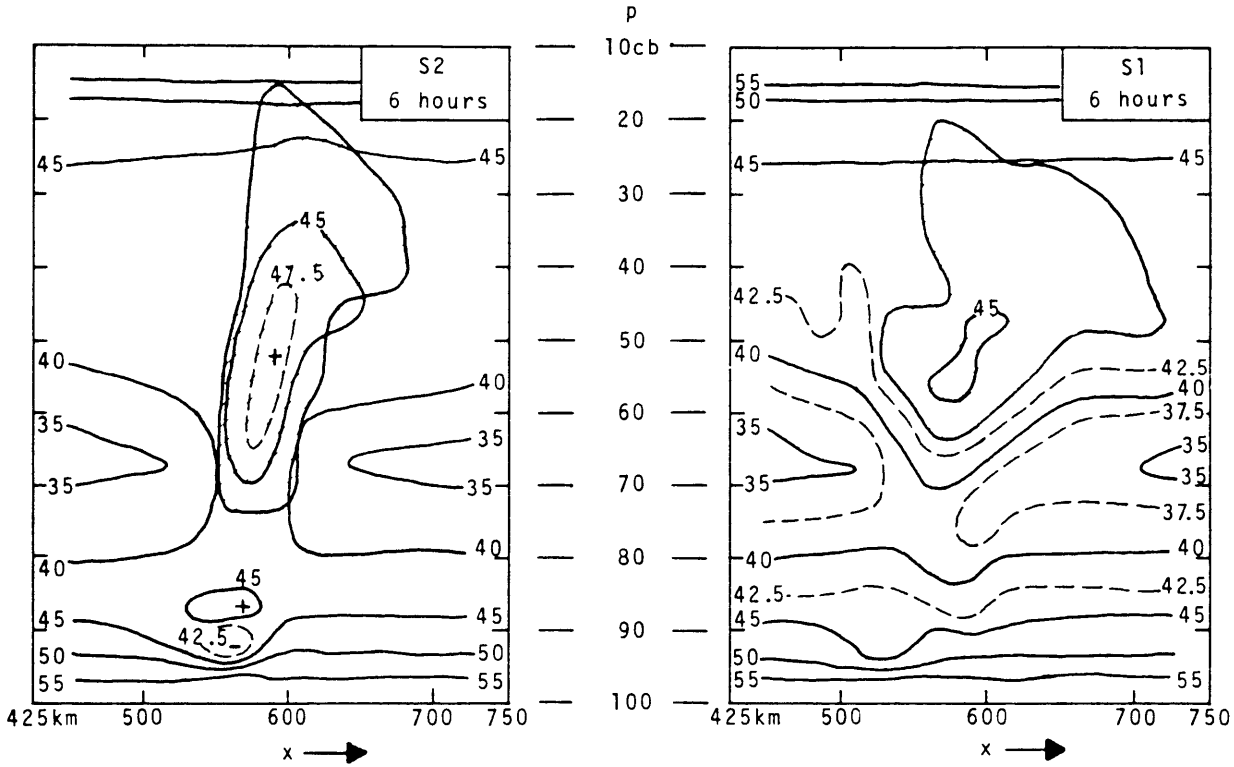


Figure 5-5. (Continued)



a. 6 hours

Figure 5-6. Θ_E cross-sections, experiments S1 and S2. Isotherms are labeled in degrees K minus 300. Large-scale cloud is hatched. Initially, Θ_E is uniform in x with profile given in figure 5-7.

b. 9 hours, S1 only

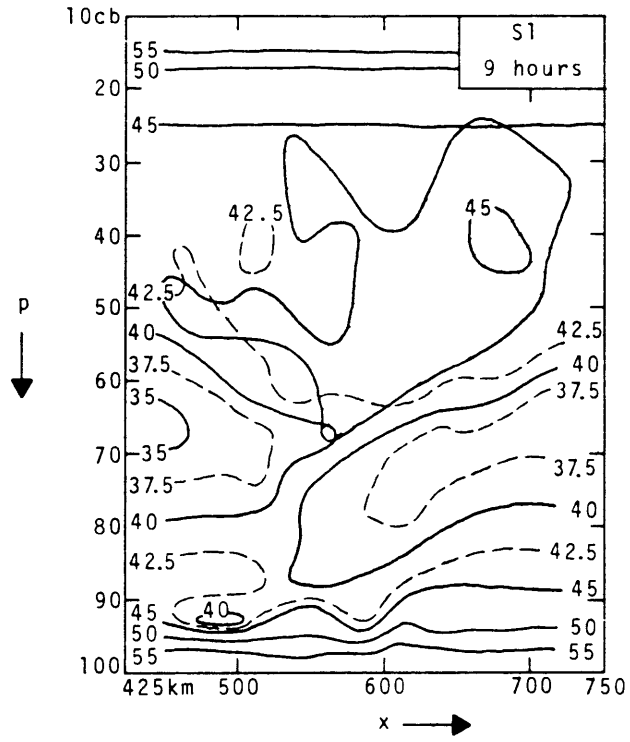


Figure 5-6. (Continued)

Table 9. Supporting and supplementary data for figures 5-4, 5-5, and 5-6. The ω values (all in units of 10^{-4} cb sec^{-1}) are extrema corresponding to important features on figure 5-4. ℓ_2 (units of 10^{-3}) is maximum observed at the indicated time (hours). Maximum surface rainfall (mm) is over the preceding 3 hours

		S1			S2		
		3 hours	6	9	3	6	
(1)	Ascent associated with convection heating below anvil	-9.01 562.5 km 85 cb	-7.55 537.5 km 85 cb	-6.74 487.5 km 80 cb	-13.26 587.5 km 75 cb	-18.86 587.5 km 75 cb	(1)
(2)	Descent associated with large-scale precipitation evaporation	NONE YET	10.92 587.5 km 75 cb	9.82 587.5 km 75 cb	--	--	(2)
(3)	Ascent within large-scale cloud	-3.22 587.5 km 45 cb	-12.98 587.5 km 50 cb	-18.09 662.5 km 40 cb	-9.68 587.5 km 55 cb	-38.73 587.5 km 50 cb	(3)
(4)	Descent within or near large-scale cloud	3.53 637.5 km 50 cb	7.18 537.5 km 50 cb	7.49 487.5 km 55 cb	4.58 637.5 km 50 cb	7.48 562.5 km 50 cb	(4)
(5)	Maximum ℓ_2	1.52 587.5 km 42.5 cb	.68 637.5 km 37.5 cb	.86 662.5 km 32.5 cb	NOT AVAILABLE		(5)
(6)	Maximum cumulus rainfall	0.3 562.5 km 587.5 km	0.5 537.5 km 562.5 km	0.4 537.5 km	0.3 562.5 km 587.5 km	0.3 587.5 km	(6)
(7)	Maximum large-scale rainfall	0.2 587.5 km	2.0 587.5 km	1.7 612.5 km	1.6 587.5 km	20.8 587.5 km	(7)

(a) Formation of a large-scale downdraft of magnitude 10 cm sec^{-1} and an attendant low-level mesohigh. Downward transport of air having low θ_E is evident.

(b) Under the influence of evaporation, weakening, not strengthening, of the original lower-tropospheric ascent region.

(c) Less extreme growth of upward motion within the large-scale cloud.

Excluding the large-scale cloud, the evolution of S2 is qualitatively similar to the first three hours of experiment N3. Both nonlinear advection of horizontal momentum and "allobaric convergence" serve to narrow and amplify the original ascent region. Evidence of the deepening in the geopotential field is seen on figure 5-5a; $\Phi - \hat{\Phi}$ at three hours is minimum at the surface, indicating a warm core. Because the water mixing ratio in convection clouds, r_{lc}, is allowed to be as large as .006, only 20% of the domain-total rainfall is from convection during the first three hours. This total is itself only 70% of that during the corresponding period of experiment N1, which features a decaying disturbance. Deepening of the initial disturbance is therefore not dependent on the total condensation heating. This supports our contention (section 4.3) that β, through its control over $\partial\theta/\partial t$ near 90 cb, is the crucial parameter in determining the stability of the initial disturbance and argues for a marginal stability value somewhat less than 1.35. By three hours the large-scale cloud is clearly warm core and strong upward motion has already developed where net convection heating is positive. Between three and six hours the upward motion in the large-scale cloud quadruples in magnitude and nonlinear processes accumulate much energy in the $2\Delta x$ -scale, as witness the field of

$\Phi - \hat{\Phi}$, figure 5-5b. (There is no solution splitting evident between even and odd timesteps.)

The evolution of S1 is indistinguishable from S2 out to about 1.5 hours, i.e., until appreciable precipitation begins falling out of the "anvil." By three hours, temperature at (587.5 km, 87.5 cb) is dropping, upward vertical motion at (587.5 km, 90 cb) is weakening (time series not shown), and a mesohigh is beginning to develop at low levels. Consequently, imbalance between the x-component of the pressure-gradient force and of the Coriolis force is destructive of low-level convergence. This condition persists, leading to development of the large-scale downdraft between four and five hours in a location where there is strong ascent at three hours. By six hours large-scale precipitation evaporation narrows, weakens, and displaces westward the original region of ascent to the extent that between 60 and 90 cb the downward mass flux is greater than the upward flux. Although $\gamma_s / \gamma_A \approx 7$ initially, narrowing of the disturbance causes it to decrease to 3.9 by three hours. Therefore, we conclude that our choices of $\partial\theta/\partial y$ and a are close to the optimum for development of an evaporation-driven downdraft. This persists in the general region of 600 km through nine hours. The resulting downward transport of θ_E , while not spectacular, is evident on figures 5-6a and b, and provides support for part (a) of our working hypothesis, stated in chapter 1. The pronounced θ_E -minimum present at 92.5 cb and 537.5 km (S1, 6 hours), 487.5 km (S1, 9 hours), and 562.5 km (S2, 6 hours) is a consequence of spurious drying associated with β greater than 1, and is observed also in experiment N3. Between three and nine hours about 60% of the total precipitation from the large-scale cloud evaporates before reaching the sea. This is less

than the 82-87% observed in the no-shear cases because of the smaller rainfall rates in the latter.

5.2.2 The experiment S1 mesohigh

The mesohigh exhibits realistic features (Fujita, 1963), being strongest at the surface and having a "pseudo-cold front," sharp wind speed maximum and direction shift at its advancing (western) edge. Temperature within the mesohigh is typically only 0.5 to 1.2 C colder than to its exterior at the same pressure. The $\phi - \hat{\phi}$ difference across its leading edge at 1000 mb is equivalent to about 0.5 mb at six hours, modest by mid-latitude standards. Thermal wind balance across the front does not exist, consistent with the short time scale of development relative to f^{-1}.

Production of precipitation increases only gradually after the anvil forms. In the early hours, most of the evaporation takes place above the boundary layer and the mesohigh appears first well above the surface (figure 5-5a). Only after three hours does significant cooling by evaporation occur below 90 cb. It is likely that the mesohigh reaches its peak strength at about six hours. The time scale of development of this mesohigh is, therefore, an order of magnitude longer than of mesohighs formed by convective-scale downdrafts within thunderstorms.

The horizontal extent of the mesohigh is controlled by the region over which evaporation is significant. The sharp western edge and diffuse eastern boundary is ascribed to the following. First, because the low-level flow relative to the large-scale rain area is toward the west, in the absence of other influences we should expect to find the coolest air at the western boundary of the precipitation area. Second, the frontogenetical

effect of low-level convergence (which is $\lesssim 10^{-4}$ sec^{-1}) is present west of the high but is weak or absent to its east. Thirdly, the 92.5 cb drying by convection makes for a sharper western boundary to the cooling by evaporation.

Table 10 lists the approximate interpolated positions of certain low-level mesosystem features at six and nine hours, experiment S1. At six hours the western edge of the mesohigh, maximum relative vorticity (wind shift "line"), maximum ascent at low levels, and western edge of the evaporation-cooled air are all essentially coincident, considering the grid resolution. This is similar to natural mesosystems. The western boundary of evaporation-related descent marks the location of the maximum low-level easterly flow in the wind surge. Six-hour gridpoint data from S1 in the vicinity of the pseudo-cold front shows that the χ-component of the pressure-gradient force and the sum of the advection terms appearing in equation (2.1) are the same order of magnitude at 97.5 cb. The same is also true for convection-initiated mesohighs (Fujita, 1963). Friction opposes the pressure-gradient force at 97.5 cb, but at six hours is close to an order of magnitude smaller. Consequently, at six hours a distinct small-scale easterly wind maximum of over 8 m sec^{-1} at (562.5 km, 97.5 cb) has appeared, manifested as the westward-directed streamline flow on figure 5-4b. Low-level convergence ahead of this wind "surge" is associated with active convection, much as is commonly observed in nature. By nine hours the cold front has moved westward at about 5 m sec^{-1}. Complex changes in $\Phi - \hat{\Phi}$ above 85 cb cause the west edge of the mesohigh to lag behind the front (table 10), which gradually weakens under the influence of surface fric-

Table 10. Interpolated positions (km) of low-level mesosystem features, run S1

Time	West edge of mesohigh	Maximum relative vorticity	ω = 0 at west end of evaporation-driven subsidence	Maximum ascent at 90 cb	Western edge of evaporation-cooled air	
					92.5 cb	97.5 cb
6 hours	540	550	570	535	530	545
9 hours	525	505	510	485	495	495

tion. At nine hours the front is visible on figure 5-4c as the leading edge of westward ageostrophic flow near 500 km.

Between the front and 600 km, spreading of rain-cooled air continues at low levels after six hours as precipitation diminishes. East of the wind surge, air which has subsided (figure 5-6b, especially between about 535 and 600 km) is manifest as a warm, dry layer between 85 and 95 cb, with low θ_E , $T-\hat{T}$ of 0.5 to 1.0 C, and relative humidity about 20% lower than the χ-average at 87.5 and 92.5 cb. Finally, we note the formation of another mesohigh in the vicinity of 650-700 km. This region experiences the heaviest large-scale rainfall and evaporation cooling at nine hours.

5.2.3 Anvil circulation, experiments S1 and S2

Anvil liquid water is provided by detrainment and by large-scale condensation. From table 11 it is evident that during experiment S1 the latter provides about 44% of the anvil liquid water. It is probable that condensation is responsible for a similar fraction of the large-scale precipitation. (Comparable data for run S2 is not available, but since the ascent in the large-scale cloud is stronger relative to the vertical motion at 90 cb, the percentage contribution by condensation must certainly be greater.) Thus, as we noted in the runs without shear, large-scale ascent is crucial to anvil longevity and contributes significantly to large-scale precipitation. The upward motion which strengthens so markedly between three and six hours of experiment S2 is a manifestation of conditional instability (of the first kind). The θ_E-cross sections (figure 5-6) prove this, since within the large-scale cloud $\partial\theta_E/\partial p = 0$ corresponds very closely to the moist-adiabatic lapse rate appropriate to equation

Table 11. Liquid-water budget for large-scale cloud, experiment S1. The whole domain is considered, but the anvil depicted on figures 5-4 and 5-6 contributes about 95% to each budget term. Units are ton m^{-1} (3 hour)$^{-1}$

Time period (hours)	Source			Percentage of total source contributed by large-scale condensation	SINK		Net storage
	Detrainment without evaporation	Large-scale condensation	Total		Large-scale evaporation of cloud	Precipitation formation (autoconversion plus collection)	
0-3	313.4	13.0	326.4	4	61.5	130.3	+134.6
3-6	314.1	205.7	519.8	40	91.9	438.0	-10.1
6-9	289.0	477.7	766.7	62	184.8	564.9	+17.0

(2.5). It is apparent from figure 5-4b that the large-scale cloud of run S2 substantially narrows between three and six hours, corresponding to the well-known tendency for the shortest waves to grow most rapidly in the absence of viscosity. Judging from the six-hour θ_E -pattern in large-scale cloud and from the growth of $|\omega|$ within it, the instability is also weakly present in S1, but does not persist. A weakly unstable lapse rate also develops in experiment N1 (section 4.1.4), but vertical velocity amplifies slowly and remains modest.

The sources of the instability in S2 are large liquid water loading and uninterrupted intensification of the large-scale vertical motion underneath the anvil. Large $\bar{r}_{ecm}$ favors net convection heating in the concentrated detrainment layer (section 4.1.2), centered initially near 50 cb where the temperature lapse rate (figure 3-1a) is close to moist adiabatic. At 16 minutes and 47.5 cb the anvil makes its appearance in the vicinity of 600 km. Immediately, net cooling becomes net heating, creating a weak, but distinct θ_E -maximum near the center of the anvil (600 km, 47.5 cb) by three hours. Up to this time the evolution and structure of the S1 anvil does not differ significantly from S2.

As the low-level vertical motion of experiment S2 amplifies, heating within the anvil increases and by three hours the stable lapse rate in the bottom half of the anvil is sufficient to lower maximum cloud top and the concentrated detrainment layer. This, in turn, shifts the convection heating downward. After 4.5 hours the maximum cloud top is below 50 cb, and we note (figure 5-6a) that the θ_E -maximum is below 50 cb at six hours. Convection detrains an ever-increasing supply of air having high θ_E ,

maintaining the unstable lapse rate in spite of ever more potent vertical velocity in the anvil. As the evaporation-driven downdraft of experiment S1 develops, the supply of air with high θ_E provided by detrainment is cut off, and the maximum of θ_E is carried upward and eastward by the flow within the anvil. By nine hours the region having a conditionally unstable lapse rate is relegated to the upper portion of the anvil's eastern lobe. One might anticipate that, had the run been continued beyond nine hours, ascent would have diminished in strength.

It is clear that the conditional instability of S1 does enhance anvil precipitation (and, therefore, its evaporation). In runs exhibiting no conditional instability but with concentrated detrainment below 30 cb (N3, S3, S4, S6) the ascent within large-scale cloud attains a value about equal to the convection induced ascent below. During run S1, $|\omega|$ within the large-scale cloud becomes about double that below. We conclude that roughly half of this, and therefore, half of the large-scale condensation, is the direct consequence of the instability. This feature is responsible for about 20-25% of the total evaporation.

5.2.4 Comparison with observation

Differences between experiments S1 and S2 demonstrate without ambiguity that evaporation from precipitation on the large scale has a central role, in support of our working hypothesis stated in chapter 1. That the S1 disturbance is in broad outline similar to Zipser's Line Islands case can be seen by comparing figures 1-2, 5-4b and c, and 5-6. We judge that figure 1-2a corresponds to sometime between three and six hours of S1, and figure 1-2b to nine hours. It should be remembered that the arrows indi-

cating vertical motion on figure 1-2 are not based on direct measurements, but rather upon inferences from radiosonde data at two stations, satellite cloud pictures, one low-level aircraft flight at 150 m altitude which furnished horizontal wind, temperature, and humidity data, and Zipser's personal observations of the event. Table 12 presents a comparison of various aspects of the S1 and Zipser disturbances, and where possible, the system discussed by Riehl (1965, 1969). There is no indication given in the latter whether or not a mesosystem exists at low levels. Considering anvil rainfall, strength of downdraft, mesohigh, etc., intensity of the Zipser disturbance seems to be greater than of that which evolves in S1. We note the extreme disparity between Zipser's cumulus rainfall and that of S1. This is primarily because of the large $r_{l,m}$. However, had all condensed liquid water precipitated from our convection, the largest cumulus rainfall observed at any one gridpoint would have been 25 mm at 537.5 km, still below Fanning's total. Figure 5-7 shows that much lower θ_E-values are found below 90 cb in Zipser's case. The initial θ_E -profile of S1 does not exhibit as marked a mid-tropospheric θ_E -minimum as is present in the environment of Zipser's disturbance. This accounts for some of the difference between the two profiles. However, we feel that had the large-scale rainfall of S1 been as heavy as the anvil rainfall reported by Zipser, the 340 K isotherm would have reached well below 90 cb.

The Line Islands' low-level mesosystem remains cohesive longer than that of S1. At both Fanning and Palmyra the wind surge and pressure rise were nearly simultaneous. This can possibly be attributed to the stronger mesohigh observed by Zipser; a high of equal strength in S1 would not have been so readily obscured by changes aloft. Convection along the Line

Table 12. Comparison of S1 with the disturbances reported by Zipser (1969) and Riehl (1965, 1969)

Disturbance aspect	S1	Zipser	Riehl
1. Distance covered by anvil, measured normal to leading edge of disturbance (km)	$\leqslant 250$	~ 400	300+
2. Total rainfall (mm)	Max:4.0 (587.5 km)	41 (Fanning) 0.4 (Palmyra)	?
3. Total rainfall from "anvil" (mm)	Max:3.7 (587.5 km)	$\geqslant 10$ (Fanning, estimated from Zipser's data; "steady rain for several hours")	("light rain")
4. Total cumulus rainfall (mm)	Max:1.1 (562.5 km)	$\leqslant 30$ (Fanning estimate)	?
5. Top of convective clouds (cb)	35-50	30-50	Max ~ 25 (radar)
6. Base of anvil (cb)	65	Uncertain--between 70 and 50	70-65
7. Top of anvil (cb)	Max 20-25	?	30 (radar)
8. Average subsidence at 90 cb over downdraft region (cb sec^{-1})	2.5×10^{-4} (6 hours) 1.3×10^{-4} (9 hours)	3.5×10^{-4}	?
9. Intensity of meso-high (pressure inside minus pressure outside)	0.5 mb	1.2 mb (Palmyra)	?
10. Strength of low level wind surge behind cold front relative to ambient flow (m sec^{-1})	3.5 (6 hours) 2.0 (9 hours)	~ 5	?

Table 12. (Continued)

Disturbance aspect	S1	Zipser	Riehl
11. Vorticity at pseudo cold front (sec^{-1})	1.8×10^{-4} (6 hours) 1.5×10^{-4} (9 hours)	$> 1.5 \times 10^{-4}$	?

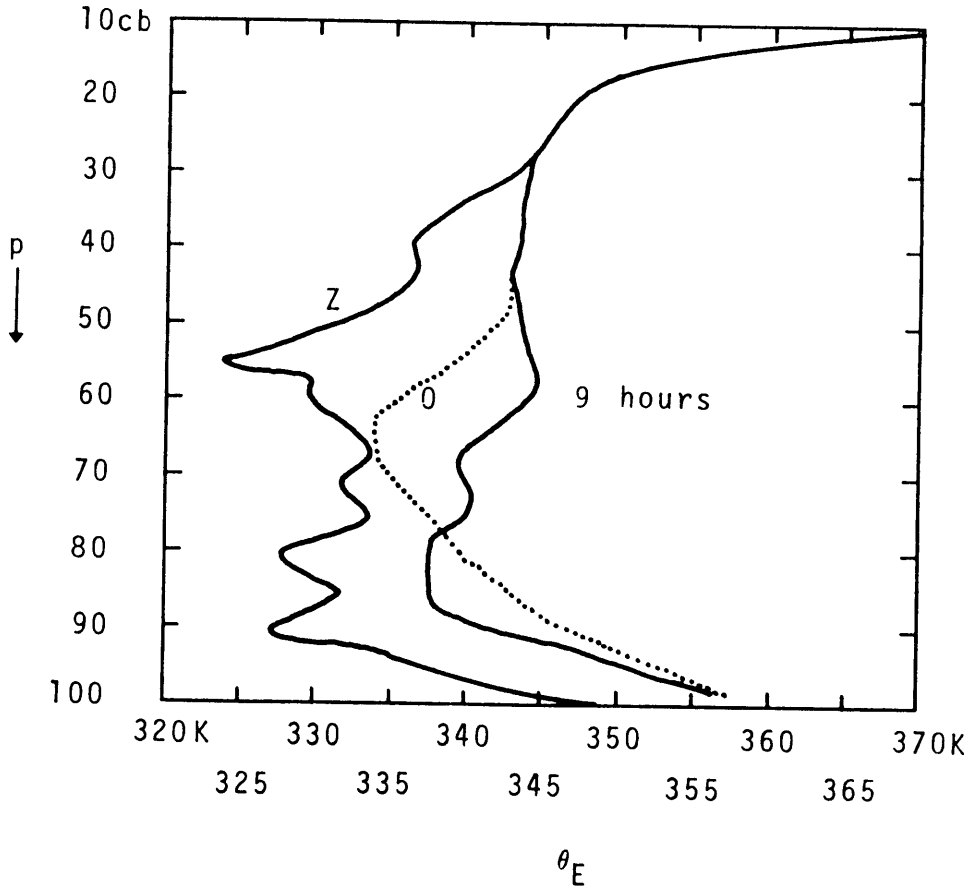


Figure 5-7. Comparison of disturbance θ_E -profiles. The curve labeled "Z" is for the 2050 Z 1 April 1967 sounding at Palmyra Island (Madden et al., 1971). The "9 hours" curve is for experiment S1, 562.5 km. The dotted curve, labeled "0" is the initial profile for all shear computations.

Islands pseudo-cold front weakens with time and produces little or no precipitation (apparently) during the "dying" phase of the disturbance, represented by figure 1-2b. This may be a consequence of the movement of the front into a more stable or drier environment and/or of weakening of the front and associated convergence, with possible implications for the cloud size spectrum (Malkus and Williams, 1963). Both these influences are absent in S1.

The gross aspects of the S1 anvil are similar to those observed by Zipser and Riehl. In particular we call attention to similarities in the dimensions of the three anvils (table 12) and their longevity as precipitation producers. (A similarly dense and long lived precipitating anvil has been reported by Newton, 1950, to the rear of an Ohio squall line. This anvil also was based in the vicinity of 60 cb.) The anvils described by Riehl and Zipser are likely composed entirely of liquid water in their lower portions (Riehl's anvil extends well below the freezing level), with some ice higher up. With such composition in the absence of a continued supply of liquid or solid water substance, either by condensation or by detrainment, precipitation would end in $\sim$ 30 minutes (conversation with Professor Houghton, 1972; Mason, 1969). In the observed anvils, horizontal air trajectories indicate that air parcels produce precipitation for several hours after leaving a region of active detrainment.

Zipser's and Riehl's observations imply the existence of a continuing source of liquid and/or solid water substance other than convection cloud detrainment. The only viable candidate is condensation due to upward vertical motion. On what scale are naturally occurring upward motions in the anvil likely to be observed and to what mechanism can these be attributed?

Large-scale vertical motions in the tropics other than those induced by cumulis convection are $\lesssim$ 1 cm sec^{-1} (Charney, 1963; Baumhefner, 1968; Hawkins, 1972), insufficient to provide the necessary precipitation. Knowledge concerning the vertical motion patterns in ordinary cumulonimbus anvils or in large, dense anvils of the type discussed by Zipser and Riehl is almost entirely lacking. Donaldson's (1971) Doppler radar measurements of an anvil at about 20 cb indicate considerable horizontal variation in the horizontal wind, but are not suitable for obtaining vertical motions. Fankhauser (1971) presents examples of a wakelike confluence at 500 mb downshear from isolated intense cumulonimbi, but again, vertical motions are uncertain. Therefore, we must resort to speculation based on hints provided by Zipser's and Riehl's observations and upon evaluation of the realism of our numerical computations.

Consider the following aspects of the Zipser and Riehl anvils: (a) The lapse rate within each anvil is close to the moist adiabatic. This is evidenced by the 1321Z, 1637Z, and 1835Z 1 April 1967 radiosonde observations from Fanning (Madden et al., 1971) and the 1200Z 8 August 1964 Gran Cayman θ_E-profile given by Riehl (1965, 1969). Therefore, persistent large (say, $>>$ 1 cm sec^{-1}) vertical motions cannot be ruled out by static stability considerations. (b) Zipser notes distinct mesoscale (15-50 km long) areas of "moderate to heavy" rain, with similarly dimensioned regions of speed divergence superposed, during the aircraft flight at 150 m under the anvil. This hints at existence of specific areas of ascent and precipitation generation within the anvil, and raises the possibility that much of the descent induced by evaporation occurs underneath such areas. Riehl does not report features of similar scale, but he is not

as concerned with the mesoscale details as is Zipser. (c) Riehl describes the cloud cover as "stable" (i.e., lacking convection) in appearance. (d) A time-lapse cloud movie taken from Palmyra during the decaying stage of the disturbance shows no evidence of convection within the anvil. In fact, at times there are altocumulus lenticularis present, evidence for the existence of stable internal gravity-wave activity in middle levels. However, the densest part of the anvil never moves over Palmyra. (e) Zipser reports steady rain at Fanning while the anvil is overhead. (It was dark at the time so cloud appearance is unknown.)

These observations infer that ascent within the anvil is likely concentrated in mesoscale areas, rather than being uniform throughout. However, large convective-scale motions within the anvil, as would be observed if the temperature lapse rate is appreciably greater than the moist adiabatic, would seem to be ruled out.

In experiments N1, N3, S3, S4, and S6, ascent within the anvil becomes as large as the heating-induced ascent below. Heating by cumulus convection together with near-zero static stability is responsible. We have seen that conditional instability develops in S1 and S2 and that this is certainly accentuated, if not produced, by the large r_{ecm} . Such instability is also very weakly present in the latter stages of N1 (section 4.1.4), with the large (but more realistic) value of .003 for r_{ecm} . We hesitate to postulate that this is the mechanism by which natural anvils perpetuate themselves. The results of run S5 (section 5.3) do not resolve the uncertainty. Nevertheless, we conclude that heating by convection is an effective mechanism for initiating conditionally stable or neutral mesoscale

vertical motions which contribute substantially to large-scale precipitation.

Two additional factors, not incorporated into our numerical model, may contribute to vertical motions within anvils. These depend upon the anvil layer having a lapse rate at least close to the moist adiabatic. They are, first, turbulence and/or weak convective-scale ascent within the top portions of cumulonimbus clouds which have sheared off from their parent cloud and have been carried downstream as part of the anvil, and second, destabilization by differential long-wave radiative cooling (Godbole, 1973; see also Knollenberg, 1972). The former is prompted by the observation of the author that cumulonimbus tops which become part of a larger-scale cloud layer seem to maintain their identity for some time as darker regions of more threatening appearance.

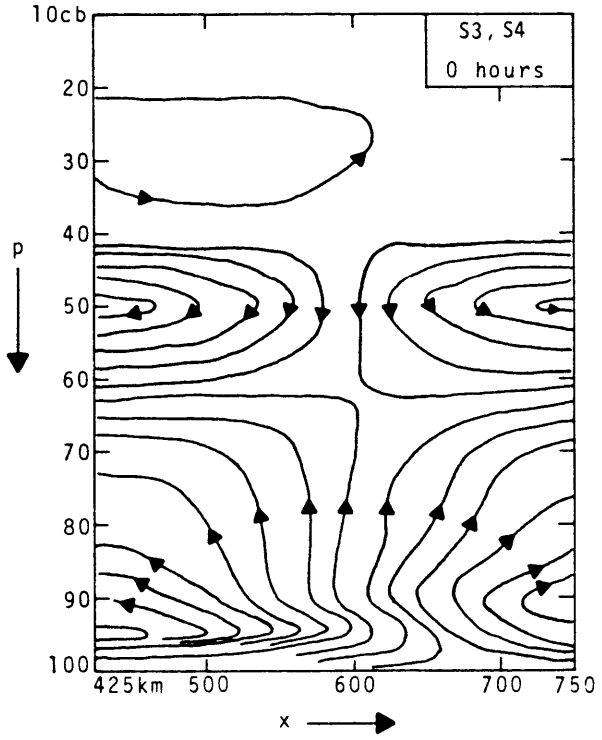
5.3 Experimental results: $\beta = 1.0$

We have noted the favorable resemblance between the S1 disturbance and that described by Zipser, a circumstance which further supports our working hypothesis. In this section we report results which are useful in further evaluation of β, t_{lcm}, and a used in experiments S1 and S2.

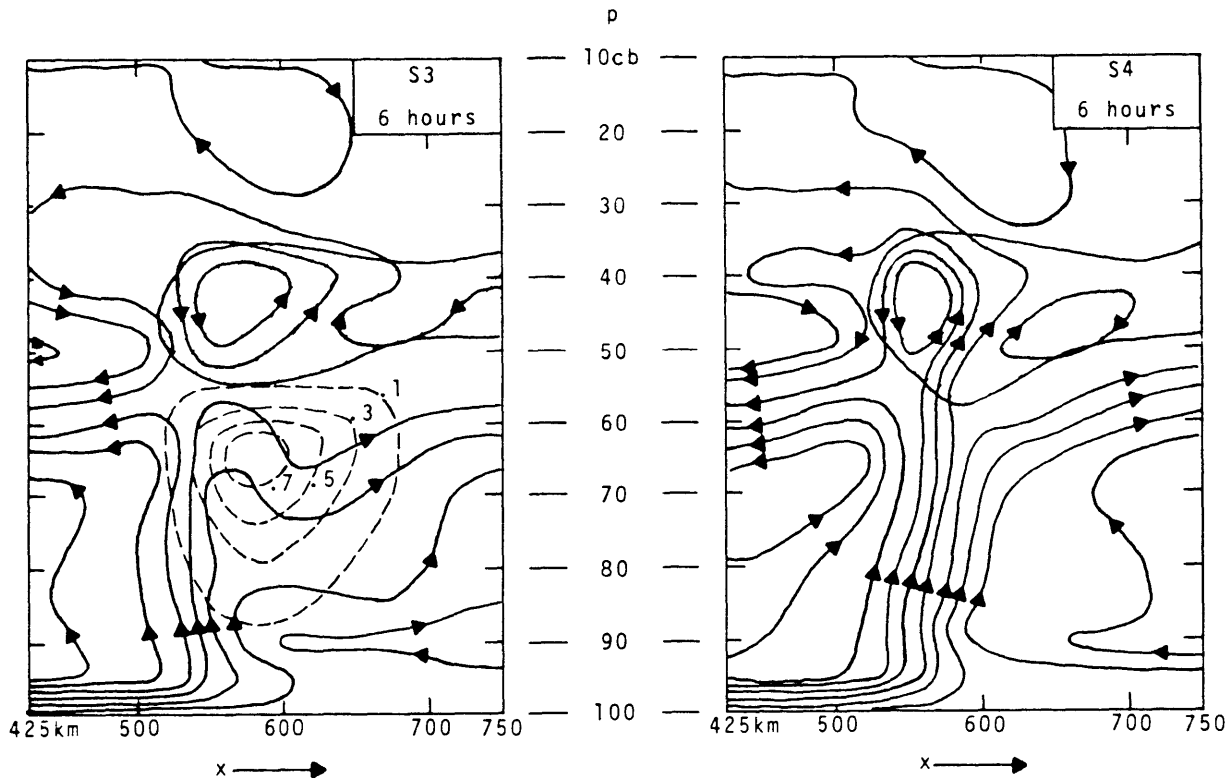
5.3.1 Experiments S3 and S4: analogs to S1 and S2

Runs S3 and S4 are identical to S1 and S2, respectively, save $\beta = 1.0$. Figure 5-8 depicts the ageostrophic streamfunction, areas of large-scale cloud, and, for run S3, isotherms of cooling by evaporation. The interval between successive streamlines in this figure is .255 ton m^{-1} sec^{-1}, pre-

Figure 5-8. As figure 5-4, runs S3 and S4. Mass flow between like-pointing streamlines is .255 ton m^{-1} sec^{-1}.

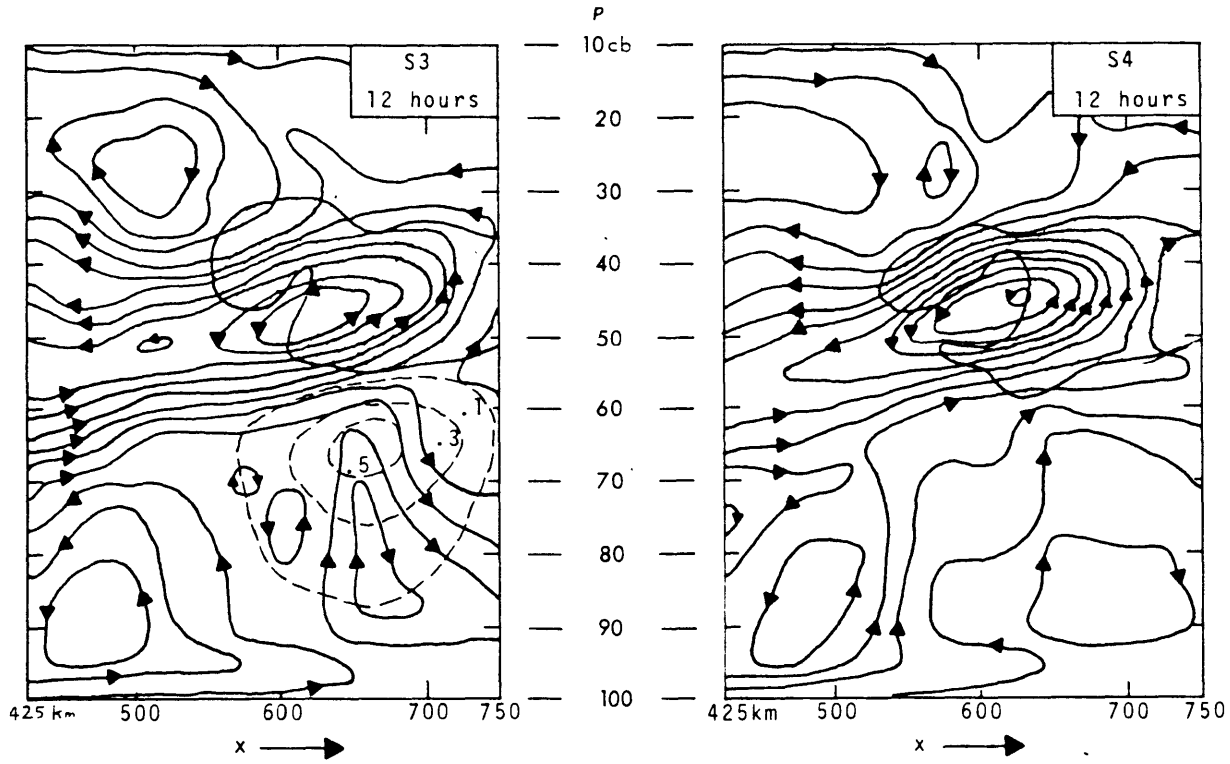


a. Initial



b. 6 hours

Figure 5-8. (Continued)



c. 12 hours

Figure 5-8. (Continued)

cisely .25 of that in figure 5-4. Table 13 provides supplementary data for these two runs.

It is evident that assigning β the value 1.0 has the same consequences as in the no-shear case--the disturbance weakens at low levels and convective activity diminishes. The net effect of this is that differences between S3 and S4 are insubstantial. Because of the presence of baroclinicity, there is neither as marked nor as rapid a breakdown as is observed with experiment N1. Disparate areas of predominant ascent and predominant subsidence consistent with quasi-geostrophic reasoning persist on the scale of the initial wave disturbance.

An anvil forms at 0.7 hours in response to detrainment. Compared with experiments S1 and S2, this detrainment is less, both in an absolute sense and relative to the advection of unsaturated air from the west by the upper flow. Liquid-water contents are modest (table 13), and, near the western edge of the region of convection, detrainment is insufficient to maintain the anvil in the face of advection of unsaturated air. Evaporation of detrained liquid water continues large, maintaining the persistent subsidence observed toward the western edge of the anvil (figures 5-8b and c). Convection heating inside the anvil is considerably reduced from its S1 and S2 value. Consequently, we observe neither a large increase in θ_E in the lower and central portions of the anvil nor the formation of a stable layer near the base of the anvil. Both developments are manifestations of the process which establishes a conditionally unstable lapse rate within the anvils of S1 and S2. Between three and six hours, subsidence within the anvil does give way to ascent in its central portion in response to convection heating. The strength of this ascent relative to that below the

Table 13. Supporting and supplementary data for figure 5-8. The ω values (in units of 10^{-4} cb sec^{-1}) are extrema corresponding to important features on figure 5-8. ζ (units of 10^{-3}) is maximum observed at the indicated time (hours). Maximum surface rainfall (mm) is for the preceding 3 hours

	S3				S4				
	3 hours	6	9	12	3	6	9	12	
(1) Ascent associated with convection heating below anvil	-2.29 562.5 km 90 cb	-2.20 537.5 km 90 cb	-2.78 512.5 km 65 cb	-1.86 637.5 km 75 cb	-2.38 562.5 km 90 cb	-2.65 562.5 km 70 cb	-1.81 537.5 km 90 cb	-1.97 537.5 km 85 cb	(1)
(2) Descent associated with large-scale precipitation evaporation	NONE YET	1.15 587.5 km 60 cb	1.40 612.5 km 70 cb	1.60 687.5 km 65 cb	--	--	--	--	(2)
(3) Ascent within or near large-scale cloud	NONE YET	-1.20 587.5 km 45 cb	-2.16 637.5 km 45 cb	-2.60 712.5 km 45 cb	NONE YET	-2.73 587.5 km 45 cb	-2.60 637.5 km 45 cb	-2.59 687.5 km 45 cb	(3)
(4) Descent within or near large-scale cloud	1.10 537.5 km 50 cb	2.16 537.5 km 45 cb	2.71 512.5 km 45 cb	1.98 562.5 km 40 cb	1.07 537.5 km 50 cb	2.60 537.5 km 45 cb	2.89 537.5 km 45 cb	2.94 562.5 km 40 cb	(4)
(5) Maximum ζ	.237 587.5 km 47.5 cb	.469 587.5 km 42.5 cb	.258 662.5 km 42.5 cb	.279 712.5 km 42.5 cb	.249 587.5 km 47.5 cb	.607 587.5 km 42.5 cb	.385 637.5 km 42.5 cb	.359 687.5 km 42.5 cb	(5)
(6) Maximum cumulus rainfall	.04 587.5 km	.17 562.5 km	.16 537.5 km	.15 587.5 km	.04 587.5 km	.20 562.5 km	.20 562.5 km	.12 587.5 km	(6)
(7) Maximum large-scale rainfall	.01 587.5 km	.15 587.5 km	.18 587.5 km	.13 662.5 km	.09 587.5 km	1.07 587.5 km	1.85 587.5 km	.98 637.5 km	(7)

anvil is less than observed in S1 and S2 because of the absence of a conditionally unstable lapse rate.

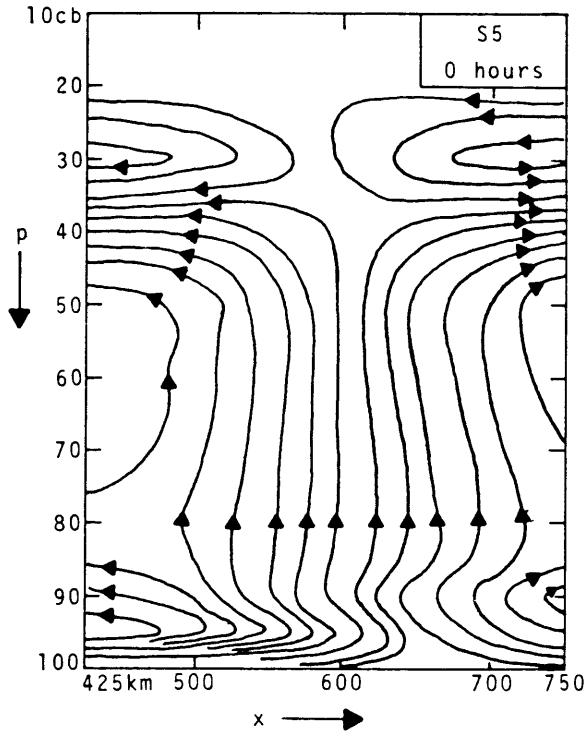
With no substantive stable layer to stop the plume updrafts, detrainment is concentrated slightly higher than in S1 and S2, and the base of the anvil is therefore 5 to 10 cb higher. This circumstance, and more importantly, the smaller precipitation rates from the anvil, cause the evaporation cooling in run S3 to be centered well above 70 cb, with cooling rates per three hours below 90 cb less than 0.1 C. This is less than 10% of the low-level cooling rate during most of experiment S1. Although evaporation is strong enough to initiate a small region of subsidence near 70 cb of strength comparable to the ascent in the region of active convection (table 13) this subsidence never penetrates into the boundary layer. There is, of course, no indication of a low level mesosystem. The ratio, $\gamma_S/\gamma_A \approx 7$ initially, drops to 3.0 by three hours, and decreases further later. Thus, the lack of response of the flow to evaporation does not result from inappropriate values of α and $\partial\theta/\partial y$. Large-scale rainfall totals no more than about 0.5 mm at any one location during run S3. Fantasizing slightly, if S3 had been a real life situation over the Line Islands, there is no way that a keen observer such as Zipser would have concluded that this disturbance has the structure attributed to the 31 March- 1 April 1967 event. This is in contrast to experiment S1. We therefore conclude that these two $\beta = 1.0$ experiments are more applicable to the study of the atmospheric response to very light rain from altostratus than to the type of disturbance with which we are primarily concerned.

5.3.2 Experiments S5 and S6: $r_{\ell cm}$ and a

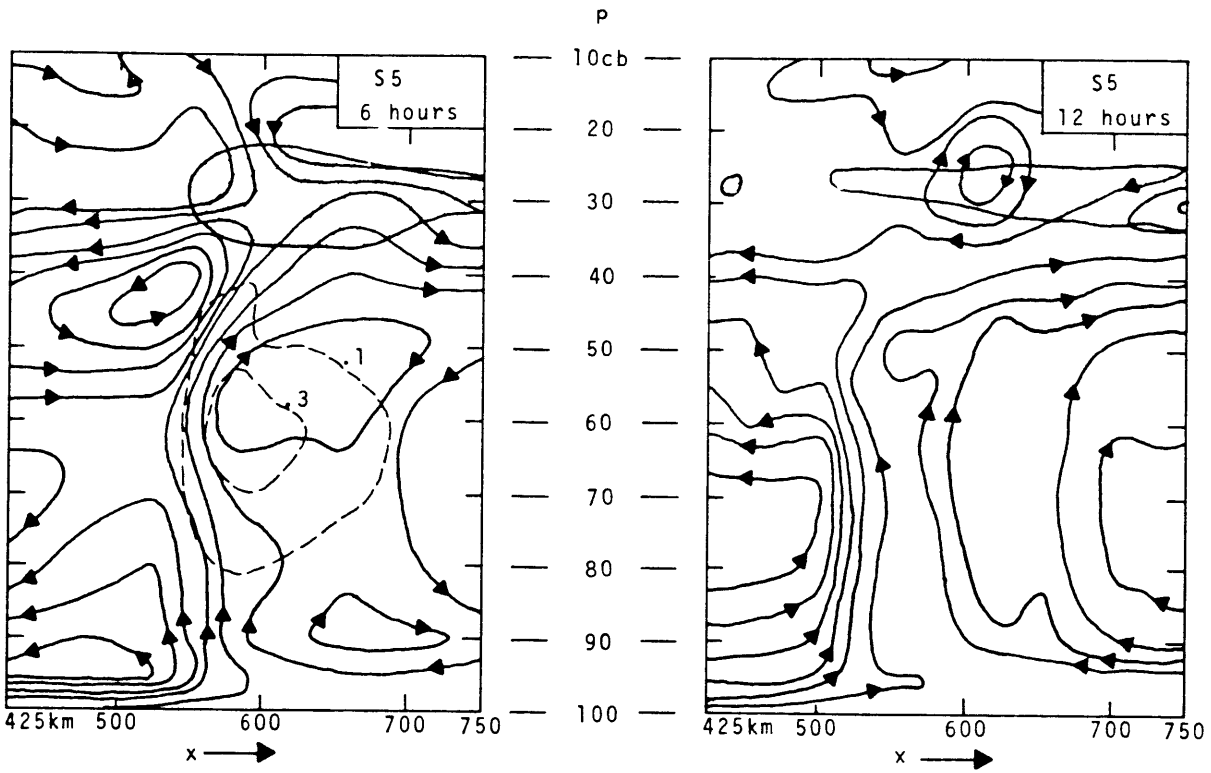
Run S5 demonstrates the importance of $r_{\ell cm}$. It is identical to S3 in all respects except that $r_{\ell cm}$ = .002 (table 8). Figure 5-9 is to be compared with figure 5-8, run S3. Ageostrophic streamline intervals and isotherms of evaporational cooling are the same as in figure 5-8. Table 14 supplements figure 5-9 with additional data on ω, r_ℓ and rainfall. Initially, maximum cloud top, p_t , is within the 25-30 cb layer, 15 cb higher than in run S3 because of the reduced liquid-water load. For a given upward mass flux into convective clouds at cloud base, M_c , equation (2.17) and (2.18) show that M_c is larger above cloud base the smaller are p_1 , the level at which the plume loses buoyancy, and p_t . Thus, the taller clouds of S5 favor more warming above cloud base level. With smaller $r_{\ell cm}$, cooling by evaporation of detrained liquid water is less, i.e., in terms of the section 4.1.2 definition, the clouds are more "efficient" -- over 80% efficient. These two factors explains the more vigorous initial ascent, its presence at higher levels, and also why the weakening with time of the upward mass flux across the disturbance is not as great in mid-troposphere as at low levels.

The anvil first forms at 0.9 hours at 27.5 cb, above the initial moist layer between 35 and 50 cb. Because of the stable stratification at cloud-top level, detrainment is concentrated through a shallower layer (in terms of pressure) than in S3. Below the concentrated detrainment layer, compensating subsidence [incorporated in $C_{\mathcal{N}}$, see equation (4.2)], is so large that this moist layer dries significantly. It is clear from the maximum r_ℓ listed in tables 13 and 14 that more intense convective activity in S5 only partially makes up for the smaller liquid-water mixing ratio of

Figure 5-9. As figure 5-4, experiment S5. Mass flow between like-pointing streamlines is .255 ton m^{-1} sec^{-1}.



a. Initial



b. 6 hours

c. 12 hours

Figure 5-9. (Continued)

Table 14. Supporting and supplementary data for figure 5-9. The ω - values (in units of 10^{-4} cb sec^{-1}) are extrema corresponding to important features on figure 5-9. ζ (units of 10^{-3}) is maximum observed at the indicated time (hours). Maximum surface rainfall (mm) is for the preceding 3 hour period.

	S5				
	3 hours	6	9	12	
(1) Ascent associated with convection heating below anvil	-3.38 587.5 km 50 cb	-3.76 562.5 km 45 cb	-2.96 562.5 km 45 cb	-3.41 512.5 km 75 cb	(1)
(2) Descent associated with large-scale precipitation evaporation		NONE OBVIOUS			
(3) Ascent within large-scale cloud	-1.65 587.5 km 35 cb	-1.23 587.5 km 35 cb	-.73 587.5 km 20 cb	-1.63 587.5 km 25 cb	(3)
(4) Descent within or near large-scale cloud	1.48 687.5 km 30 cb	2.34 587.5 km 20 cb	2.10 537.5 km 20 cb	1.22 637.5 km 25 cb	(4)
(5) Maximum	.327 612.5 km 27.5 cb	.307 587.5 km 27.5 cb	.112 687.5 km 27.5 cb	.183 612.5 km 27.5 cb	(5)
(6) Maximum cululus rainfall	2.81 587.5 km	3.82 562.5 km	2.58 537.5 km	2.51 537.5 km	(6)
(7) Maximum large-scale rainfall	.01 612.5 km	.06 587.5 km	.03 637.5 km	.01 662.5 km	(7)

the detrained air. Moist static stability is appreciable above 35 cb. Consequently, anvil air parcels do not make substantial vertical excursions; vertical motions (table 14) are much weaker relative to ascent below the anvil than in other runs, and the motions in the anvil are unsteady. For this reason and because of the great height of the anvil, large-scale condensation is an order of magnitude less than in run S3, and, during any particular three-hour period, never contributes more than about 30% of the anvil's liquid water supply, and with diminished convection with little help from large-scale condensation, the anvil decreases in thickness and density after three hours.

Large-scale precipitation is meager. Although 87-90% of it evaporates after leaving the anvil, cooling by evaporation is a minor item in the heat budget and there is no positively identifiable response in the streamfunction field (figure 5-9b and c).

The ratio, γ_s/γ_A = 4.0 initially, decreases to 2.6 by three hours and subsequently becomes smaller as the ascent region narrows. This suggests that there exists no combination of $\partial\theta/\partial y$ and α which would produce a significantly greater tendency toward an evaporation-induced downdraft. This run is emphatic in its indication that a high-based anvil does not produce much precipitation, a contention supported by observation. Precipitation from such an anvil is too light because insufficient water substance is available and because static stability inhibits development of large vertical motions within the anvil. Providing our modeling of detrainment in the top part of our convective-cloud layer is reasonably accurate, another inference from the S5 results is possible. If natural clouds all happen to detrain at one level, we should not expect, in

response to the convection, middle- or high-cloud formation at a lower level. Therefore, under normal tropical conditions, an active, precipitating anvil will not form unless there is substantial detrainment below $\sim$ 30-40 cb. The existence of clouds (as in Riehl's, 1965, case) which detrain above this level is not precluded, but these must coexist with clouds which detrain at a lower level.

A more realistic value of $.5556 \times 10^{-3}$ sec^{-1} for a is tested in run S6, which in all other respects is identical to S3. Liquid-water mixing ratio in the anvil remains only $.15 \times 10^{-3}$ as a consequence of the greater efficiency of the autoconversion process. Otherwise, differences between S3 and S6 are minor, and no results from the latter are shown. γ_s / γ_A = 1.9 initially and about 0.9 by three hours. Consistent with this we observe the precipitation to be centered only slightly east of the axis of the ascent region. The response of the flow is that anticipated in section 5.1. During the first six hours heating-induced ascent is slightly weaker than in S3, and at six hours precipitation-driven descent is also slightly weaker, in spite of there being more evaporational cooling. Specifically, at six hours the maximum subsidence induced by evaporation is 1.15×10^{-4} cb sec^{-1} in experiment S3, and 1.01×10^{-4} cb sec^{-1} in experiment S6, whereas, during the preceding three hours maximum local cooling by evaporation is .83 C in S3 and .92 C in S6. By nine hours, after the ascent within the anvil has become significant, the evaporation-induced downdraft is slightly stronger than in S3. The descent does not penetrate below 85 cb.

We conclude that the value of a is not critical to $\beta = 1.0$ computations and there is every reason to believe the same is true for $\beta = 1.35$.

Since $A_c \sim A_u$ in S1, the time scale of microphysical processes is substantially less than two hours so that increasing a would probably have proportionally less effect. Extrapolating from our comparison of S3 and S6, we anticipate that the evaporation-driven downdraft would develop sooner and perhaps be only 90% as strong.

6. CONCLUSIONS AND SUGGESTIONS FOR FUTURE RESEARCH

In this chapter we shall summarize the discussion in the preceding four chapters with emphasis on conclusions relating to our working hypothesis. We shall also mention possible model improvements and topics which should be pursued in future research.

6.1 Summary and conclusions

This research was inspired by the observational studies of Riehl (1965, 1969) and Zipser (1969), which suggest a possible major role for precipitation evaporation on a space scale larger than the convective scale. Our working hypothesis, as stated in chapter 1, is: "that evaporation of precipitation falling from a widespread thick layer of altostratus cloud is sufficient to produce a mesoscale downdraft having sufficient strength and persistence to (a) alter the θ_E -profile so that it resembles observed disturbance profiles exemplified by figure 1-1, and (b) alter the dynamics of the large scale to the extent that to ignore such evaporation is to make a qualitative error."

To use as our basic tool in testing this hypothesis we designed a numerical model having the following main aspects. (a) Dynamics are governed by the hydrostatic unfiltered equation set. (b) Cumulus convection is parameterized using a one-dimensional plume model allowing for the vertical transport of water substance in vapor and liquid form. (c) A complete water budget is included, comprised of the individual budgets of vapor, cloud, and precipitation. The microphysical processes "autoconversion," "collection" (accretion) and large-scale precipitation evaporation

are parameterized, after the manner of Kessler (1969). Model equations are solved by standard finite-difference procedures. We employ no special computational devices, such as grid nesting, variable grid spacing, or smoothing (either explicit, or implicit through the use of a lateral eddy viscosity).

Model computations bearing most critically on the hypothesis are (section 5.2) the shear runs S1, with large-scale evaporation included, and S2, with evaporation set equal to 0 but otherwise identical. The comparative results are in support of both parts (a) and (b) of our hypothesis. A mesoscale downdraft of peak magnitude 10 cm sec^{-1} develops in response to evaporation of rain from a thick, dense "anvil." Descent is sufficiently strong and persistent to transport mid-tropospheric air to lower levels and to be associated with a weak, but realistic surface mesosystem. Moreover, evaporative cooling is sufficient to reverse the deepening induced by convection heating.

It is clear that the process we are studying is (in the model) the end result of at least two "layers" of parameterization. Acceptance of our results depends upon a careful scrutiny of the parameterizations employed. This we have attempted in the preceding chapters, and our main conclusions are summarized below.

(a) Given a certain precipitation water content, ℓ_p , we judge the evaporation rate to be accurate to approximately $\pm 25\%$ (section 2.4 and Appendix E). We do not regard this as justification for doubting the validity of our results, particularly since the errors appear to be predominantly on the side of underestimation.

(b) The microphysical parameterizations of autoconversion and collection, although crude, are believed adequate. Their performance in numerical models of cumulus clouds has generally been judged satisfactory. Of importance is that we find only a slight sensitivity of the model to a fourfold variation in the autoconversion coefficient, α (section 5.3). This is the only free parameter, once we agree to the use of the Marshall-Palmer drop-size distribution with $N_0 = 10^7$ m^{-4}, and to the value of one for the efficiency of collection of cloud drops by precipitation (section 2.4).

(c) The validity of our results is then seen to rest upon the accuracy and validity of two processes which supply about equal amounts of liquid water to the model "anvil" (table 11). These are: detrainment of liquid water from convective clouds, and condensation associated with large-scale ascent within the anvil.

(d) The principal uncertainties and free parameters which relate to detrainment of liquid water are as follows, assuming that an individual cloud may be satisfactorily represented as a plume (section 2.3.1):
(1) The value of β in (2.10). Results from our model depend critically upon the assigned value of β. For β greater than about 1.25, deepening of the initial wave disturbance occurs and sufficient liquid water is detrained to form a dense large-scale cloud. Otherwise, this cloud is diffuse and evaporation unimportant. We presented (section 4.1.2) observational evidence, which has limited applicability to our small time and space scale, in favor of β being larger than unity. On this basis and in consideration of the meteorological realism of the $\beta = 1.35$ results as compared to those associated with $\beta = 1.0$, we claim that 1.35 is a plausi-

ble choice. A more definitive statement must await further research. (2) Lack of a spectrum of cloud sizes, contrary to observed/implied cloud cluster populations (section 4.1.2). From this we infer that mass detrainment is too concentrated near the level of zero plume buoyancy appropriate to our assigned entrainment rate of .2 per kilometer. Nevertheless, when a deeper layer is considered the total mass detrainment may not be overestimated. (3) The maximum liquid-water content in cumulus, $r_{\ell cm}$. The value .006, assumed in experiments S1 through S4 and S6, is not supported by observations (section 5.1); these would seem to indicate a value of .002 as appropriate. Therefore, with $r_{\ell cm}$ = .006, detrainment in the model is occurring at a rate equivalent to convection activity in nature (as measured, for instance, by mass flux upward through convective cloud base) which is about three times that of the model.

(e) Mesoscale vertical motions are present within the model anvil during all runs. This is consistent with inferences concerning the anvils observed by Riehl and Zipser (section 5.2.4). These motions are responsible for the longevity of the anvil as a precipitation-producer. In our computations we find that ascent strength within the anvil is related to within-anvil intensity of heating by cumulus convection and moist static stability. In all numerical computations during which ascent (as measured by ω) within the anvil becomes as large as ascent at lower levels induced by convection heating, the anvil is centered at or below 35 cb and the moist static stability is near zero. During runs S1 and S2, ascent in the anvil becomes larger than ascent below; this is a consequence of conditional instability, which is, in turn, initiated, or at least intensified, by too large $r_{\ell cm}$. This, possibly spurious, instability is responsible

for about 20 to 25% of large-scale rainfall, with most of the rainfall enhancement coming after the evaporation downdraft is well established. We further speculate that rainfall from natural anvils may be augmented by within anvil turbulence and/or radiation processes, neither of which are included in our computations.

From the foregoing, major sources of uncertainty concerning the extent to which our results support our hypothesis are the choices of β , the ratio of upward mass flux through convective cloud base to the large-scale mass flux at 90 cb, and of $r_{\ell cm}$, maximum liquid-water mixing ratio of detrained convective-cloud air. A logical sequel to the experiments reported on in chapter 5 is a computation with β assigned the value 1.35, $r_{\ell cm}$ = .002, and the entrainment rate larger than 0.2 km^{-1} such that, initially, concentrated detrainment is into the same layer as in run S1. We predict that such an experiment would not show as strong a downdraft as in S1, but stronger than in S3 and sufficient to perturb the boundary layer. However, uncertainty concerning β would remain.

Based on our numerical-model results, we conclude that in the tropics cooling by evaporation of non-convective precipitation is likely to have crucial implications for the dynamics of the ideal disturbance characterized by plentiful, but only moderately deep convection. In other words, a disturbance is most likely to show development of a dense, thick, precipitating anvil if it possesses a high population density of cumulus congestus and cumulonimbus which detrain primarily below about 35 cb, that is, where the lapse rate is generally only slightly less than the moist adiabatic.

Furthermore, we conclude that large vertical motions in the anvil are essential to its persistence and precipitation production. The precise mechanisms producing these motions in natural anvils remain unknown.

In addition we suggest that development of an anvil which is responsible for widespread light rain at the surface is followed by reversal of any deepening tendency, as measured by, e.g., disturbance-scale convergence or relative vorticity at low levels. We would not expect this to hold for disturbances having a very moist environment.

We do not consider our numerical-model results to be definitive concerning the necessity for vertical wind shear. On the basis of physical reasoning we concluded (section 5.1) that intensity of anvil precipitation is greatest when shear is absent, but also that a downdraft driven by evaporation cooling is less likely to develop, or, if it does, is weaker. Zipser (1968) has cited cases similar to that reported in his 1969 paper, except that vertical shear is small, and we recall the probable large effect evaporation has on the evolution of experiment N3 (section 4.2).

There are interesting aspects of our computations which are not associated with precipitation evaporation. In spite of Rossby number about 0.8, initialization with the quasi-geostrophic divergence above the boundary layer proves quite satisfactory. We conclude that an accurate initialization above the boundary layer must incorporate stratification and we show that this can be done satisfactorily in this model by adding frictional forcing directly to the quasi-geostrophic ω-equation. For reasons of expediency we have ignored stratification in the initialization of all but one (N2) of the complete model runs. For β in excess of our experimentally estimated stability criterion, at low levels subsidence induced by

clouds in the cloud environment is stronger than large-scale subsidence outside the region of convection. This leads to formation of a warm core at low levels in the initial wave disturbance. Intensification of the disturbance is by the "allobaric" process on account of the short (relative to f^{-1}) time scale. Friction is a retarding influence. We have no reason to doubt that had, for instance, one of our shear runs been repeated without friction and with β equal to 1.35, deepening would have occurred, baroclinic forcing being the favorable large-scale ingredient. Nonlinear advection in the boundary layer is responsible for narrowing of the ascent region in all runs; this is particularly marked with $\beta > 1.0$. The boundary layer of only one run, N2, can be said to be an Ekman layer; in this case the divergent component of the flow is very weak. In all other runs, nonlinear advective terms are, at least locally, of the same order of magnitude as other terms in the momentum equations.

6.2 Suggestions for future research

Additional case studies such as Zipser (1969), but with more complete data coverage, including radar, will be necessary to either confirm or deny the conclusions reached in this study. In particular, such projects should undertake to determine the anvil-water budget as accurately as possible, in what layer detrainment is concentrated, the temperature structure of the anvil, and whether or not there exists large vertical motion within the anvil.

It is also possible that precipitation evaporation on scales larger than convective may occasionally be of importance in mid-latitude mesoscale systems, although, in many cases the effects of evaporation probably tend

to be masked by synoptic-scale variability. Newton (1950) cites evidence for subsidence induced by evaporation underneath a large ($\sim$ 200 km wide) anvil associated with a squall line. The writer has observed from Iowa a number of situations characterized by persistent "anvils" which, following thunderstorms, produced steady rain for at least one to two hours. These are invariably associated with, but not necessarily the cause of, marked mesoscale pressure fluctuations and wind variability.

Improvements to the model might include recasting the basic equations in spectral form in order to accurately describe nonlinear advection, which, as we have seen, is important on the mesoscale. In the process of so doing, the water-budget equations and cumulus parameterization would require special attention. It also appears desirable to improve vertical resolution so that low-level mesosystems can be more accurately described.

Two assumptions are common to all present cumulus-parameterization schemes and are (apparently) valid for interactions between convection and large-scale flows characterized by time scales $\gtrsim$ one day. These are (a) the quasi-equilibrium, (i.e., the parameterizability) assumption [terminology of Arakawa and Schubert, 1974; equation (2.10) in our case] relating convective activity to the instantaneous state of the large scale, and (b) the assumption that the fractional area covered by convective clouds is everywhere much less than one.

Of fundamental importance is the question of the parameterizability of cumulus convection in terms of instantaneous fields of the explicitly forecast mesoscale variables. Arakawa and Schubert (1974) have shown that the "adjustment time" of convection to a slowly changing large-scale environment is of order 10^3 to 10^4 seconds (a figure in agreement with the

author's intuitive notion, based on observation). This time scale is that characteristic of mesoscale motions. It is therefore evident a priori that the quasi-equilibrium assumption is inadequate for estimating mesoscale: convective-scale interactions. It may be possible to say, by analogy with inertia-gravity waves and geostrophic adjustment, that mesoscale features associated with cumulus convection are generic to the adjustment process. It may happen in many applications (hopefully, including the present one) to the mesoscale:convective-scale interaction problem that the quasi-equilibrium assumption is satisfactory. It is the opinion of the writer that before introducing the Arakawa parameterization into a mesoscale model, an effort should be made to verify his quasi-equilibrium assumption using mesoscale data. The National Severe Storms Laboratory mesonet comes to mind.

At cloud base, fractional cloud area, η , is given by (2.16). Values of about 0.1 are typical of experiment S1, and η becomes as large as one-third during run N3. We have undertaken a crude analysis of the errors incurred by assuming $\eta \ll 1$, see Appendix C. From this we learn that the explicit error in the prediction of $\bar{\theta}$ (grid area average of θ) is not serious, but that because the quantity $(q_{cloud}/\bar{q} - 1)$, $q = r$ or r_w , is not small, serious errors are incurred in the water-budget equations. These, in turn, will eventually contaminate the prediction of $\bar{\theta}$. It is evident that a distinction must be made between cloud and environment within each grid square. This problem deserves much further attention.

Finally, the time is right, in the author's opinion, to seriously attack the problem of convective-scale downdrafts. It is well known that downdrafts within cumulonimbus clouds are critical to the development and

maintenance of mid-latitude squall lines (e.g., Newton, 1967); Betts (1973) has presented evidence that mass transport in cumulonimbus downdrafts is about half as large as the updraft transport. It is noted in chapter 1 that in important respects mesoscale and convective-scale downdrafts are indistinguishable in their influence upon the large scale. We have seen from our numerical computations that under ideal conditions mesoscale downdrafts are of great significance, even to the extent of terminating development initiated by CISK. It is reasonable to assume that convective-scale downdrafts can also quash CISK, but possibly under a wider range of conditions (for instance, when convective cloud tops are very high). Thus, the writer is of the opinion that a strong effort should be directed toward developing a downdraft parameterization. The strength and properties of convective-scale downdrafts are apparently much more dependent on microphysical precipitation processes and vertical shear of the horizontal wind in the environment than are those of updrafts. The first step in parameterization must be to learn more about downdraft dynamics through careful observational studies. This knowledge would then provide a check on results of numerical modeling of deep convection (e.g. Hane, 1974) which might in turn permit extension or generalization of the observational conclusions. In the author's judgment, successful numerical forecasting of the mesoscale depends upon the development of an adequate downdraft parameterization.

Appendix A. Energy and the constraints on the domain average of u and v

Defining

$$\hat{(\,)} \equiv \frac{1}{L_x}\int_0^{L_x} (\,)\,dx \quad , \text{ and}$$

$$\langle(\,)\rangle \equiv \frac{1}{p_\infty}\int_0^{p_\infty} (\,)\,dp \quad ,$$

we first consider the domain average of (2.1),

$$\frac{\partial \langle \hat{u} \rangle}{\partial t} = \langle \Phi \rangle\Big|_{x=0} - \langle \Phi \rangle\Big|_{x=L_x} + f\langle \hat{v} \rangle + \langle \hat{F}_x \rangle .$$

With the constraint that $\langle \hat{u} \rangle$ is constant in time (section 2.1), it follows that $\langle \hat{v} \rangle$ must be zero in the absence of friction providing that

$\langle \Phi \rangle\Big|_{x=0} = \langle \Phi \rangle\Big|_{x=L_x}$. In all our runs $\langle \hat{F}_x \rangle \neq 0$. We choose to keep the constraint $\langle \hat{v} \rangle = 0$ and allow $\langle \Phi \rangle\Big|_{x=L_x} \neq \langle \Phi \rangle\Big|_{x=0}$.

Thus, the momentum loss by surface friction is exactly compensated by a net east-west pressure force.

The energy equation for the set (2.1)-(2.5), derivable using standard procedures, contains the term $fv\left[u_g - (p/\chi)\,\partial u_g/\partial p\right]$, where u_g is the zonal geostrophic wind and $\chi = R/c_p$. This term is the rate of pressure work by the north-south velocity component plus the north-south

advection of total potential energy. To eliminate this spurious term, it is sufficient to assume that $\partial\theta/\partial y$ is everywhere constant, once we agree that $\langle\hat{v}\rangle = 0$.

The restrictions on $\langle\hat{u}\rangle$ and $\langle\hat{v}\rangle$ are incorporated into the time integration of (2.1) and (2.2) (step number 2 of table 1) as follows. (a) It is convenient at each time step to partition $\Phi(x, y, p, t)$ into 2 parts. The first of these, Φ_{1n}, is computed directly from (2.3) at time step $n+1$ using $\Phi_{1n} = 0$ at 97.5 cb for all x. Since $\partial\theta/\partial y$ is constant, $\partial^2\Phi_{1n}/\partial x\partial y = 0$. (b) Tentative values of u and v at $n+1$, designated u_1 and v_1, are computed using $\Phi = \Phi_{1n}$. (c) $\Phi_{2n}(x, y)$ is defined by the corrections which must be applied to these in order that the $\langle\hat{u}\rangle$ and $\langle\hat{v}\rangle$ constraints be satisfied. (In the actual computer program, Φ_{2n} is not explicitly computed unless the Φ_n array is to be printed out.) For a leapfrog time step,

$$u_{n+1} = u_{1,n+1} - 2\Delta t \frac{\partial\Phi_{2n}}{\partial x} \tag{A.1}$$

$$v_{n+1} = v_{1,n+1} - 2\Delta t \frac{\partial\Phi_{2n}}{\partial y}, \tag{A.2}$$

whence,

$$\langle u_{n+1}\rangle = \langle u_{1,n+1}\rangle - 2\Delta t \frac{\partial\Phi_{2n}}{\partial x}$$

$$\langle\hat{v}_{n+1}\rangle = \langle\hat{v}_{1,n+1}\rangle - 2\Delta t \frac{\partial\hat{\Phi}_{2n}}{\partial y}.$$

From mass continuity $\langle u_{n+1} \rangle = \langle \hat{u} \rangle$, therefore

$$2\Delta t \frac{\partial \Phi_{2n}}{\partial x} = \langle u_{1\,n+1} \rangle - \langle \hat{u} \rangle \; ; \qquad \text{(A.3)}$$

the x-variation of Φ_2 must be such that mass continuity and the $\langle \bar{u} \rangle$ constraint are both satisfied. By substituting (A.3) into (A.1) we obtain the final u_{n+1} . With $\langle \hat{v}_{n+1} \rangle$ constrained to be 0,

$2\Delta t \left(\partial \hat{\Phi}_{2n} / \partial y \right) = \langle \hat{v}_{1\,n+1} \rangle$. Since $\partial u_1 / \partial y = 0 = \partial u / \partial y$,

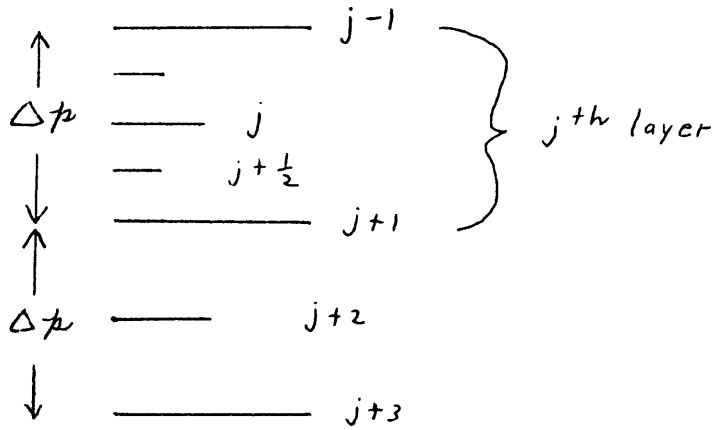
$\partial^2 \Phi_{2n} / \partial x \partial y = 0$; therefore $v_{n+1} = v_{1\,n+1} - \langle \hat{v}_{1\,n+1} \rangle$. Φ_2 is computed by assuming it 0 at $x = 0$ and then using (A.3). All figures depicting geopotential in chapters 4 and 5 are for $\Phi = \Phi_1 + \Phi_2$ with its x-average subtracted.

Appendix B. Computation of C_θ, C_r and C_{rv}

Letting q be θ, r, or r_v (as in section 2.3.2), we write, for a pressure level at which convective clouds are present,

$$C = g\left[-\frac{\partial}{\partial p}(\bar{q} M_c) + \bar{q}_c \frac{\partial q_m}{\partial p} + q_c q_m \frac{\partial \lambda}{\partial p}\right]. \quad \text{(B.1)}$$

C represents C_θ, C_r, or C_{rv}, and the overbar indicates a large-scale variable. The finite difference analogue of this expression for gridcolumns containing convective clouds is the subject of this section. The subscript notation is as indicated below for one sample computational layer within such a column (see figure 2-1).



For a computational layer above that containing cloud base, we write (B.1) in terms of finite differences as

$$C_j = \frac{g}{\Delta p}\Big[\left(\bar{q}_{j-1} M_{c_{j-1}} - \bar{q}_{j+1} M_{c_{j+1}}\right)$$

$$+ \bar{q}_j h_{j-1}\left(m_{j+1} - m_{j-1}\right)$$

$$+ \bar{q}_{j+\frac{1}{2}}\left(h_{j+1} - h_{j-1}\right)\left(m_j - m_{j+1}\right)$$

$$+ q_{c_j} m_j \left(h_{j+1} - h_{j-1}\right)\Big]. \qquad \text{(B.2)}$$

The first and last terms in this expression follow directly from the first and last terms in (B.1). However, the second term in (B.1), the entrainment of environment air into convective clouds, is broken up into 2 parts when finite differences are applied. Referring back to point (k) in section 2.3.1, if $\partial h/\partial p > 0$ in the j th layer, then some of the plumes penetrating the base of this layer have their top in this layer, while the remainder top out above it. We assume that all entrainment into plumes having top above the j th layer occurs at p_j [second term in (B.2)]. Furthermore, all plumes topping out in the j th layer do so at p_j, and all entrainment into these occurs at $p_{j+\frac{1}{2}}$ [3rd term in (B.2)].

$\bar{q}_{j+\frac{1}{2}} \equiv .75\ \bar{q}_j + .25\ \bar{q}_{j+2}$.

C is treated using analogous procedures in a computational layer which contains the convective cloud base level or is below it.

Appendix C. Consequences of assuming fractional cloud area is negligible

An a posteriori check of our assumption that the fractional area, η, covered by convective clouds is much less than one reveals that this is a source of error when $\beta > 1.0$. Equation (2.16) can be used to estimate η at cloud base, η_b. By three hours of experiment N3, the large-scale upward vertical velocity at 90 cb reaches 23 cm sec^{-1}, corresponding to $\eta_b = .34$. During most of experiments S1 and S2, η_b is also greater than 0.1 at certain gridpoints. In what follows, we estimate a portion of the error in the forecast of $\bar{\theta}$ and $\bar{r}$.

In the derivation of equation (B.1) from (2.21), we assume $\eta << 1$. The fractional error in C_θ and C_r we define as

$\epsilon \equiv \frac{\text{correct - used}}{\text{correct}}$, where "correct" is the expression for C_θ or C_r taken directly from (2.21), and "used" is C_θ or C_r corresponding to (B.1), the expression actually used in the model. In terms of the dummy variable, q:

$$\epsilon = \frac{\left[\eta_m \frac{\partial}{\partial p}\left[(\bar{q} - q_e) k\right] + \frac{\partial}{\partial p}\left[(q_e - \bar{q})\bar{M}\right]\right]}{-\eta_m \frac{\partial}{\partial p}(q_e k) + q_c \eta_m \frac{\partial k}{\partial p} + \frac{\partial}{\partial p}\left[(q_e - \bar{q})\bar{M}\right]} \qquad (C.1)$$

The overbar indicates a large-scale variable and q_e is the value of q in the cloud environment. We evaluate ϵ by substituting the expressions $(\bar{q} - q_e) = [\eta/(1-\eta)](q_c - \bar{q})$, and $q_e = (\bar{q} - \eta q_c)/(1-\eta)$ to eliminate q_e, and by assuming $\eta = k \eta_b$. Our choice of k is that depicted in figure 2.2. The sounding used to derive this profile provides

$\bar{q}$ and the cloud computation (r_{crit} = .003) yields q_c . Because, in fact, $\bar{q}$ is unequal to q in the cloud environment, q_e , ϵ reveals only part of the consequence of assuming $\gamma << 1$; error in the cloud computation, when $\bar{q}$ replaces q_e in (2.12), is another source of error in C_θ , C_r and C_w . This is not included in the following listing of ϵ as a function of pressure.

	ϵ	
Pressure	$q = \theta$	$q = r$
42.5	-.369	-.040
47.5	-.003	.021
52.5	.007	.136
57.5	.023	.280
62.5	.024	.633
67.5	.015	-1.240
72.5	.017	-.302
77.5	.018	-.180
82.5	.028	-.101
87.5	.027	-.055

The error in the prediction of θ is small in spite of large γ ; the prediction of $\bar{r}$ is less accurate. Except for θ at 47.5 cb, the sign of ϵ is that of the "correct" value of C_θ or C_r , indicating that the effect of (B.1) is to <u>underestimate</u> the actual changes. The large values of ϵ at 42.5 cb for θ , and at 62.5 and 67.5 for r , are where the "correct" value is small in magnitude. To a first approximation, ϵ is linear in γ for a given λ , $\bar{q}$ and q_c so long as γ is not too large.

The alternative to assuming $\gamma << 1$ is a considerable reworking of the computation procedure (table 1). In particular, an explicit water vapor budget for the cloud environment is necessary. The implicit rela-

tionship between q_c, q_e and γ, given $\bar{q}$ and assuming $\gamma = \lambda \gamma_b$, would require an iterative procedure involving solution of (2.12). The processes involving non-convective precipitation would logically only occur in the cumulus-cloud environment. No computations incorporating these modifications have been carried out. We think that, in spite of γ_b being 0.10 to 0.15 during much of S1 and S2, the basic conclusions relating to these runs still hold, and that the sensitivity of the model to β is independent of the assumption that $\gamma << 1$. Nevertheless, removing this assumption should be a primary aim of future research.

Appendix D. Fallout of precipitation: numerical procedures

Kessler (1969, p. 20) provides an approximate expression for the fall-speed of an individual raindrop, $V_p = -130 (\rho_0/\rho_s)^{0.5} D^{0.5}$ [m sec^{-1}], where ρ_s and ρ_0 (100 cb) are (Jordan, 1958) standard densities, and D is the drop diameter [m]. The mass-weighted average of this over all drops in the Marshall-Palmer distribution, expressed in terms of pressure as the independent variable, is $\omega_p = 285\, \rho_s^{.625}\, \rho_0^{0.5}\, r_p^{.125}$ [cb sec^{-1}]. Thus, ω_p is a weak function of r_p and pressure. Figure D-1 illustrates this for a typical range of r_p. The assumed constant value of ω = 0.05 cb sec^{-1} is a slight overestimate for most r_p observed, more so at lower pressures.

The Marchuk scheme (Phillips, 1973) for the equation $\partial q/\partial t = -\omega\, \partial q/\partial p$, $\omega > 0$, is, for $t = n\Delta t$, layer thickness Δp, and $\sigma \equiv \omega \Delta t/\Delta p$,

$$q_{j\, n+\frac{1}{2}} = q_{jn} - \frac{\sigma}{2}\left(q_{j\, n+\frac{1}{2}} - q_{j-1\, n+\frac{1}{2}}\right)$$

$$q_{j\, n+1} = q_{jn} - \frac{\sigma}{2}\left(q_{j+1\, n+\frac{1}{2}} - q_{j-1\, n+\frac{1}{2}}\right).$$

The amplification factor for this is 1 for all σ. Thus Δt (90 or 180 seconds) can be the same as that used with the other large-scale equations. Figure D-2 presents the results from an application of the Marchuk scheme to (2.8), with A and E_p set to zero. One may observe that the phase speed of the maximum value of r_p is about 25% too slow when Δt = 180 seconds, but that there is considerable downstream diffusion of

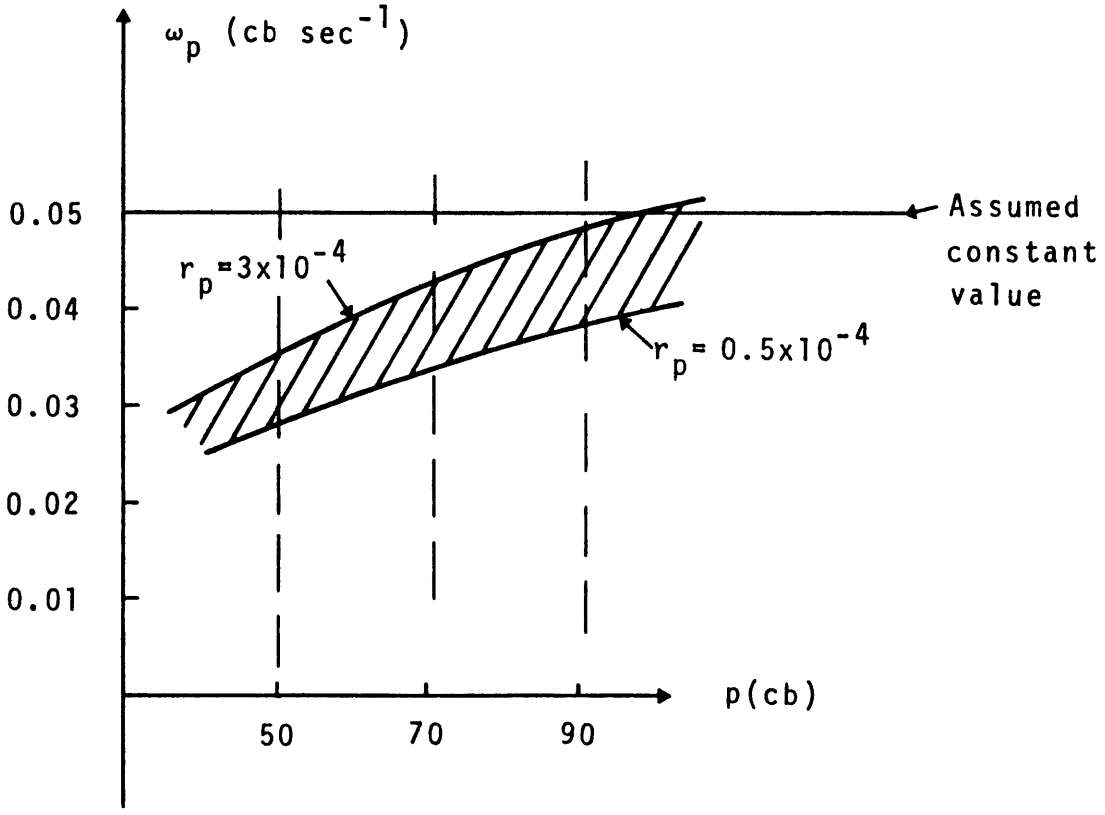


Figure D-1. Plot of $\omega_p = 285\ \rho^{.625}\ \rho_c^{0.5}\ r_p^{.125}$ with pressure for a typical range of precipitation-water mixing ratio (r_p) in our experiments. The constant value of $\omega_p = 0.05$ cb sec^{-1} is shown for comparison.

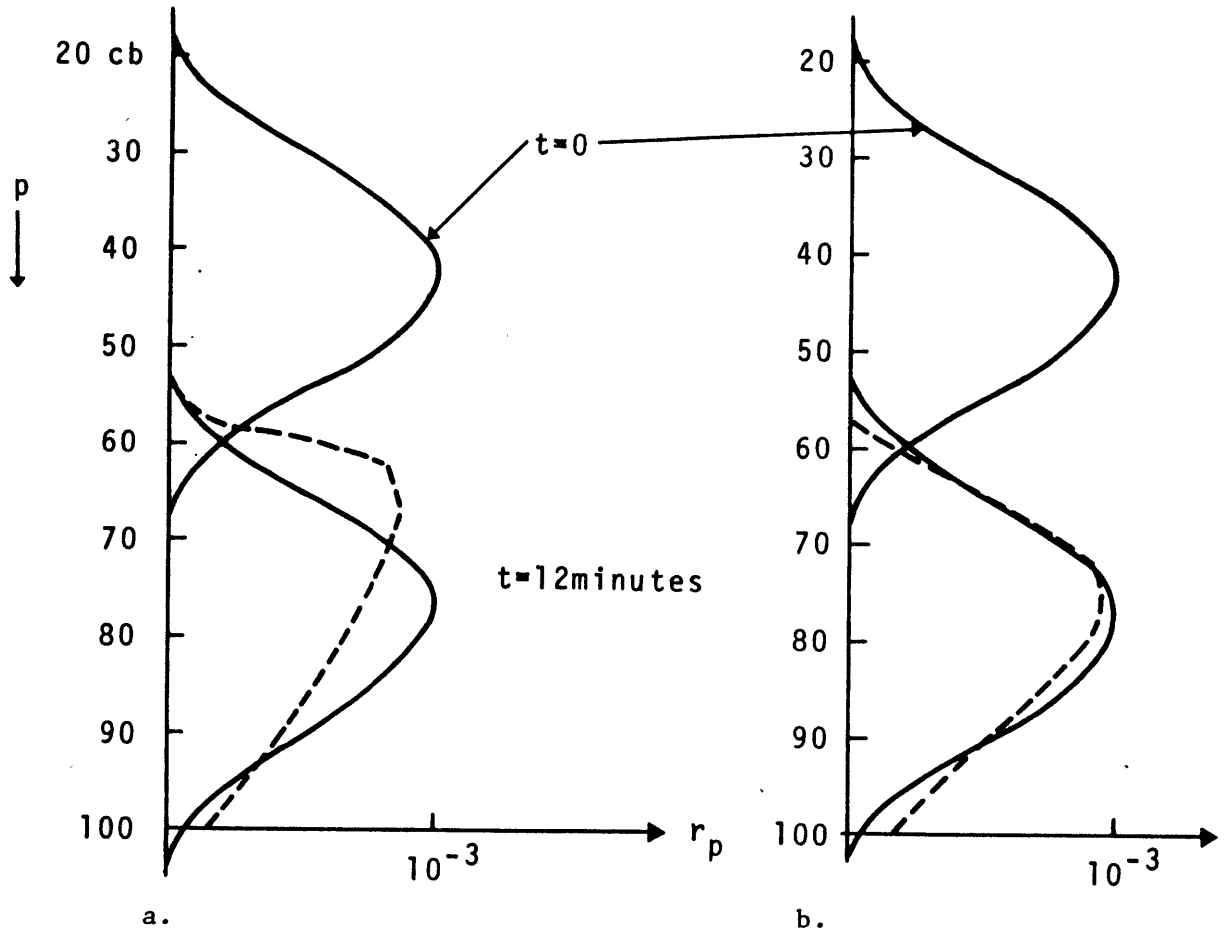


Figure D-2. Exact and Marchuk finite-difference solutions to (2.8) with $\omega_p = 0.05$ cb sec^{-1} and $A = 0 = E_p$. The exact solution is

$$r_p = 0.5 \times 10^{-3} \left\{ 1 + \sin \left[\frac{2\pi}{50} \left[(p - 30) - \omega_p t \right] \right] \right\},$$

$17.5 + \omega_p t \leq p \leq 67.5 + \omega_p t$, and zero elsewhere. Here, p is in cb. This solution at $t = 0$ constitutes the initial condition for the two finite-difference solutions. Part a. is for $\Delta t = 180$ seconds, the computational step used in runs in which there is no vertical shear of the zonal geostrophic wind, and b. is for $\Delta t = 5$ seconds.

t_p . As we should expect, reducing the time step to 5 seconds improves the accuracy of the finite difference solution considerably, but a 10% phase speed error in the t_p - maximum remains. The choice of $\omega_p = 0.05$ cb sec^{-1} was made with these results in mind.

Appendix E. A_c and E_p computation procedure and truncation error

$\mathcal{E}(p)$, appearing in equation (2.24), is listed below. The value appropriate to 0 C and 60 cb is assumed valid for $p < 60$ cb.

p (cb)	$\mathcal{E}(p)$
57.5 and above	4.0
62.5	3.9
67.5	3.7
72.5	3.5
77.5	3.3
82.5	3.1
87.5	2.8
92.5	2.5
97.5	2.1

The computation of A_c and E_p [equations (2.22) and (2.23)], which involves raising r_p to fractional powers, is expedited as follows. Prior to all computer runs with the complete model, two two-dimensional tables were constructed. These are indexed by pressure level (97.5 cb, 92.5 cb, etc.) and by r_p (0, 10^{-4}, 2 x 10^{-4}, etc.) and their entries are the pressure and r_p-dependent parts of A_c or E_p. During the time integration the computation of r_p raised to a non-integer exponent is thus replaced by linear interpolation into the appropriate table. Since these exponents are fairly close to 1, the errors made by doing this are largely only for very small r_p. A_c is in error by less than 10% for r_p greater than 0.4 x 10^{-4}; E_p is in error by less than 20% for r_p greater than 0.4 x 10^{-4}.

With a time step as large as 180 seconds it is necessary to exercise care in the incorporation of A_c and E_p into (2.5)-(2.8). In terms of the symbolic equation, $\partial f/\partial t = F(f)$, where F stands for A or E_p, the finite difference procedure used is

$$f_{n+1} = f_n + \frac{\Delta t}{2}\left[F(f_n) + F(f^*_{n+1})\right],$$

where $f^*_{n+1} = f_n + \Delta t\, F(f_n)$. The accuracy of this procedure was judged by comparing results from several pairs of runs. For each pair, initial conditions were the same, but one run was made with Δt = 5 seconds and the other with Δt = 180 seconds. Taking Δt = 5 seconds as the standard, the error in A_c due to the finite difference procedure is less than 10% unless r_ℓ is larger than 10^{-3} where r_p is less than $.5 \times 10^{-4}$. This unfavorable combination is present only during small portions of runs S1 and S2 (table 7). The underestimate in E_p obtained by examination of another pair of runs is under 10% except where $r_p < 0.4 \times 10^{-4}$ with $(r_s - r_v) > 5 \times 10^{3}$. This condition does occur in limited areas in most experiments, but this is not considered serious because r_p is so small.

From the time histories of r_ℓ and r_p at certain grid points within large-scale cloud it is evident that a coupled oscillation in r_ℓ and r_p develops when $r_p \gtrsim .05 \times 10^{-3}$ and $r_\ell \gtrsim 0.5 \times 10^{-3}$. This has a period of about 13-15 minutes which is apparently independent of Δt. The amplitude is a small fraction of r_p for r_ℓ and r_p close to the lower limits cited above, but for the larger r_ℓ and r_p associated with $\beta > 1.0$, the amplitude is at times of the order of r_p itself. The

oscillation is associated with the nonlinear coupling between k_ℓ and k_p in A_c . The oscillation is coupled to the motion field through E_p in (2.5), but the response in θ has amplitude $\lesssim \pm 0.01$ K, and no response is detected in the grid point history of ω . This oscillation is responsible for no more than a 5% underestimate in E_p averaged over one period.

REFERENCES

Arakawa, Akio, 1971: A parameterization of cumulus convection and its application to numerical simulation of the tropical general circulation. Paper presented at the Seventh Technical Conference on Hurricanes and Tropical Meteorology, Barbados, W.I.

_____, and Wayne Howard Schubert, 1974: Interaction of a cumulus cloud ensemble with the large-scale environment, Part I. J. Atmos. Sci., 31, 674-701.

Bates, J. R., 1972: Tropical disturbances and the general circulation. Quart. J. Roy. Meteor. Soc., 98, 1-16.

_____, 1973: A generalization of the CISK theory. J. Atmos. Sci., 30, 1509-1519.

Baumhefner, David P., 1968: Application of a diagnostic numerical model to the tropical atmosphere. Mon. Wea. Rev., 96, 218-228.

Beard, K. V., and Hans R. Pruppacher, 1971: A wind tunnel investigation of the rate of evaporation of small water drops falling at terminal velocity in air. J. Atmos. Sci., 28, 1455-1464.

Betts, A. K., 1973: A composite mesoscale cumulonimbus budget. J. Atmos. Sci., 30, 597-610.

_____, 1974: The scientific basis and objectives of the U.S. Convection Subprogram for the GATE. Bull. Amer. Meteor. Soc., 55, 304-313.

Bryan, K., 1966: A scheme for numerical integration of the equations of motion on an irregular grid free of nonlinear instability. Mon. Wea. Rev., 94, 39-40.

Charney, Jule G., 1963: A note on large-scale motions in the tropics. J. Atmos. Sci., 20, 607-609.

Donaldson, Ralph J., Jr., 1970: Mapping a thunderstorm anvil flow by Dappler radar. J. Appl. Meteor., 9, 911-915.

Fankhauser, James C., 1971: Thunderstorm-environment interactions determined from aircraft and radar observations. Mon. Wea. Rev., 99, 171-192.

Fujita, Tetsuya T., 1963: Analytical Mesometeorology: a review. Meteor. Monographs, Vol. 5, No. 27, 77-125.

Geisler, J. E., 1972: On the vertical distribution of latent heat release and the mechanics of CISK. J. Atmos. Sci., 29, 240-243.

Godbole, Ramesh V., 1973: On destabilization of clouds by radiative cooling. Mon. Wea. Rev., 101, 496-500.

Gray, William M., 1967: The mutual variation of wind, shear and baroclinicity in the cumulus convective atmosphere of the hurricane. Mon. Wea. Rev., 95, 55-73.

Hane, Carl E., 1973: The squall-line thunderstorm: numerical experimentation. J. Atmos. Sci., 30, 1672-1690.

Hawkins, Harry F., Jr., 1972: Development of a seven-level balanced, diagnostic model and its application to three disparate tropical disturbances. National Oceanic and Atmospheric Administration Technical Memorandum ERL NHRL-98, National Hurricane Research Laboratory, Miami, Florida.

Israeli, M., and E. S. Sarachik, 1973: Cumulus parameterization and CISK. J. Atmos. Sci., 30, 582-589.

Jordan, C. L., 1958: Mean soundings for the West Indies area. J. Meteor., 15, 91-97.

Kessler, Edwin III, 1969: On the distribution and continuity of water substance in atmospheric circulations. Meteor. Monographs, Vol. 10, No. 32, 1-84.

Knollenberg, Robert C., 1972: On radiational cooling computations in clouds. J. Atmos. Sci., 29, 212-214.

Kuo, H.-L., 1965: On the formation and intensification of tropical cyclones through latent heat release by cumulus convection. J. Atmos. Sci., 22, 40-63.

_____, 1973: Planetary boundary layer flow of a stable atmosphere over the globe. J. Atmos. Sci., 30, 53-65.

López, Raúl Erlando, 1972: Cumulus convection and larger-scale circulations, Part II: Cumulus and mesoscale interactions. Atmospheric Science Paper No. 189, Colorado State University.

_____, 1973: a parametric model for cumulus convection. J. Atmos. Sci., 30, 1354-1373.

Lorenz, E. N., 1960: Energy and numerical weather prediction. Tellus, 12, 364-373.

MacDonald, J. E., 1963: The saturation adjustment in numerical modelling of fog. J. Atmos. Sci., 20, 476-478.

Madden, R., E. Zipser, E. Danielson, D. Joseph, and R. Gall, 1971: Rawinsonde data obtained during the Line Islands Experiment. Volume I: Data reduction procedures and thermodynamic data. NCAR Technical Note TN/STR-55, National Center for Atmospheric Research, Boulder, Colorado.

Malkus, Joanne, and R. T. Williams, 1963: On the interaction between severe storms and large cumulus clouds. Meteor. Monographs, Vol. 5, No. 27, 59-64.

Marshall, J. S., and W. Mck. Palmer, 1948: The distribution of raindrops with size. J. Meteor., 5, 165-166.

Mason, B. J., 1969: Some outstanding problems in cloud physics -- the interactions of microphysical and dynamical processes. Quart. J. Roy. Meteor. Soc., 98, 449-485.

Miller, Banner I., Peter P. Chase, and Brian R. Jarvinen, 1972: Numerical prediction of tropical weather systems. Mon. Wea. Rev., 100, 825-838.

Newton, C. W., 1950: Structure and mechanism of the prefrontal squall line. J. Meteor., 7, 210-222.

_____, 1967: Severe convective storms. Advances in Geophysics, Vol. 12, 257-308, New York, Academic Press, 445 pp.

Nitta, Tsuyoshi, 1972: Energy budget of wave disturbances over the Marshall Islands during the years of 1956 and 1958. J. Met. Soc. Japan, Ser. II, 50, 71-84.

Ogura, Y., and J. G. Charney, 1962: A numerical model of thermal convection in the atmosphere. Proc. Int. Symp. on Numerical Weather Prediction, Meteor. Soc. Japan, Tokyo, 431-452.

_____, and Han-Ru Cho, 1973: Diagnostic determination of cumulus cloud populations from observed large-scale variables. J. Atmos. Sci., 30, 1276-1286.

_____, and N. A. Phillips, 1962: Scale analysis of deep and shallow convection in the atmosphere. J. Atmos. Sci., 19, 173-179.

Ooyama, Katsuyuki, 1971: A theory on parameterization of cumulus convection. J. Met. Soc. Japan, Ser. II, 49, (Special Issue), 744-756.

Phillips, Norman A., 1960: On the problem of initial data for the primitive equations. Tellus, 12, 121-126.

_____, 1973: Principles of large scale numerical weather prediction. Dynamic Meteorology, P. Morel, ed., Dordrecht, Holland, and Boston, U.S.A., Reidel, 1-96.

Pond, S., G. T. Phelps, J. E. Paquin, G. McBean, and R. W. Stewart, 1971: Measurements of the turbulent fluxes of momentum, moisture, and sensible heat over the ocean. J. Atmos. Sci., 28, 918-928.

Reed, Richard J., and Ernest E. Recker, 1971: Structure and properties of synoptic-scale wave disturbances in the equatorial Western Pacific. J. Atmos. Sci., 28, 1117-1133.

Riehl, H., 1965: Varying structure of waves in the easterlies. Dynamics of Large-Scale Atmospheric Processes. Proc. Intern. Symp. Moscow, 411-416.

_____, 1969: Some aspects of cumulonimbus convection in relation to tropical weather systems. Bull. Amer. Meteor. Soc., 50, 587-595.

_____, and R. P. Pierce, 1968: Studies on interaction between synoptic and mesoscale weather elements in the tropics. Atmospheric Science Paper No. 126, Colorado State University.

Rosenthal, Stanley L., 1970: A circularly symmetric primitive equation model of tropical cyclone development containing an explicit water vapor cycle. Mon. Wea. Rev., 98, 643-663.

Sasaki, Y., 1962: Effects of condensation, evaporation, and rainfall on development of mesoscale disturbances: a numerical experiment. Proc. Intern. Symp. on Numerical Weather Prediction, Meteor. Soc. Japan, Tokyo, 477-500.

Schlesinger, Robert E., 1973a: A numerical model of deep moist convection: Part I. Comparative experiments for variable ambient moisture and wind shear. J. Atmos. Sci., 30, 835-856.

_____, 1973b: A numerical model of deep moist convection: Part II. A prototype experiment and variations upon it. J. Atmos. Sci., 30, 1374-1391.

Simpson, Joanne, 1972: A note on the CISK mechanism in the tropics and its role in disturbance formation and maintenance. Unpublished manuscript, 15 pp.

_____, and Victor Wiggert, 1969: Models of precipitating cumulus towers. Mon. Wea. Rev., 97, 471-489.

_____, and _____, 1971: 1968 Florida cumulus seeding experiment: numerical model results. Mon. Wea. Rev., 99, 87-118.

Syōno, S., and M. Yamasaki, 1966: Stability of symmetrical motions driven by latent heat release by cumulus convection under the existence of surface friction. J. Met. Soc. Japan, Ser II, 44, 353-375.

Williams, Knox T., and William M. Gray, 1973: Statistical analysis of satellite-observed trade wind cloud clusters in the western North Pacific. Tellus, 25, 313-336.

Williams, R. T., 1967: Atmospheric frontogenesis: a numerical experiment. J. Atmos. Sci., 24, 627-641.

Yamasaki, Masanori, 1968: Numerical simulation of tropical cyclone development with the use of primitive equations. J. Met. Soc. Japan, Ser. II, 46, 178-201.

Yanai, Michao, Steven Esbensen, and Jan-Hwa Chu, 1973: Determination of bulk properties of tropical cloud clusters from large-scale heat and moisture budgets. J. Atmos. Sci., 30, 611-627.

Zipser, E. J., 1968: Talk on the 1968 Florida State University Barbados Project, at September meeting of south Florida chapter of the American Meteorological Society.

_____, 1969: The role of organized unsaturated convective downdrafts in the structure and rapid decay of an equatorial disturbance. J. Appl. Meteor., 8, 799-814.

BIOGRAPHIC NOTE

The author was born 3 February 1943 in San Diego, California. Somehow, in what is surely one of the world's most boring climates, he developed a fascination for the weather in his earliest years, which remains undiminished to the present day. He attended the public schools of San Diego, and the University of California at Los Angeles, where he majored in meteorology.

The author moved to Cambridge in 1966 and in 1970 married Miss Judy Carol Martin of Brookline. He is currently teaching meteorology at Iowa State University.